Immersion Scatterometry for Nanoscale Grating Topography Extraction

by

Elson Yee-Hsin Liu

A dissertation submitted in partial fulfillment
of the requirements for the degree of
Doctor of Philosophy
(Electrical Engineering)
in The University of Michigan
2014

Doctoral Committee:

Professor Fred L. Terry, Jr., Chair
Professor Brian D. Athey
Professor Jeffrey A. Fessler
Professor Kim A. Winick

Those who stay will be champions!

—Bo Schembechler

© Elson Yee-Hsin Liu

All Rights Reserved

2014

To my parents, who have always supported me

Acknowledgments

There are countless people whom I'd like to thank for their support over the course of my Ph.D. studies. First, I'd like to thank my advisor, Fred Terry, for introducing me to the scatterometry problem. Many thanks to him for providing me with guidance when I needed direction, and for having the patience to put up with me for the duration of this project.

I'd also like to thank Brian Athey, Jeff Fessler, and Kim Winick, for agreeing to serve on my committee and for the myriad ways they have supported me throughout my graduate studies. This thesis has surely been improved by their feedback.

Numerous staff members of the Lurie Nanofabrication Facility (LNF) provided direct assistance to the work in this thesis. Thanks for Sandrine Martin, Pilar Herrera-Fierro, and Tom Latowski for providing access to deionized water from the LNF for my immersion experiments. Thanks also to Dennis Schweiger and Dave Kouba for assistance in designing the immersion cell.

I would never made it here without the support and assistance of several EECS central staff members. Among them, I'd like to thank Beth Stalnaker for helping me navigate the EECS Ph.D. process, and Karen Liska for smoothing over all the HR hiccups that invariably occurred in the transitions between GSRA appointments and GSI appointments.

These acknowledgements would not be complete without mentioning my advisor at the beginning of my Ph.D. journey, the late Emmett Leith. He had a particular knack for coming up with the simplest and clearest explanations for complex concepts,

and I can only hope that I acquired some of that skill and applied it to this thesis.

When I was between labs, I became involved with student organizations again, and they became a outlet to help maintain my sanity. I'd like to acknowledge the support of Anika Awai-Williams, Jen Wegner, and Susan Wilson in my involvement with the Tau Beta Pi engineering honor society, the Epeians engineering honor society, and the University of Michigan Central Student Government (formerly known as the Michigan Student Assembly).

I'd also like to thank the many friends I've had and/or made over the course of my graduate studies. Any listing of them is likely to be woefully incomplete, but I'd feel terrible if I didn't at least acknowledge the following: Steve Agacinski, Vinay Alexander, Nicholas Baine, Tim Bekkers, Michael Benson, J. P. Blackford, Giacomo Bologna, Peter Borock, Andy Boucher, Jim Brusstar, Alan Chang, Greg Chen, Mel Chi, Wei-Chen Chien, Mike Chin, Dave Clark, Liz Cloos, Mohammad Dar, Chuck Divin, Brad Dobbie, Alex Dowling, Kiran D'Souza, Ethan Eagle, Sakib Elahi, Matt Eral, Kaitlin Flynn, Chris Galbraith, Nate Gallaher, Ezra Geggel, Gerald Giarmo, Rob Goeddel, Kristin Graf, Shawn Grannell, Curt Gomulinski, Sam Haberl, Mike Hand, Eric Harper, Rae-Anne Hayes, Paul Hou, Tim Hull, Michael Huston, Eric Jankowski, Mike Jonell, Jeremy Keeney, Dan Kiefer, Stephan King-Monroe, Katy Kneiser, Matt Kneiser, Doug Krusell, Kyle Lady, Anne Laverty, Michael Z. Lee, Victor Lee, Jack Li, Andrew Lingg, Lauren H. Logan, Brandon Lucas, John Lyons, Pritpaul Mahal, Abhishek Mahanti, Paul Mattis, Shawn McDermed, Prakit Mohal, Dan Nathan-Roberts, Michelle Noronha, Patrick O'Mahen, Kevin Owen, Pat Pannuto, Beth Percha, Jeff Powers, Ahmir Rashid, Vikas Reddy, Ryan Rindler, Mike Rorro, Dave Sebastian, Dhritiman Sagar, Barry Shang, Jeff Simmons, Ethan Stark, Brian Steers, Chris Stevens, Jessica TerBush, Carlos Torres, Bryan Toth, Rachel Trabert, Adam Tury, Matt VanderKolk, Ray Walling, Elmer Wang, Rob Warren, Garrick Williams, Emily Wolters, Eric Wucherer, Randy Yao, Edwin Yik, Menna Youssef, and

Phil Zeeck.

Finally, many thanks to my parents, Nai-hsiang Liu and Horng-shing Chang, and my sister, Annie, for a lifetime of support.

Table of Contents

Dedication ii

Acknowledgments iii

List of Tables viii

List of Figures ix

Abstract xiii

Chapter 1 Introduction 1
- 1.1 Problem statement 3
- 1.2 Research accomplishments 4
- 1.3 Outline of the thesis 5

Chapter 2 Background: grating topography extraction by scatterometry 6
- 2.1 Optical scattering from interfaces and thin films 7
  - 2.1.1 Interfaces 7
  - 2.1.2 Thin films 7
- 2.2 Rigorous coupled-wave analysis (RCWA) of gratings 8
  - 2.2.1 Planar diffraction from binary gratings 10
  - 2.2.2 Planar diffraction from surface-relief gratings 19
- 2.3 Data collection: Ellipsometry 23
  - 2.3.1 Spectroscopic ellipsometry 26
  - 2.3.2 Immersion ellipsometry 27
- 2.4 Data analysis 27
  - 2.4.1 Data fitting: Levenberg-Marquardt regression 27
  - 2.4.2 Grating profile parameterization 32

Chapter 3 Immersion scatterometry: preliminary results 33
- 3.1 Materials and methods 34
  - 3.1.1 Samples 34
  - 3.1.2 Ellipsometer 34

3.1.3 Cell 34
3.1.4 Optical properties of water 35
3.2 Simulation of 100-nm period gratings 38
3.3 Measurements on the 700-nm period gratings 41
3.4 Measurements on the 160-nm period gratings 46

Chapter 4 Investigation of systematic errors in immersion ellipsometry 51
4.1 Errors in angle of incidence 51
4.1.1 Simulation 53
4.1.2 Materials and methods 54
4.1.3 Results and discussion 56
4.2 Errors in ambient refractive index 61
4.2.1 Simulation 61
4.2.2 Materials and methods 61
4.2.3 Results and discussion 63
4.3 Errors due to stress-induced window birefringence 65
4.3.1 Simulation 66
4.3.2 Materials and methods 68
4.3.3 Results and discussion 69

Chapter 5 Improved procedure of grating topography extraction by immersion scatterometry 72
5.1 Materials and methods 72
5.2 Results and discussion 73
5.2.1 Atmospheric measurements of bare silicon 73
5.2.2 Immersion measurements of bare silicon 73
5.2.3 Atmospheric measurements of thick SiO_2 film 74
5.2.4 Immersion measurements of thick SiO_2 film 75
5.2.5 Atmospheric measurements of 700-nm pitch Sony photoresist grating 75
5.2.6 Immersion measurements of 700-nm pitch Sony photoresist grating 77

Chapter 6 Conclusion and future work 81
6.1 Summary 81
6.2 Future work 82

Bibliography 83

List of Tables

Table

4.1 Angular repeatability of immersion ellipsometric measurements of a nominally bare silicon wafer in an unanodized aluminum cell. 58

4.2 Angular repeatability of immersion ellipsometric measurements of a nominally bare silicon wafer in an anodized aluminum cell. 59

4.3 Estimated ambient temperature T for ellipsometric measurements of the 2.0037 µm SiO_2 SOPRA reference wafer in undegassed and degassed deionized water. 65

4.4 Estimated oxide thickness t and in-plane retardance parameter p for ellipsometric measurements of the 2.0037 µm SiO_2 SOPRA reference wafer in deionized water. 70

5.1 Atmospheric measurements of bare silicon used to estimate the native oxide thickness. 73

5.2 Immersion measurements of bare silicon to estimate the immersion angle of incidence. 74

5.3 Atmospheric measurements of SOPRA 2.0037 µm SiO_2 reference wafer used to estimate the oxide thickness. 74

5.4 Immersion measurements of SOPRA 2.0037 µm SiO_2 reference wafer used to estimate the oxide thickness and the first-order in-plane retardance parameter. 75

5.5 Fit results and 95.4% confidence limits for an 8-trapezoid grating model to dry ellipsometric measurements of the 700-nm grating with new photoresist data. 76

5.6 Fit results and 95.4% confidence limits for an 8-trapezoid grating model to wet ellipsometric measurements of the 700-nm grating without birefringence correction. 78

5.7 Fit results and 95.4% confidence limits for an 8-trapezoid grating model to wet ellipsometric measurements of the 700-nm grating with birefringence correction. 80

List of Figures

Figure

2.1 Illustrating the Fresnel reflection and transmission coefficients from an interface. 8
2.2 Geometry for analysis of reflection from a thin film. 9
2.3 Geometry of the binary grating diffraction problem in the planar diffraction configuration. 11
2.4 Geometry for representing a surface-relief grating as a stack of 4 binary gratings. 20
2.5 Schematic of a basic ellipsometer operating in the reflection mode. Light from a source is collimated by optics L_1, passes through a polarization state generator, and reflects from the sample. The reflected light passes through a polarization state analyzer, and is focused by optics L_2 onto a detector. 23
2.6 Illustrating the trapezoidal parameterization of grating profiles. . . . 32

3.1 Extracted effective-medium approximation (EMA) refractive index for water (solid blue curve) and Tilton–Taylor reference data at 23°C (dashed green curve). Observe that the curves for the EMA model, the Tilton–Taylor model for $T = 37$°C, and freely-varying Tilton–Taylor model overlap, but the Tilton–Taylor model for $T = 23$°C does not. . 37
3.2 Refractive index of Quan-Fry seawater at 10‰(dashed blue curve) and 5‰(dash-dot green curve) salinity compared to Tilton-Taylor water (solid red curve) at 25 °C. 38
3.3 Simulated ellipsometric spectra for 100-nm period silicon gratings with linewidths of 16 nm, 20 nm and 24 nm in air. 39
3.4 Simulated ellipsometric spectra for 100-nm period silicon gratings with linewidths of 16 nm, 20 nm and 24 nm in deionized water. 40
3.5 Simulated ellipsometric spectra for 100-nm period, 24-nm average linewidth silicon gratings with sidewall angles of 90°, 87.5° and 85° in air. 40
3.6 Simulated ellipsometric spectra for 100-nm period, 24-nm average linewidth silicon gratings with sidewall angles of 90°, 87.5° and 85° in deionized water. 41

3.7 Measured (blue solid curves) and best-fit (green dashed curves) spectroscopic ellipsometric (SE) data for a single-trapezoid model of the 700-nm photoresist (PR) grating measured in air. 42
3.8 Measured and best-fit SE data for an 8-trapezoid model of the 700-nm PR grating measured in air. 43
3.9 Fit results and 95.4% confidence limits for an 8-trapezoid grating model to dry ellipsometric measurements of the 700-nm grating. 43
3.10 Comparison of best 8-trapezoid fit (blue outline) of the 700-nm grating measured in air with cross-sectional scanning electron micrograph. . . 43
3.11 Simulated $m = 3$ backscattered reflected (solid blue) and transmitted (dashed red) energy for best-fit 8-trapezoid model of the 700-nm grating measured in air. 44
3.12 Measured and best-fit SE data for an 8-trapezoid model of the 700-nm PR grating measured in water. 45
3.13 Comparison of the best fit from SE data for an 8-trapezoid model of the 700-nm PR grating measured in water (red) and air (blue). 45
3.14 Comparison of the dry-only fit (blue) and dual dry/BEMA fit (red) for the 700 nm grating. 46
3.15 Measured and best-fit SE data for a single-trapezoid model of the 160-nm PR grating measured in air. 47
3.16 Measured and best dual-ambient fit SE data for a single-trapezoid model of the 160-nm PR grating measured in water. 48
3.17 Fit results and confidence limits for a single-trapezoid grating model to dual-mode (dry and wet) ellipsometric measurements of the 160-nm grating. $\sigma = 2.5 \times 10^{-2}$ for this fit. 48
3.18 Measured and best-fit SE data for a 16-trapezoid model of the 160-nm PR grating measured in air. 49
3.19 Measured and best dual-ambient fit SE data for a 16-trapezoid model of the 160-nm PR grating. 50

4.1 Deviation of an oblique ray incident upon an ideal plane-parallel window. 52
4.2 Error surface for immersion ellipsometry of a nominally bare silicon wafer (2 nm SiO_2 on Si) in deionized water for errors in the angle of incidence (AOI) and ambient temperature. The contours of the error surface show that immersion measurements of this sample are relatively sensitive to angle of incidence and relatively insensitive to ambient temperature, since a relatively small change in the angle of incidence results in a mean-squared error comparable to a relatively large change in the ambient temperature. 55
4.3 A representative ellipsometric spectrum from a “bare” silicon wafer in air in (α, β) format. 57
4.4 A representative ellipsometric spectrum from a “bare” silicon wafer in deionized water in (α, β) format. 57

4.5 Estimated angle of incidence from ellipsometric measurements of a “bare” silicon wafer in deionized water, taken in an unanodized aluminum cell over the course of several weeks. The horizontal lines associated with each data point indicate the upper confidence limit and lower confidence limit of the 95.4% confidence interval for each individual measurement. 58
4.6 Estimated SiO_2 thickness from ellipsometric measurements of a “bare” silicon wafer in deionized water, taken in an unanodized aluminum cell over the course of several weeks. The vertical lines associated with each data point indicate the 95.4% confidence interval for each individual measurement. 59
4.7 Estimated angle of incidence from ellipsometric measurements of a “bare” silicon wafer in deionized water, taken in an anodized aluminum cell over the course of a week. The horizontal lines associated with each data point indicate the upper confidence limit and lower confidence limit of the 95.4% confidence interval for each individual measurement. 60
4.8 Estimated SiO_2 thickness from ellipsometric measurements of a “bare” silicon wafer in deionized water, taken in an anodized aluminum cell over the course of a week. The vertical lines associated with each data point indicate the 95.4% confidence interval for each individual measurement. 60
4.9 Error surface for immersion ellipsometry of a thick (2 µm) SiO_2 film on Si in deionized water for errors in the angle of incidence and ambient temperature. 62
4.10 Representative ellipsometric spectrum for SOPRA reference wafer with 2.0037 µm SiO_2 on Si in air. 64
4.11 Representative ellipsometric spectrum for SOPRA reference wafer with 2.0037 µm SiO_2 on Si in deionized water. 64
4.12 Comparison of the dry and wet simulated ellipsometric spectra for the dry best-fit profile for the 700 nm Sony photoresist grating. The wet β spectrum (bottom center) shows an offset between the experimental data (solid blue) and the simulated spectrum (green dashed) for the dry best-fit profile in the immersion case. 66
4.13 Error surface for immersion ellipsometry of a nominally bare silicon wafer (2 nm SiO_2 on Si) in deionized water for errors in the angle of incidence and first-order in-plane retardance parameter. 67
4.14 Error surface for immersion ellipsometry of a a thick (2 µm) SiO_2 film on Si in deionized water for errors in the angle of incidence and first-order in-plane retardance parameter. 68
4.15 Error surface for immersion ellipsometry of a a thick (2 µm) SiO_2 film on Si in deionized water for errors in the oxide thickness and first-order in-plane retardance parameter. 69
4.16 In-plane retardance spectrum estimated from ellipsometric measurements of the 2.0037 µm SiO_2 SOPRA reference wafer in deionized water. 71

5.1 Measured SE data for a uniform film of Sony photoresist taken at $\theta = 75°$. 76
5.2 Measured and best-fit SE data for an 8-trapezoid model of the Sony 700-nm photoresist grating measured in air. 77
5.3 Measured and best-fit SE data for an 8-trapezoid model of the Sony 700-nm photoresist grating measured in deionized water with no birefringence correction. 79
5.4 Measured and best-fit SE data for an 8-trapezoid model of the Sony 700-nm photoresist grating measured in deionized water with birefringence correction from thick SiO_2 data. 79
5.5 Comparison of the simulated dry ellipsometric spectra (green dashed) for the 8-trapezoid wet best-fit profile (without birefringence correction) for the 700 nm Sony photoresist grating with experimental data (solid blue). 80

Abstract

The objective of optical scatterometry is to determine the geometrical parameters of a periodic structure, such as a surface-relief grating, from its ellipsometric spectrum. There is particular interest in applying this technique to semiconductor metrology, where it can be used for wafer-to-wafer process monitoring and control of lithographic and etching processes.

In this thesis, immersion scatterometry is investigated to improve feature resolution for nanoscale surface-relief gratings. Improved resolution may come in the form of reduced uncertainty in estimated parameters, or reconstruction of previously unresolved features. The rationale behind immersion scatterometry is that increasing the ambient refractive index reduces the effective wavelength, which means that scattered modes that are evanescent in atmosphere may be propagating modes in the immersion case. Additional propagating reflected modes create the potential for more features in the specular-mode ellipsometric spectrum, which can convey additional information about the sample under investigation.

Initial experimental results for immersion ellipsometry and topography extraction of gratings are reported. Potential sources of systematic error in immersion ellipsometry are investigated. The effects of these error sources are quantified, and mitigation strategies are evaluated. These strategies should also aid in reducing errors in other applications of immersion ellipsometry, including electrochemistry, biology, and medicine.

Chapter 1

Introduction

The problem of grating topography extraction by spectroscopic ellipsometry, or *scatterometry*, is to determine the geometrical parameters (linewidth, profile, etc.) of a periodic structure from its ellipsometric spectrum. There is particular interest in applying this technique to semiconductor metrology, where it can be used for wafer-to-wafer process monitoring and control of lithographic and etching processes. The semiconductor industry is faced with an ongoing challenge to keep pace with Moore's law by scaling to ever shrinking feature sizes. This presents challenges to both fabrication and metrology. On the fabrication side, immersion lithography has been utilized to reduce the effective wavelength, and multiple patterning has been utilized to exceed classical resolution limits. On the metrology side, optical microscopy was used until critical dimensions and feature sizes shrank below the *Rayleigh resolution limit*,

$$R = k_1 \frac{\lambda}{NA},$$

where k_1 is a constant characterizing the imaging system ($k_1 = 0.61$ for ideal imaging systems with circular pupils and on-axis illumination), λ is the wavelength of the imaging light, and $NA = n \sin \alpha$ is the *numerical aperture*, which measures the light-collecting capability of the imaging system.

Once optical microscopy no longer had the capability to resolve the necessary critical dimensions and feature sizes, scanning electron microscopy (SEM) took over as the dominant metrology technique. SEM probes a sample with a focused beam

of electrons and detects one or more signals generated by the interaction of those electrons with the sample. Signals generated by this interaction include secondary electrons (SE), backscattered electrons (BSE), characteristic X-rays, light generated by cathodoluminescence (CL), specimen current, and transmitted electrons. By scanning the probe beam over the sample, an image of the sample's surface topography and/or material composition can be formed. SEM can be used to image cross sections of samples (cross-sectional SEM), or to estimate critical dimensions or feature sizes from top-down or tilted column images (critical dimension SEM, or CD-SEM). Cross-sectional SEM produces images that most closely resemble the ground truth, but the sample must be cleaved to expose the feature to be imaged, making it an inherently destructive measurement. CD-SEM does not require destructive sectioning of the sample, but faces other measurement challenges such as charging (the build-up of electrons on the sample, creating a time-dependent inhomogeneous electric field affecting the measurement) [1] and photoresist shrinkage (the observation that photoresist linewidths shrink after electron beam exposure) [2].

Scatterometry can estimate the topography of periodic microfabricated structures with precision well exceeding classical resolution limits. The procedure for grating topography extraction by scatterometry consists of two basic steps:

1. *Collect experimental optical scattering data.* This data may be ellipsometric or reflectometric and it may be spectroscopic or angle-resolved. In the work done for this thesis, we used specular-mode spectroscopic ellipsometry to acquire optical scattering data.
2. *Determine the geometry of grating that produces the scattering response that best fits the experimental data.* A parametrized model of the grating topography is constructed for forward-scattering simulations. The forward-scattering simulation may be used to pre-compute a library of scattering responses, or the simulation may be driven by a data-fitting algorithm to search for the parameters that best match the experimental data. In the work done for this thesis, we used Levenberg-Marquardt regression to drive a rigorous coupled-wave analysis (RCWA) grating diffraction simulation.

Scatterometry is an attractive metrology technique for semiconductor production

because it offers feature shape resolution comparable to CD-SEM or atomic force microscopy with high throughput, high repeatability, and less risk of damage to the sample [3]. Huang and Terry [4] note several reasons why the scatterometry measurement is able to extract feature shape information with resolution well beyond the Rayleigh limit. First, we have a lot of prior information about the structure, namely that it is periodic (and the period is known or can be determined with high accuracy), and optical constants of the structure are also well known. This is a much more constrained problem than image formation for an arbitrary scene. Second, we have information collected across a wide spectral range. Third, the measurement is sensitive to evanescent modes in the grating region which are not accessible to a conventional optical imaging system.

1.1 Problem statement

In this thesis, immersion scatterometry is investigated to improve feature resolution. Improved resolution may come in the form of reduced uncertainty in estimated parameters, or reconstruction of previously unresolved features. The rationale behind immersion scatterometry is that increasing ambient refractive index n results in a shorter effective wavelength

$$\lambda = \frac{\lambda_0}{n},$$

which enables more propagating backscattered modes, which are mode numbers m and scattering angles θ_m that satisfy the grating equation

$$\Lambda(\sin\theta_m + \sin\theta_i) = \frac{m\lambda_0}{n}.$$

The existence of more propagating backscattered modes creates the potential for more features in the specular-mode ellipsometric spectrum, but enabling additional propa-

gating modes from the grating equation is not a necessary condition for generating additional features in the ellipsometric spectrum. Changing the coupling of energy into existing propagating modes (by changing the geometry of the grating lines or the optical properties of the grating material, for example) can also generate new features. This, in turn, creates the potential to resolve geometrical features of the sample that could not be resolved without immersion, or to reduce the uncertainty in the estimated geometrical parameters. However, systematic errors may be present in the immersion measurement that are not present when the measurement is performed normally in atmosphere. Thus a significant component of this thesis is identifying and characterizing potential sources of systematic error in the immersion case. In this thesis, we identify three potential sources of systematic error in the immersion case:

1. Error in the angle of incidence on the sample in the immersion case,
2. Deviation of the refractive index of the immersion medium from published data and models, and
3. Stress-induced birefringence in the windows that admit the probe beam and transmit the scattered beam.

For each error source, we develop experiments to characterize this quantity and control it to the extent possible with our current experimental setup.

1.2 Research accomplishments

The following original research accomplishments were achieved while performing the work reported in this thesis:

- The first experimental demonstration of grating topography extraction by liquid-immersion spectroscopic ellipsometry [5].
- The development of a novel dual-ambient strategy for grating topography extraction using ellipsometric data collected in air and in liquid immersion [5].
- The development and characterization of a repeatable sample alignment procedure to reduce systematic error due to small deviations in angle of incidence.
- The development of a procedure to estimate the refractive index of the liquid ambient and reduce associated systematic error.
- The development of a procedure to estimate the stress-induced birefringence of

the sample cell windows in the immersion case and compensate for the associated systematic error.
- The development of a procedure to mitigate systematic error in grating topography extraction.

1.3 Outline of the thesis

In chapter 2 we review the background of grating topography extraction by scatterometry. We review the scattering of electromagnetic waves, such as light, from planar interfaces, thin films, binary gratings and surface relief gratings. Then we review the technique of spectroscopic ellipsometry, which measures the polarization dependence of the scattering of light from a sample. Finally we review strategies for grating topography extraction from ellipsometric data.

In chapter 3 we present initial experimental results for immersion scatterometry. We describe the modifications necessary to perform the immersion method, the samples we used for our initial experiments, and the results of these experiments.

In chapter 4 we investigate three potential sources of systematic error in immersion ellipsometry: error in the angle of incidence, error in the immersion refractive index, and error introduced by stress-induced birefringence in the immersion cell windows. We describe the samples that we use to characterize these errors, motivate the choice of these samples using the results of computer simulations, and present experimental results.

In chapter 5 we propose an improved measurement procedure for immersion scatterometry to try to mitigate the effects of the sources of systematic error considered in chapter 4. We present experimental results and evaluate the performance of this procedure.

Finally, in chapter 6 we summarize the results presented in this thesis and propose avenues for future work.

Chapter 2

Background: grating topography extraction by scatterometry

Optical scattering from grating test structures has been used for some time to determine the topography or critical dimension of micro- or nanofabricated devices. Kleinknecht and Meier used measurements of the intensity of the first two diffracted orders of HeNe laser light scattered from photolithographic masks or photoresist gratings to determine the linewidth [6]. McNeil, Naqvi, and co-workers coined the term *scatterometry* to describe the use of angle-resolved ellipsometric measurements and rigorous coupled-wave simulations to determine the width and profile of subwavelength gratings [7, 8]. Terry and co-workers [9] and Spanos and co-workers [10, 11] independently proposed the use of specular spectroscopic ellipsometric measurements instead of single-wavelength, angle-resolved measurements; the Spanos group coined the name *specular spectroscopic scatterometry* for this technique.

In this chapter we review the basic theory of topography extraction by scatterometry. We begin by reviewing the theory of optical scattering from interfaces, thin films, and surface-relief gratings. Then we review the principles of ellipsometry, which is the experimental technique that we use to collect optical scattering data. Finally, we review the data analysis techniques used to reconstruct grating topography from ellipsometric data, namely Levenberg-Marquardt regression, and the models used to represent the structures and materials under consideration.

2.1 Optical scattering from interfaces and thin films

2.1.1 Interfaces

The amount of light that is reflected or transmitted from a planar interface between two media (figure 2.1) is given by the Fresnel coefficients, which are determined by matching the components of the electric and magnetic fields that are parallel to the interface. The Fresnel coefficients for reflection and transmission of p-polarized (TM) and s-polarized (TE) light at an interface between a medium with complex refractive index $\tilde{n}_1 = n_1 - j\kappa_1$ and a medium with complex refractive index $\tilde{n}_2 = n_2 - j\kappa_2$ at an angle of incidence θ_1 are given by [12, appendix C]

$$r_{12}^p = \frac{\tilde{n}_2 \cos\theta_1 - \tilde{n}_1 \cos\theta_2}{\tilde{n}_2 \cos\theta_2 + \tilde{n}_1 \cos\theta_2} \qquad t_{12}^p = \frac{2\tilde{n}_1 \cos\theta_1}{\tilde{n}_2 \cos\theta_1 + \tilde{n}_1 \cos\theta_2} \tag{2.1}$$

$$r_{12}^s = \frac{\tilde{n}_1 \cos\theta_1 - \tilde{n}_2 \cos\theta_2}{\tilde{n}_1 \cos\theta_1 + \tilde{n}_2 \cos\theta_2} \qquad t_{12}^s = \frac{2\tilde{n}_1 \cos\theta_1}{\tilde{n}_1 \cos\theta_1 + \tilde{n}_2 \cos\theta_2} \tag{2.2}$$

where the transmission angle θ_2 is given by Snell's law,

$$\tilde{n}_1 \sin\theta_1 = \tilde{n}_2 \sin\theta_2. \tag{2.3}$$

2.1.2 Thin films

For simplicity, we consider a sample which is a thin film of refractive index $\tilde{n}_2$ and thickness d on a substrate of refractive index $\tilde{n}_3$ and an incidence angle of θ_1 in an ambient refractive index $\tilde{n}_1$ (figure 2.2). The total reflection from this film originates from the reflection and transmission of light from the ambient-film interface and the film-substrate interface. Then it can be shown [12, appendix C] that the total

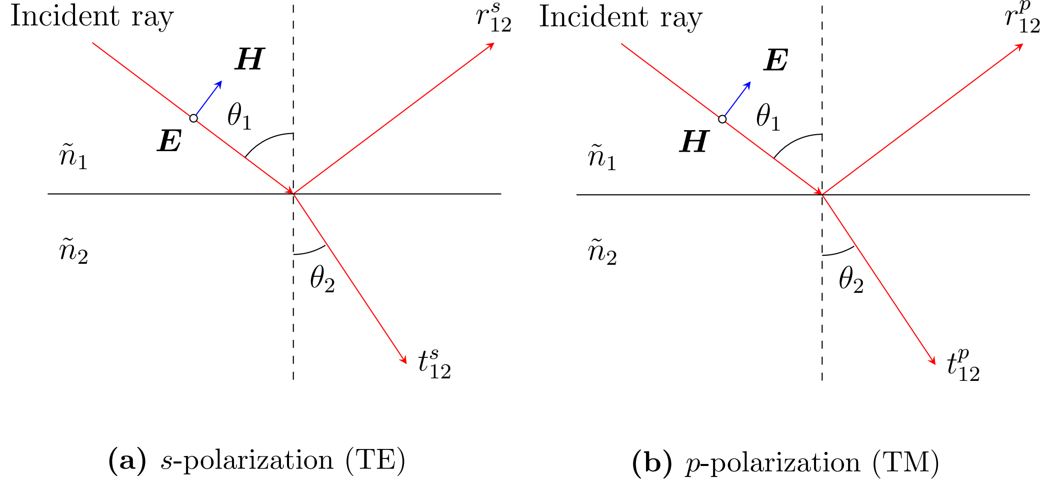

(a) s-polarization (TE)

(b) p-polarization (TM)

Figure 2.1 Illustrating the Fresnel reflection and transmission coefficients from an interface.

reflection coefficients of the film are

$$R_p = \frac{r^p_{12} + r^p_{23}\exp(-j2\beta)}{1 + r^p_{12}r^p_{23}\exp(-j2\beta)} \tag{2.4}$$

$$R_s = \frac{r^s_{12} + r^s_{23}\exp(-j2\beta)}{1 + r^s_{12}r^s_{23}\exp(-j2\beta)} \tag{2.5}$$

where

$$\beta = \frac{2\pi}{\lambda} d\tilde{n}_2 \cos\theta_2. \tag{2.6}$$

2.2 Rigorous coupled-wave analysis (RCWA) of gratings

The grating equation

$$\Lambda(\sin\theta_m + \sin\theta_i) = \frac{m\lambda_0}{n}. \tag{2.7}$$

tells us in which directions light is diffracted (or scattered) from a grating, but it does not tell us how much energy is coupled into each scattered mode. We need to know

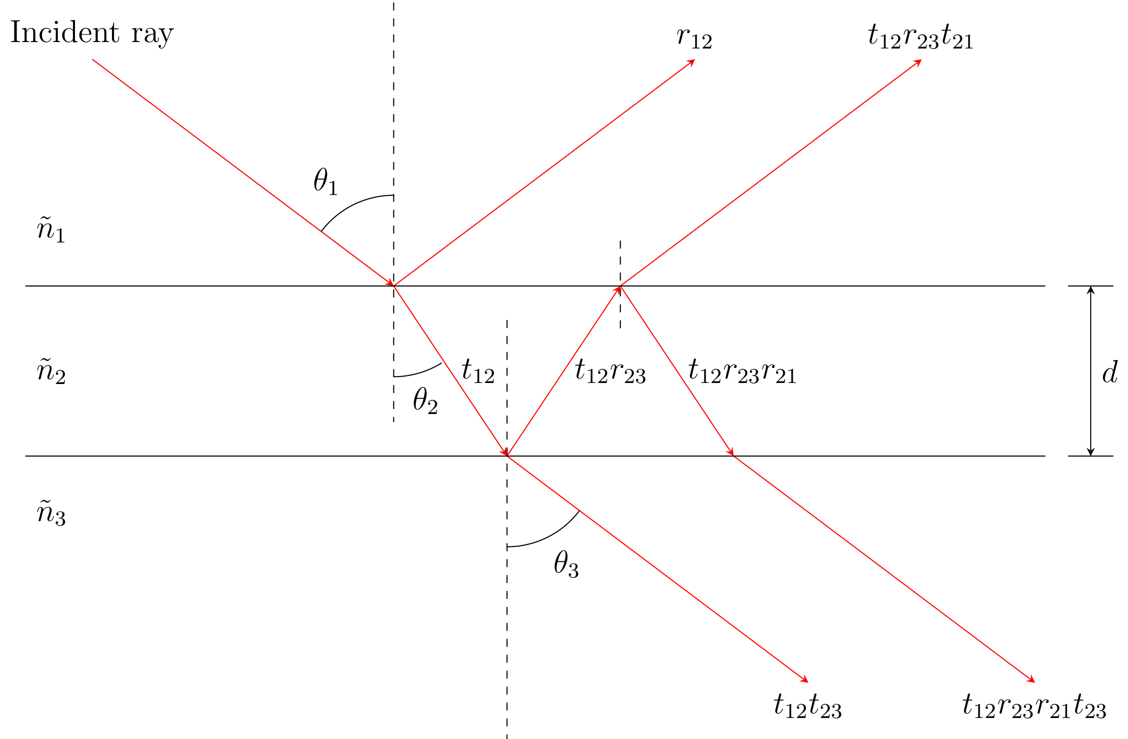

Figure 2.2 Geometry for analysis of reflection from a thin film.

more than the grating period Λ to study the energy properties of gratings—we need the geometrical structure and optical properties as well. Then we can solve Maxwell's equations for the particular situation and determine the diffraction efficiency into each scattered mode.

There are a variety of methods used to analyze electromagnetic diffraction from gratings [13, 14, 15]. In the proposed work, we will use the method of rigorous coupled-wave analysis (RCWA) described by Moharam, Gaylord, and co-workers [16, 17]. Moharam, Gaylord, and co-workers called their coupled-wave analysis "rigorous" because it provides a numerical solution to Maxwell's equations without making any theoretical approximations in its formulation. This distinguishes it from approximate coupled-wave analyses, such as Kogelnik's classic two-wave first-order coupled-wave analysis of volume holographic gratings [18]. The formulation of RCWA presented in [16] has convergence problems for TM polarization that were solved by a reformulation

that was discovered independently by Lalanne and Morris [19] and by Granet and Guizal [20]. The improved convergence of this reformulation was explained by Li [21].

2.2.1 Planar diffraction from binary gratings

In our experiments and simulations, the grating is in the planar diffraction configuration, which means that both the incident and reflected wavevectors lie in the plane formed by the normal vector to the grating and the grating vector (which points in the direction of the periodicity of the grating). We begin by formulating RCWA for binary gratings; later we will show how stacks of these gratings can be used to approximate surface-relief gratings. We follow the notation of Moharam, Gaylord, and co-workers [16] closely, albeit correcting the typographical errors and the convergence problems for TM polarization. A binary rectangular-groove grating is shown in Figure 2.3. The grating occupies an infinite slab region separating two half-spaces. The grating is illuminated by a monochromatic plane wave in half-space I propagating with wavevector $\boldsymbol{k}$. The light impinges upon the grating at an angle of incidence θ. We align the z-axis with the normal to half-space I and the x-axis with the periodicity of the grating.

The periodicity of the grating allows us to express the relative permittivity distribution of the grating as a Fourier series

$$\epsilon(x) = \sum_m \epsilon_m \exp\left(j\frac{2\pi m x}{\Lambda}\right) \tag{2.8}$$

where ϵ_m is the mth Fourier component of the permittivity distribution and Λ is the period of the grating. The relative permittivity distribution is related to the refractive index distribution $n(x)$ by the relation $\epsilon(x) = [n(x)]^2$. In particular the refractive index of a binary grating consists of alternating regions with refractive indices n_r

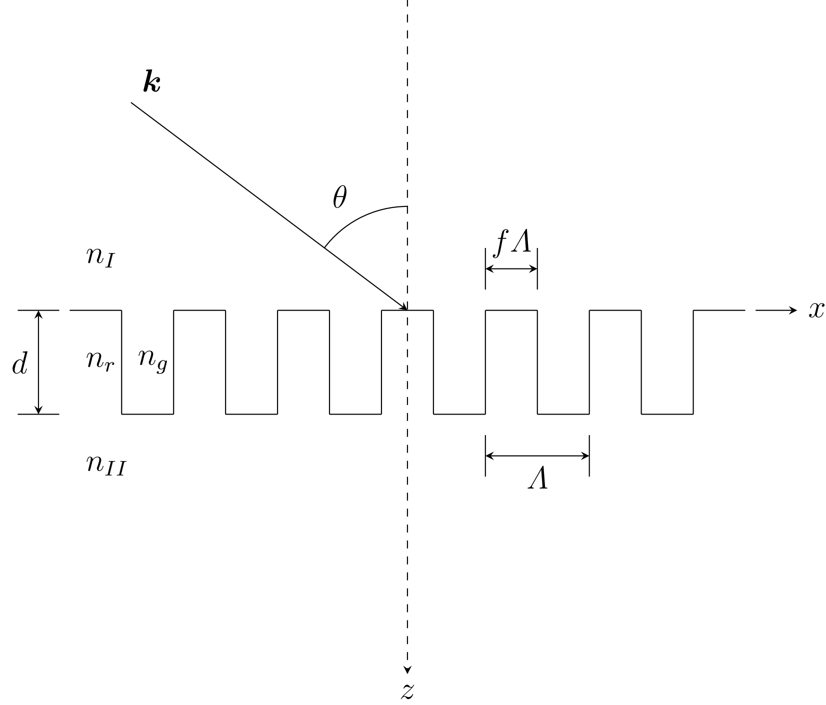

Figure 2.3 Geometry of the binary grating diffraction problem in the planar diffraction configuration.

(ridges) and n_g (grooves), in which case the Fourier coefficients are explicitly given by

$$\epsilon_m = \begin{cases} n_r^2 f + n_g^2(1-f), & m = 0 \\ \left(n_r^2 - n_g^2\right) \dfrac{\sin(\pi m f)}{\pi m}, & m \neq 0, \end{cases} \tag{2.9}$$

where f is the fraction of the period Λ occupied by the ridges.

For reasons that will become apparent later, we also need the Fourier series expansion of the reciprocal relative permittivity distribution

$$\tilde{\epsilon}(x) = \frac{1}{\epsilon(x)} = \sum_m \tilde{\epsilon}_m \exp\left(j\frac{2\pi m x}{\Lambda}\right). \tag{2.10}$$

The Fourier coefficients are given by

$$\tilde{\epsilon}_m = \begin{cases} \left(\frac{1}{n_r^2}\right) f + \left(\frac{1}{n_g^2}\right)(1-f), & m = 0 \\ \left(\frac{1}{n_r^2} - \frac{1}{n_g^2}\right) \dfrac{\sin(\pi m f)}{\pi m}, & m \neq 0. \end{cases} \tag{2.11}$$

The grating is illuminated by a plane wave at angle of incidence θ. In the TE case, the plane wave is described by the electric field

$$E_{\text{inc},y} = \exp[-jk_0 n_I (\sin\theta\, x + \cos\theta)\, z],$$

and in the TM case, the plane wave is described by the magnetic field

$$H_{\text{inc},y} = \exp[-jk_0 n_I (\sin\theta\, x + \cos\theta)\, z].$$

Incident and substrate regions

The periodicity of the grating allows the electric field in the incident and substrate regions to be expanded in an angular spectrum of plane waves satisfying the Floquet condition. In the TE case, we have

$$E_{I,y} = E_{\text{inc},y} + \sum_i R_i \exp[-j(k_{xi}x - k_{I,zi}z)],$$
$$E_{II,y} = \sum_i T_i \exp\{-j[k_{xi}x + k_{II,zi}(z-d)]\},$$

and in the TM case, we have

$$H_{I,y} = H_{\text{inc},y} + \sum_i R_i \exp[-j(k_{xi}x - k_{I,zi}z)],$$
$$H_{II,y} = \sum_i T_i \exp\{-j[k_{xi}x + k_{II,zi}(z-d)]\},$$

where R_i and T_i are the amplitude reflection and transmission, respectively, of the ith diffracted order,

$$k_{xi} = k_o \left[n_I \sin\theta - i \left(\frac{\lambda}{\Lambda_0} \right) \right],$$

and

$$k_{\ell,zi} = \begin{cases} +k_0 \sqrt{n_\ell^2 - \left(\frac{k_x i}{k_0}\right)^2}, & k_0 n_\ell > k_{xi}, \\ -jk_0 \sqrt{\left(\frac{k_x i}{k_0}\right)^2 - n_\ell^2}, & k_{xi} > k_0 n_\ell \end{cases}$$

where $\ell \in \{I, II\}$.

Grating region

The periodicity of the grating allows the electric and magnetic fields in the grating region can expanded into space-harmonic fields to satisfy Floquet's theorem (Bloch theorem in one dimension). In the TE case, we have

$$E_{gy} = \sum_i S_{yi}(z) \exp(-jk_{xi}x),$$
$$H_{gx} = -j\sqrt{\frac{\epsilon_0}{\mu_0}} \sum_i U_{xi}(z) \exp(-jk_{xi}x),$$

and in the TM case, we have

$$H_{gy} = \sum_i U_{yi}(z) \exp(-jk_{xi}x),$$
$$E_{gx} = j\sqrt{\frac{\mu_0}{\epsilon_0}} \sum_i S_{xi}(z) \exp(-jk_{xi}x),$$

where S_i and U_i are the normalized amplitudes of the ith space-harmonic electric and magnetic fields, respectively. The requirement that these fields satisfy Maxwell's equations results in a system of differential equations for the amplitudes of these

harmonics. In the TE case we have

$$\frac{\partial^2 \boldsymbol{S}_y}{\partial (z')^2} = \boldsymbol{A}\boldsymbol{S}_y, \tag{2.12}$$

where

$$\begin{aligned} z' &= k_0 z, \\ \boldsymbol{A} &= \boldsymbol{K}_x^2 - \boldsymbol{E}, \\ \boldsymbol{K}_x &= \text{a diagonal matrix with } K_{x,i,i} = k_{xi}/k_0, \\ \boldsymbol{E} &= \text{a matrix of permittivity harmonics } E_{i,p} = \epsilon_{(i-p)}. \end{aligned}$$

In the TM case Moharam, Gaylord, and co-workers [16] have

$$\frac{\partial^2 \boldsymbol{U}_y}{\partial (z')^2} = \boldsymbol{E}\boldsymbol{B}\boldsymbol{U}_y, \tag{2.13}$$

where $\boldsymbol{B} = \boldsymbol{K}_x \boldsymbol{E}^{-1} \boldsymbol{K}_x - \boldsymbol{I}$. This is a silent reformulation of the problem, because $\boldsymbol{B}$ should actually be defined $\boldsymbol{B} = \boldsymbol{K}_x \boldsymbol{P} \boldsymbol{K}_x - \boldsymbol{I}$, where $\boldsymbol{P}$ is a matrix of reciprocal permittivity harmonics $P_{i,p} = \tilde{\epsilon}_{(i-p)}$. This is a partial implementation of the refomulation of the problem by Lalanne and Morris [19] and by Granet and Guizal [20] that was subsequently explained by Li [21], which results in the matrix equation

$$\frac{\partial^2 \boldsymbol{U}_y}{\partial (z')^2} = \boldsymbol{P}^{-1}\boldsymbol{B}\boldsymbol{U}_y, \tag{2.14}$$

where

$$\boldsymbol{B} = \boldsymbol{K}_x \boldsymbol{E}^{-1} \boldsymbol{K}_x - \boldsymbol{I}. \tag{2.15}$$

The explanation for the improved convergence of the new TM formulation is as follows. In both the TE and TM formulations, we are trying to find a Fourier series or pseudo-Fourier series expansion for a function $h(x) = f(x)g(x)$ that is the product of

two other functions, and we are trying to find the Fourier coefficients h_n in terms of the Fourier coefficients f_n and g_n. When f and g are piecewise-continuous, piecewise-smooth, bounded periodic functions, the Fourier coefficients h_n can be obtained from f_n and g_n by *Laurent's rule*

$$h_n = \sum_{m=-\infty}^{\infty} f_{n-m} g_m = \sum_{m=-\infty}^{\infty} g_{n-m} f_m. \tag{2.16}$$

Then $h(x)$ has a Fourier factorization

$$h(x) = \sum_{n=-\infty}^{\infty} h_n \exp(jnx) = \sum_{n=-\infty}^{\infty} \sum_{m=-\infty}^{\infty} f_{n-m} g_m \exp(jnx).$$

The problem we are faced with here is whether Laurent's rule applies when the series are symmetrically truncated, that is, for a truncated Laurent's rule

$$h_n^{(M)} = \sum_{m=-M}^{M} f_{n-m} g_m, \tag{2.17}$$

whether the truncated Laurent's rule expansion

$$h^{(M)}(x) = \sum_{m=-M}^{M} h_n^{(M)} \exp(jnx) \tag{2.18}$$

converges to the truncated Fourier series expansion

$$h_M(x) = \sum_{m=-M}^{M} h_n \exp(jnx). \tag{2.19}$$

The truncated Laurent's rule can be written as a matrix-vector product if we construct a Toeplitz matrix $[\![f]\!]$ with elements $[\![f]\!]_{n,m} = f_{n-m}$ and a vector of Fourier coefficients $\boldsymbol{g}$, in which case we have

$$\boldsymbol{h} = [\![f]\!]\, \boldsymbol{g} = [\![g]\!]\, \boldsymbol{f}. \tag{2.20}$$

In the TE formulation, we have the product ϵE_{gy}, which is the product of a discontinuous function ϵ and a continuous function E_{gy}. This is what Li calls a *type 1 product*, that is, a product of two piecewise-smooth, bounded, periodic functions that have no concurrent jump discontinuities. When $h(x) = f(x)g(x)$ is a type 1 product, it can be Fourier factorized by Laurent's rule.

In the TM formulation, we have the products $\epsilon(x)E_{gx}$ and $\frac{1}{\epsilon(x)}\frac{\partial H_{gy}}{\partial x}$, which are both products of two piecewise-smooth, bounded, period functions that have only pairwise-complementary jump discontinuities. These are what Li call *type 2 products*, which cannot be Fourier factorized by Laurent's rule, but can be Fourier factorized by what Li calls the *inverse rule*:

$$\boldsymbol{h} = \left[\!\left[\frac{1}{f}\right]\!\right]^{-1}\boldsymbol{g}. \tag{2.21}$$

In words, wherever a Toeplitz matrix occurs in the product of Fourier coefficients, the convergence is improved by replacing it with the matrix inverse of a Toeplitz matrix of the reciprocal coefficients, i.e. $[\![f]\!] \to \left[\!\left[\frac{1}{f}\right]\!\right]^{-1}$. In the context of the grating problem, this means applying the substitutions $\boldsymbol{P} \to \boldsymbol{E}^{-1}$ and $\boldsymbol{E} \to \boldsymbol{P}^{-1}$. Moharam, Gaylord, and co-workers [16] had partially implemented this when they replaced what should have been $\boldsymbol{B} = \boldsymbol{K}_x\boldsymbol{P}\boldsymbol{K}_x - \boldsymbol{I}$ with $\boldsymbol{B} = \boldsymbol{K}_x\boldsymbol{E}^{-1}\boldsymbol{K}_x - \boldsymbol{I}$, and Lalanne and Morris [19] and Granet and Guizal [20] completed this when they reformulated

$$\frac{\partial^2 \boldsymbol{U}_y}{\partial(z')^2} = \boldsymbol{E}\boldsymbol{B}\boldsymbol{U}_y$$

as

$$\frac{\partial^2 \boldsymbol{U}_y}{\partial(z')^2} = \boldsymbol{P}^{-1}\boldsymbol{B}\boldsymbol{U}_y.$$

Grating region modes

We can express the amplitudes of the space-harmonics in terms of the eigenvalues and eigenvectors of the system of differential equations. These amplitudes are the modes of the grating region (which is why RCWA is sometimes referred to as the "Fourier modal method"), and the mode amplitudes are to be determined by the boundary conditions. In the TE case and TM cases, we find the eigenvalues q_m^2 and eigenvectors $\boldsymbol{w}_m$ of $\boldsymbol{A}$ and $\boldsymbol{B}$, respectively. In both cases, we form the matrices

$$\begin{aligned}
\boldsymbol{Q} &= \text{a diagonal matrix with elements } q_m\text{, which are the} \\
&\quad\ \text{positive square roots of the eigenvalues of } \boldsymbol{A} \text{ or } \boldsymbol{B}, \\
\boldsymbol{W} &= \text{a matrix with elements } w_{i,m}\text{, which is the } i\text{th element} \\
&\quad\ \text{of the eigenvector } \boldsymbol{w}_m \text{ corresponding to eigenvalue } q_m, \\
\boldsymbol{V} &= \begin{cases} \boldsymbol{WQ} & \text{(TE)}, \\ \boldsymbol{PWQ} & \text{(TM)}. \end{cases}
\end{aligned}$$

The definition $\boldsymbol{V} = \boldsymbol{PWQ}$ in the TM case replaces Moharam, Gaylord, and co-workers' definition $\boldsymbol{V} = \boldsymbol{E}^{-1}\boldsymbol{WQ}$ [16] to complete the convergence correction for the TM case.

Boundary counditions

We solve for the reflected and transmitted amplitudes in the incident and substrate media, respectively, and also for the mode amplitudes in the grating region by enforcing the electromagnetic boundary conditions at the interfaces separating these regions. The electromagnetic boundary conditions result in a system of linear equations which can be solved by standard numerical methods. In the TE case, we have at the incident

boundary ($z = 0$)

$$\begin{bmatrix} \delta_{i0} \\ jn_I \cos\theta\, \delta_{i0} \end{bmatrix} + \begin{bmatrix} \boldsymbol{I} \\ -j\boldsymbol{Y}_I \end{bmatrix} \boldsymbol{R} = \begin{bmatrix} \boldsymbol{W} & \boldsymbol{WX} \\ \boldsymbol{V} & -\boldsymbol{VX} \end{bmatrix} \begin{bmatrix} \boldsymbol{c}^+ \\ \boldsymbol{c}^- \end{bmatrix},$$

and at the substrate boundary ($z = d$), we have

$$\begin{bmatrix} \boldsymbol{WX} & \boldsymbol{W} \\ \boldsymbol{VX} & -\boldsymbol{V} \end{bmatrix} \begin{bmatrix} \boldsymbol{c}^+ \\ \boldsymbol{c}^- \end{bmatrix} = \begin{bmatrix} \boldsymbol{I} \\ -j\boldsymbol{Y}_{II} \end{bmatrix} \boldsymbol{T},$$

where

$$\delta_{i0} = \begin{cases} 1 & i = 0 \\ 0 & i \neq 0 \end{cases}$$

$$\boldsymbol{X} = \text{a diagonal matrix with } X_{i,i} = \exp(-k_0 q_m d),$$

$$\boldsymbol{Y}_I = \text{a diagonal matrix with } Y_{I,i,i} = (k_{I,zi}/k_0),$$

$$\boldsymbol{Y}_{II} = \text{a diagonal matrix with } Y_{II,i,i} = (k_{II,zi}/k_0).$$

In the TM case, we have at the incident boundary

$$\begin{bmatrix} \delta_{i0} \\ j \cos\theta\, \delta_{i0}/n_I \end{bmatrix} + \begin{bmatrix} \boldsymbol{I} \\ -j\boldsymbol{Z}_I \end{bmatrix} \boldsymbol{R} = \begin{bmatrix} \boldsymbol{W} & \boldsymbol{WX} \\ \boldsymbol{V} & -\boldsymbol{VX} \end{bmatrix} \begin{bmatrix} \boldsymbol{c}^+ \\ \boldsymbol{c}^- \end{bmatrix},$$

and at the substrate boundary, we have

$$\begin{bmatrix} \boldsymbol{WX} & \boldsymbol{W} \\ \boldsymbol{VX} & -\boldsymbol{V} \end{bmatrix} \begin{bmatrix} \boldsymbol{c}^+ \\ \boldsymbol{c}^- \end{bmatrix} = \begin{bmatrix} \boldsymbol{I} \\ j\boldsymbol{Z}_{II} \end{bmatrix} \boldsymbol{T},$$

where

$$\boldsymbol{Z}_I = \text{a diagonal matrix with } Z_{I,i,i} = (k_{I,zi}/k_0 n_I^2),$$
$$\boldsymbol{Z}_{II} = \text{a diagonal matrix with } Z_{II,i,i} = (k_{II,zi}/k_0 n_{II}^2).$$

2.2.2 Planar diffraction from surface-relief gratings

Moharam, Gaylord and co-workers [17], among others, have extend the formulation of RCWA for binary gratings to surface-relief gratings of essentially arbitrary topography. This extension is achieved by discretizing the grating into a stack of binary gratings. The geometry is illustrated in figure 2.4. The key to computational implementation of this scheme is to choose an algorithm for boundary matching that is numerically stable and efficient. Several algorithms have been reported, including the enhanced transmittance matrix (T-matrix) approach [17], the scattering matrix (S-matrix) algorithm [22], and the R-matrix algorithm [23]. In this work, we will use the enhanced transmittance matrix approach.

The enhanced transmittance matrix approach is based on the standard transmittance matrix approach, which matches the boundary conditions from the incident medium to the substrate medium through the layers $\ell \in \{1, 2, \ldots, L\}$. In the TE case, we have the equation

$$\begin{bmatrix} \delta_{i0} \\ j n_I \cos\theta\, \delta_{i0} \end{bmatrix} + \begin{bmatrix} \boldsymbol{I} \\ -j\boldsymbol{Y}_I \end{bmatrix} \boldsymbol{R} = \prod_{\ell=1}^{L} \begin{bmatrix} \boldsymbol{W}_\ell & \boldsymbol{W}_\ell \boldsymbol{X}_\ell \\ \boldsymbol{V}_\ell & -\boldsymbol{V}_\ell \boldsymbol{X}_\ell \end{bmatrix} \begin{bmatrix} \boldsymbol{W}_\ell \boldsymbol{X}_\ell & \boldsymbol{W}_\ell \\ \boldsymbol{V}_\ell \boldsymbol{X}_\ell & -\boldsymbol{V}_\ell \end{bmatrix}^{-1} \begin{bmatrix} \boldsymbol{I} \\ j\boldsymbol{Y}_{II} \end{bmatrix} \boldsymbol{T},$$

and in the TM case, we have the equation

$$\begin{bmatrix} \delta_{i0} \\ j \cos\theta\, \delta_{i0}/n_I \end{bmatrix} + \begin{bmatrix} \boldsymbol{I} \\ -j\boldsymbol{Z}_I \end{bmatrix} \boldsymbol{R} = \prod_{\ell=1}^{L} \begin{bmatrix} \boldsymbol{W}_\ell & \boldsymbol{W}_\ell \boldsymbol{X}_\ell \\ \boldsymbol{V}_\ell & -\boldsymbol{V}_\ell \boldsymbol{X}_\ell \end{bmatrix} \begin{bmatrix} \boldsymbol{W}_\ell \boldsymbol{X}_\ell & \boldsymbol{W}_\ell \\ \boldsymbol{V}_\ell \boldsymbol{X}_\ell & -\boldsymbol{V}_\ell \end{bmatrix}^{-1} \begin{bmatrix} \boldsymbol{I} \\ j\boldsymbol{Z}_{II} \end{bmatrix} \boldsymbol{T},$$

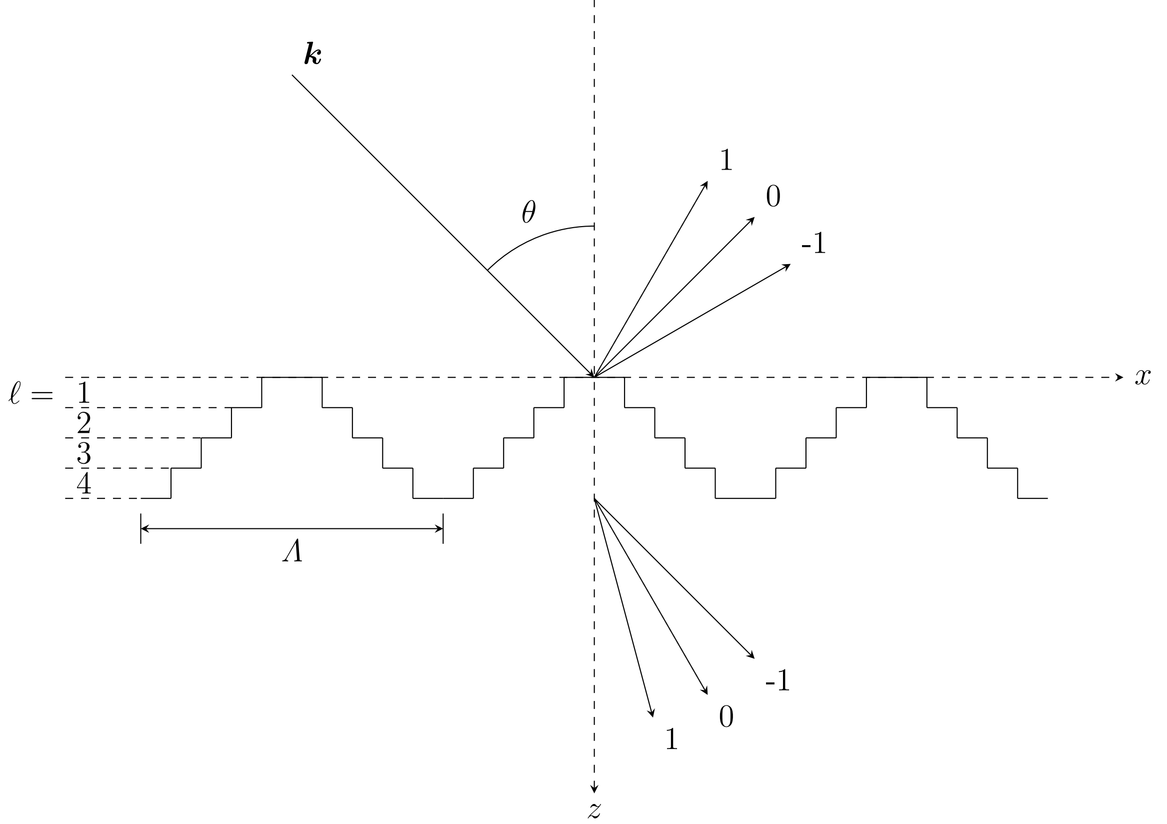

Figure 2.4 Geometry for representing a surface-relief grating as a stack of 4 binary gratings.

Direct solution of these equations, as written, is susceptible to numerical instability because the eigenvalues $q_{\ell,m}$ that enter into the matrix $\boldsymbol{X}_\ell$ tend to be complex-valued with positive real parts. When the real part of $q_{\ell,m}$ is large and positive, the corresponding element $\exp(-k_0 q_{\ell,m} d_\ell)$ of the diagonal matrix $\boldsymbol{X}_\ell$ will be very small. This results in one or more columns of the matrix being inverted being virtually zero, which may cause numerical failure or serious error in the matrix inversion routine.

The enhanced transmittance matrix approach stabilizes the numerical procedure by factoring this numerically unstable matrix at each layer. Without loss of generality, we will present the approach for the TM case. We motivate the approach by considering the matrices for the last term in the matrix product, which correspond to solving the boundary conditions for matrix $\ell = L$. If we define $\boldsymbol{f}_{L+1} = \boldsymbol{I}$ and $\boldsymbol{g}_{L+1} = j\boldsymbol{Z}_{II}$ and

factor the ill-conditioned matrix inverse, then we have

$$\begin{bmatrix} \boldsymbol{W}_L & \boldsymbol{W}_L\boldsymbol{X}_L \\ \boldsymbol{V}_L & -\boldsymbol{V}_L\boldsymbol{X}_L \end{bmatrix} \begin{bmatrix} \boldsymbol{W}_L\boldsymbol{X}_L & \boldsymbol{W}_L \\ \boldsymbol{V}_L\boldsymbol{X}_L & -\boldsymbol{V}_L \end{bmatrix}^{-1} \begin{bmatrix} \boldsymbol{f}_{L+1} \\ \boldsymbol{g}_{L+1} \end{bmatrix} \boldsymbol{T}$$
$$= \begin{bmatrix} \boldsymbol{W}_L & \boldsymbol{W}_L\boldsymbol{X}_L \\ \boldsymbol{V}_L & -\boldsymbol{V}_L\boldsymbol{X}_L \end{bmatrix} \begin{bmatrix} \boldsymbol{X}_L & 0 \\ 0 & \boldsymbol{I} \end{bmatrix}^{-1} \begin{bmatrix} \boldsymbol{W}_L & \boldsymbol{W}_L \\ \boldsymbol{V}_L & -\boldsymbol{V}_L \end{bmatrix}^{-1} \begin{bmatrix} \boldsymbol{f}_{L+1} \\ \boldsymbol{g}_{L+1} \end{bmatrix} \boldsymbol{T} \quad (2.22)$$

We have factored the ill-conditioned matrix inverse into the product of two matrix inverses, one of which is well-conditioned (the matrix containing blocks of $\boldsymbol{W}_\ell$ and $\boldsymbol{V}_\ell$, and one of which is still ill-conditioned when the elements of the diagonal matrix $\boldsymbol{X}_\ell$ are small. At this point, we introduce

$$\begin{bmatrix} \boldsymbol{a}_L \\ \boldsymbol{b}_L \end{bmatrix} = \begin{bmatrix} \boldsymbol{W}_L & \boldsymbol{W}_L \\ \boldsymbol{V}_L & -\boldsymbol{V}_L \end{bmatrix}^{-1} \begin{bmatrix} \boldsymbol{f}_{L+1} \\ \boldsymbol{g}_{L+1} \end{bmatrix},$$

so we can write the matrix product for layer $\ell = L$ as

$$\begin{bmatrix} \boldsymbol{W}_L & \boldsymbol{W}_L\boldsymbol{X}_L \\ \boldsymbol{V}_L & -\boldsymbol{V}_L\boldsymbol{X}_L \end{bmatrix} \begin{bmatrix} \boldsymbol{X}_L & 0 \\ 0 & \boldsymbol{I} \end{bmatrix}^{-1} \begin{bmatrix} \boldsymbol{a}_L \\ \boldsymbol{b}_L \end{bmatrix} \boldsymbol{T}.$$

Now we stabilize the inversion of the diagonal matrix containing $\boldsymbol{X}_L$. Since this matrix is diagonal, we can perform the inversion analytically and find that

$$\begin{bmatrix} \boldsymbol{X}_L & 0 \\ 0 & \boldsymbol{I} \end{bmatrix}^{-1} = \begin{bmatrix} \boldsymbol{X}_L^{-1} & 0 \\ 0 & \boldsymbol{I} \end{bmatrix}$$

but there is still the problem of representing the diagonal elements of the inverse matrix accurately with finite precision and the possibility of truncation errors. We achieve this by introduction the substitution $\boldsymbol{T} = \boldsymbol{a}_L^{-1}\boldsymbol{X}_L\boldsymbol{T}_L$. Now we introduce $\boldsymbol{f}_L$ and

$\boldsymbol{g}_L$ so we can write the matrix product for layer $\ell = L$ as

$$\begin{bmatrix} \boldsymbol{f}_L \\ \boldsymbol{g}_L \end{bmatrix} \boldsymbol{T}_L = \begin{bmatrix} \boldsymbol{W}_L & \boldsymbol{W}_L \boldsymbol{X}_L \\ \boldsymbol{V}_L & -\boldsymbol{V}_L \boldsymbol{X}_L \end{bmatrix} \begin{bmatrix} \boldsymbol{I} \\ \boldsymbol{b}_L \boldsymbol{a}_L^{-1} \boldsymbol{X}_L \end{bmatrix} \boldsymbol{T}_L$$

Repeating this process for all layers, we can write the transmittance matrix equation as

$$\begin{bmatrix} \delta_{i0} \\ j\cos\theta\,\delta_{i0}/n_I \end{bmatrix} + \begin{bmatrix} \boldsymbol{I} \\ -j\boldsymbol{Z}_I \end{bmatrix} \boldsymbol{R} = \begin{bmatrix} \boldsymbol{f}_1 \\ \boldsymbol{g}_1 \end{bmatrix} \boldsymbol{T}_1,$$

where

$$\boldsymbol{T} = \left(\prod_{\ell=1}^{L} \boldsymbol{a}_\ell^{-1} \boldsymbol{X}_\ell \right) \boldsymbol{T}_1$$

We can now outline the implementation of the enhanced transmittance matrix algorithm.

1. Set $\boldsymbol{f}_{L+1} = \boldsymbol{I}$.
2. Set

$$\boldsymbol{g}_{L+1} = \begin{cases} -j\boldsymbol{Y}_{II} & \text{TE}, \\ J\boldsymbol{Z}_{II} & \text{TM}. \end{cases}$$

3. Starting from layer $\ell = L$ and working up to layer $\ell = 1$:
   (a) Calculate

$$\begin{bmatrix} \boldsymbol{a}_\ell \\ \boldsymbol{b}_\ell \end{bmatrix} = \begin{bmatrix} \boldsymbol{W}_\ell & \boldsymbol{W}_\ell \\ \boldsymbol{V}_\ell & -\boldsymbol{V}_\ell \end{bmatrix}^{-1} \begin{bmatrix} \boldsymbol{f}_{\ell+1} \\ \boldsymbol{g}_{\ell+1} \end{bmatrix}.$$

   (b) Calculate

$$\begin{bmatrix} \boldsymbol{f}_\ell \\ \boldsymbol{g}_\ell \end{bmatrix} = \begin{bmatrix} \boldsymbol{W}_\ell & \boldsymbol{W}_\ell \boldsymbol{X}_\ell \\ \boldsymbol{V}_\ell & -\boldsymbol{V}_\ell \boldsymbol{X}_\ell \end{bmatrix} \begin{bmatrix} \boldsymbol{I} \\ \boldsymbol{b}_\ell \boldsymbol{a}_\ell^{-1} \boldsymbol{X}_\ell \end{bmatrix}$$

4. Solve

$$\begin{bmatrix} \delta_{i0} \\ j\cos\theta\,\delta_{i0}/n_I \end{bmatrix} + \begin{bmatrix} \boldsymbol{I} \\ -j\boldsymbol{Z}_I \end{bmatrix} \boldsymbol{R} = \begin{bmatrix} \boldsymbol{f}_1 \\ \boldsymbol{g}_1 \end{bmatrix} \boldsymbol{T}_1,$$

   for the desired amplitudes $\boldsymbol{R}$ and/or $\boldsymbol{T}_1$. If the transmitted amplitudes are desired, use $\boldsymbol{T}_1$ to calculate

$$\boldsymbol{T} = \left(\prod_{\ell=1}^{L} \boldsymbol{a}_\ell^{-1} \boldsymbol{X}_\ell \right) \boldsymbol{T}_1.$$

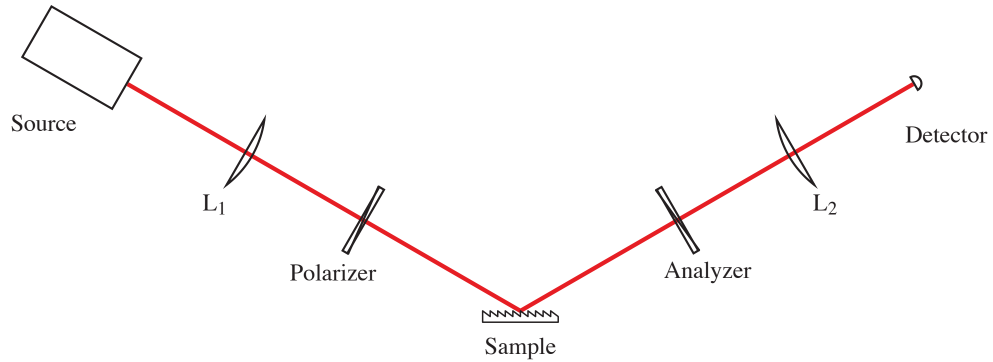

Figure 2.5 Schematic of a basic ellipsometer operating in the reflection mode. Light from a source is collimated by optics L_1, passes through a polarization state generator, and reflects from the sample. The reflected light passes through a polarization state analyzer, and is focused by optics L_2 onto a detector.

2.3 Data collection: Ellipsometry

In this work, we will use ellipsometry to collect experimental optical scattering data. Ellipsometry is a polarization-sensitive optical measurement technique. It uses the differences in the optical response for different polarizations to deduce information about an object. The basic operating principle of ellipsometry was developed by Drude [24, 25], and the instrument that Drude developed was given the name "ellipsometer" by Rothen [26]. Ellipsometry was originally applied to the measurement of interfaces and thin films, but it has also been applied to gratings, rough surfaces, and other structures. In this work, we use ellipsometry in the reflection mode, therefore we will describe the technique in that context.

Figure 2.5 illustrates the basic configuration of an ellipsometer operating in the reflection mode. Light is collimated and passes through a polarization state generator. For simplicity, we will initially assume that the light is monochromatic; later, we will consider the polychromatic case. It reflects from the sample and passes through a polarization state analyzer. The transmitted light is focused onto a detector, which measures the intensity.

In the reflection mode, ellipsometry determines the amplitude of the total reflection

coefficients R_p of the p-polarization and R_s of the s-polarization from the observable total power reflection coefficients $\mathcal{R}_p = |R_p|^2$ and $\mathcal{R}_s = |R_s|^2$. The total reflection coefficients depend on the optical properties of the sample and ambient medium, and the structure of the sample, particularly any structural features comparable to the effective wavelength of the light impinging upon them.

We use complex numbers to represent the total reflection coefficients since an object can affect the amplitude or phase of the electromagnetic waves that are reflected from them. Then the ratio R_p/R_s is generally complex-valued, and can be represented in complex-exponential form as

$$\frac{R_p}{R_s} = xe^{jy}$$

where x and y are real numbers and $j = \sqrt{-1}$.

There are several alternative representations of the complex-valued ratio R_p/R_s [27, sections 1.5 and 2.4.2]. One is the $(\varPsi, \varDelta)$ format, defined by

$$(\tan \varPsi)e^{j\varDelta} = \frac{R_p}{R_s} \tag{2.23}$$

The quantities $\varPsi$ and $\varDelta$ originate from the technique of *null ellipsometry*, which is illustrated below. We follow the exposition of Tompkins [27, section 2.3]. The polarizer consists of a rotatable linear polarizer followed by a quarter-wave plate (abbreviated QWP and frequently referred to as the *compensator*) set at 45° with respect to the plane of incidence. The analyzer consists of a rotatable linear polarizer. The measurement principle is that the polarizer is rotated to an angle P such that the polarizer and compensator generate an elliptical polarization state that the sample converts into linearly polarized light. The analyzer is then rotated to an angle A such that it extinguishes this linearly polarized light (the *null*). All angles are measured positive counterclockwise from the plane of incidence when looking into the beam. There are multiple combinations of the polarizer and analyzer angles in the transverse

plane that will give the null, so we define several ellipsometric zones within which the null angles are unique. For the configuration under consideration, it is typical to use measurements in zones 2 and 4, defined as

Zone 2:	$-45° < P_2 < 135°$	$0° < A_2 < 90°$	QWP $= 45°$
Zone 4:	$-135° < P_4 < 455°$	$-90° < A_4 < 0°$	QWP $= 45°$

Then the zone estimates for Δ and Ψ are given by

$$\Delta_2 = 270° - 2P_2 \qquad \Delta_4 = 90° - 2P_4$$

$$\Psi_2 = A_2 \qquad \Psi_4 = -A_4$$

If the compensator is ideal, either zone can be used individually to estimate Δ and Ψ. In the presence of compensator or other errors, averaging the two zone estimates can cancel out errors due to inexact compensation.

In our work, we use a Sopra GESP-5 rotating-polarizer ellipsometer. For rotating-element ellipsometers, it is convenient to represent ellipsometric quantities in (α, β) format, which is related to (Ψ, Δ) format by the relations

$$\alpha = -\cos(2\Psi) \qquad \beta = \sin(2\Psi)\cos\Delta.$$

For a rotating-polarizer ellipsometer, the quantities α and β are the Fourier coefficients of the intensity signal

$$I(t) = I_0\{1 + \alpha\cos[2P'(t)] + \beta\sin[2P'(t)]\}$$

where $P'(t) = 2\pi ft + P_c$ describes the angle from the sample p direction to the

polarizer transmission axis, measured in a counterclockwise positive direction looking toward the source, as a function of time [28]. We can calculate $\tan\Psi$ and $\cos\Delta$ from these Fourier coefficients using the formulae

$$\tan\Psi = \left|\sqrt{\frac{1+\alpha}{1-\alpha}}\right| |\tan A'|$$
$$\cos\Delta = \beta\left|\sqrt{\frac{1}{1-\alpha^2}}\right|,$$

where A' is angle from the sample p direction to the analyzer transmission axis, measured in a counterclockwise positive direction looking toward the source.

2.3.1 Spectroscopic ellipsometry

As mentioned in the previous section, the total reflection coefficients R_p and R_s may depend both on the optical properties of the sample and ambient medium and any structural features of the sample that are sensitive to the effective wavelength. These, in turn, generally depend on the frequency of the incident radiation, which suggests that by probing the sample with additional information may reveal additional information about the sample structure and the optical properties of the sample or ambient medium (or both). This is the premise of spectroscopic ellipsometry [12]. Most spectroscopic ellipsometers use an arc lamp as the light source in order to provide significant energy over a broad range of frequencies. The spectrum of the reflected light is measured either by using a scanning monochrometer to select narrow frequency bands to excite a single photodetector, or be using a fixed dispersive element (for example, a diffraction grating or a prism) to disperse the light onto an array of photodetectors.

2.3.2 Immersion ellipsometry

Ellipsometry may be performed on a sample in an ambient environment other than atmosphere by enclosing the sample in a cell with windows that allow the polarizer and analyzer beam to pass through them. McCrackin and co-workers [29] noted the use of sample cells to enable ellipsometer measurements in vacuum and gaseous environments and under liquids, and described the cell which they used for measurements under liquids. This describes the usual case for immersion ellipsometry where the ambient environment is an unavoidable consequence of the sample or process being measured, as often arises in biology or electrochemistry. Deliberate immersion in index-matching fluids in order to optically remove thin films was proposed by Moy [30] and has been used widely by Irene and co-workers [31, 32].

2.4 Data analysis

2.4.1 Data fitting: Levenberg-Marquardt regression

Two approaches have been described for determining the grating parameters that best match the measured data. The earliest approaches to scatterometry [11] generated a database of scattering signatures for various choices for each of the grating parameters. The most prominent drawback to this approach is that the database has to be pre-computed, which can be time-consuming, and that changing the model requires re-computing the entire database.

The other approach is to use an optimization routine such as a genetic algorithm or the Levenberg-Marquardt algorithm [33, 34] to search for the parameters that best match the experimental data. One apparent advantage of optimization methods is that they do not require a pre-computed database, and therefore can immediately be applied to different models for the grating topography. The disadvantages include

possible slow convergence or convergence that is sensitive to starting conditions. In this work, we will use Levenberg-Marquardt nonlinear regression.

We follow the exposition of the Levenberg-Marquardt regression in Press *et al.*[35, chapter 15]. In Levenberg-Marquardt regression, we attempt to minimize the goodness of fit χ^2 for the experimental data y_i with respect to a model $y(x \mid \boldsymbol{p})$ that depends on regression parameters $\boldsymbol{p} = \begin{bmatrix} p_1 & p_2 & \dots & p_M \end{bmatrix}^T$:

$$\chi^2(\boldsymbol{p}) = \sum_i \left\{ \frac{[y_i - y(x_i \mid \boldsymbol{p})]^2}{\sigma_i^2} \right\}.$$

The minimum of the goodness of fit as a function of the model parameters $\boldsymbol{p}$ occurs when

$$\nabla \chi^2(\boldsymbol{p}) = \mathbf{0}.$$

Levenberg-Marquardt is a hybrid regression method that combines gradient-search regression and a quasi-Newton method. For any arbitrary choice of the regression parameters $\boldsymbol{p}_0$, the gradient $\nabla_{\boldsymbol{p}} \chi^2(\boldsymbol{p}_0)$ points in the direction of most rapid increase in χ^2, therefore $-\nabla_{\boldsymbol{p}} \chi^2(\boldsymbol{p}_0)$ points in the direction of most rapid decrease. Thus we could iteratively improve an initial guess $\boldsymbol{p}_0$ for the regression parameters $\boldsymbol{p}$ by adding a multiple of the local downhill gradient $-\nabla_{\boldsymbol{p}} \chi^2(\boldsymbol{p}_0)$. This is the basis of gradient-search regression. The difficulty with gradient-search regression is choosing the multiple of the local downhill gradient, and the downhill gradient does not generally point directly from the current guess for the regression parameters to the minimum. Gradient-search tends to converge quickly when the current guess is far from the minimum, and slowly near the minimum.

Suppose we approximated χ^2 by a quadratic form

$$\chi^2(\boldsymbol{p}_0) \approx \gamma - \boldsymbol{b}^T \cdot \boldsymbol{p}_0 + \frac{1}{2} \boldsymbol{p}_0^T \boldsymbol{A} \, \boldsymbol{p}_0$$

where $\boldsymbol{b} = \nabla_{\boldsymbol{p}} \chi^2(\boldsymbol{p}_0)$ and $\boldsymbol{A}$ is the Hessian matrix for χ^2 with elements

$$A_{kl} = \frac{\partial^2 \chi^2(\boldsymbol{p}_0)}{\partial p_k \partial p_l}.$$

If this approximation is good, we can jump immediately from the current guess $\boldsymbol{p}_0$ to the minimizing parameters

$$\boldsymbol{p}_{\min} = \boldsymbol{p}_0 + \boldsymbol{A}^{-1}[-\nabla \chi^2(\boldsymbol{p}_0)].$$

Quasi-Newton methods are based on applying this principle using approximations to the Hessian. The iterates for $\boldsymbol{p}$ tend to converge quickly when the current estimate is near the minimum and the χ^2 function is well-approximated by a quadratic form, and slowly far from the minimum.

Levenberg-Marquardt switches between gradient-search when the magnitude of the gradient of χ^2 is large (far from the minimum) and a quasi-Newton approach when the gradient is small (near the minimum). The gradient of χ^2 has components

$$\frac{\partial \chi^2}{\partial p_k} = -2 \sum_i \frac{y_i - y(x_i \mid \boldsymbol{p})}{\sigma_i^2} \frac{\partial y(x_i \mid \boldsymbol{p})}{\partial p_k}.$$

The second derivatives of χ^2 are

$$\frac{\partial^2 \chi^2}{\partial p_k \partial p_l} = 2 \sum_i \frac{1}{\sigma_i^2} \left[\frac{\partial y(x_i \mid \boldsymbol{p})}{\partial p_k} \frac{\partial y(x_i \mid \boldsymbol{p})}{\partial p_l} - [y_i - y(x_i \mid \boldsymbol{p})] \frac{\partial^2 y(x_i \mid \boldsymbol{p})}{\partial p_k \partial p_l} \right].$$

It is conventional to eliminate the factors of 2 by defining

$$\beta_k = -\frac{1}{2} \frac{\partial \chi^2}{\partial p_k}, \qquad \alpha_{kl} = \frac{1}{2} \frac{\partial^2 \chi^2}{\partial p_k \partial p_l},$$

where $\boldsymbol{\beta} = -\frac{1}{2} \nabla \chi^2(\boldsymbol{p})$ and $\boldsymbol{\alpha} = \frac{1}{2} \boldsymbol{A}$ is called the *curvature matrix.*

With these definitions, the quasi-Newton update formula can be written as

$$\boldsymbol{\alpha}\,\boldsymbol{\delta p} = \boldsymbol{\beta},$$

At this point, we note that the exact second derivatives of χ^2 depend on both the first and second derivatives of the model $y(x \mid \boldsymbol{p})$. It is conventional to neglect the second derivatives of the model $\partial^2 y(x \mid \boldsymbol{p})/\partial p_k \partial p_l$ because they tend to be small, and they can destabilize the algorithm if the model fits badly or the data contain outliers. Then the elements of the curvature matrix are

$$\alpha_{kl} = \sum_i \frac{1}{\sigma_i^2} \left[\frac{\partial y(x_i \mid \boldsymbol{p})}{\partial p_k} \frac{\partial y(x_i \mid \boldsymbol{p})}{\partial p_l} \right].$$

The gradient-search update formula can be written in the form

$$\delta p_k = c_k \beta_k,$$

where c_k is a scaling constant for the kth component of the gradient. Levenberg-Marquardt scales each component using the diagonal elements of the curvature matrix α_{kk} and an adjustable scaling constant λ:

$$\delta p_k = \frac{1}{\lambda \alpha_{kk}} \beta_k.$$

The Levenberg-Marquardt method combines these two formulas by defining a new matrix

$$\boldsymbol{\alpha}' = \boldsymbol{\alpha} + \lambda \boldsymbol{I}.$$

and using the update formula

$$\boldsymbol{\alpha}'\,\boldsymbol{\delta p} = \boldsymbol{\beta}.$$

When λ is large, $\boldsymbol{\alpha}'$ is diagonally dominant, and the method takes a step that is

primarily determined by gradient search. When λ is small, $\boldsymbol{\alpha}'$ is approximately equal to the curvature matrix, and the method takes a quasi-Newton step.

We can now outline the Levenberg-Marquardt algorithm in its entirety. Given an initial estimate for the regression parameters $\boldsymbol{p}$:

1. Compute $\chi^2(\boldsymbol{p})$.
2. Pick an initial value for λ, e.g. $\lambda = 0.001$.
3. While the stopping criterion is not met, perform the following steps repeatedly:
   (a) Solve $\boldsymbol{\alpha}'\,\boldsymbol{\delta p} = \boldsymbol{\beta}$ for $\boldsymbol{\delta p}$ and evaluate $\chi^2(\boldsymbol{p} + \boldsymbol{\delta p})$.
   (b) If $\chi^2(\boldsymbol{p} + \boldsymbol{\delta p}) \geq \chi^2(\boldsymbol{p})$,
      - increase λ (e.g. by setting $\lambda \leftarrow 10\lambda$),

      otherwise,
      - decrease λ (e.g. by setting $\lambda \leftarrow \lambda/10$), and
      - update the estimate by setting $\boldsymbol{p} \leftarrow \boldsymbol{p} + \boldsymbol{\delta p}$.

There are many reasonable choices for stopping criterion. Convergence to machine precision is overkill, since we are at best obtaining a statistical estimate of the regression parameters $\boldsymbol{p}$, so small changes in χ^2 are not statistically meaningful. Furthermore, the algorithm should be permitted to continue while χ^2 increases more than trivially, because it means that the current value of λ is suboptimal. A typical criterion is to stop when either the absolute or relative decrease in χ^2 is less than 0.001.

Once the algorithm has stopped, we can estimate the standard errors of the fitted parameters $\boldsymbol{p}$ by setting $\lambda = 0$ and computing the covariance matrix

$$\boldsymbol{C} = \boldsymbol{\alpha}^{-1}.$$

Then standard error for the parameter p_k is given by

$$\sigma_k = \sqrt{C_{kk}}.$$

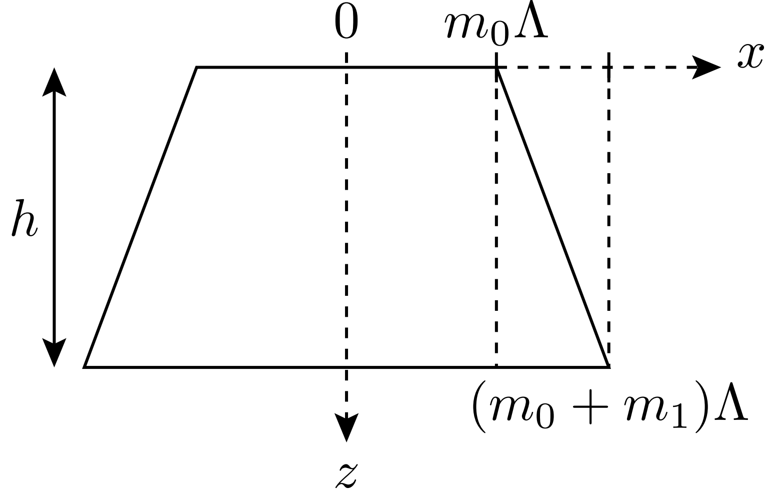

Figure 2.6 Illustrating the trapezoidal parameterization of grating profiles.

2.4.2 Grating profile parameterization

To keep the number of regression parameters managable, we parameterize grating profiles as a stack of trapezoids, with the line boundary x as a function of depth z of the ith trapezoid being described by

$$x(z) = \left[m_{i0} + m_{i1}\left(\frac{z}{h_i}\right)\right]\Lambda,$$

where m_{i0} is the normalized width, m_{i1} is the normalized sidewall slope, and h_i is the normalized height of the ith trapezoid. This geometry is illustrated in figure 2.6. The stack of trapezoids can then be sliced into a stack of binary gratings for RCWA simulation.

Chapter 3

Immersion scatterometry: preliminary results

This chapter describes our work demostrating the viability of liquid-immersion scatterometry [5]. There is some precedent for the idea of using liquid-immersion in optical measurement in gratings. Lu *et al.*[36] reported immersion diffractometry, which used a Littrow configuration to measure the pitch of diffraction gratings. A patent application by ASML [37] also suggests the possibility of performing the measurements under liquid immersion. This thesis is an experimental follow-up to a proposal and simulation study by Terry and Bendik to perform scatterometry in immersion to improve feature resolution [38].

To demonstrate and assess the viability of these methods, we use water as the immersion medium. Water is an attractive choice for the immersion medium because it is already used in many microelectronic fabrication and measurement processes, and in particular has been used as an immersion medium to improve the performance of optical lithography [39].

3.1 Materials and methods

3.1.1 Samples

Silicon wafers with a uniform SiO_2 film were used for reference measurements. Two sets of photoresist (PR) gratings were used for scatterometry measurements. The first, fabricated by Sony, was a 700-nm period (nominally 350-nm linewidth) photoresist grating on a 31.7-nm thick SiO_2 film on a silicon substrate that has been extensively characterized in prior work [4]. The other grating sample, supplied by Clariant AZ, Inc., was a 160-nm period (nominally 80-nm linewidth) photoresist grating on a bottom antireflective coating (BARC) layer.

3.1.2 Ellipsometer

All ellipsometry measurements were made using a SOPRA GESP-5 rotating polarizer ellipsometer with an ultraviolet-optimized prism/grating scanning monochrometer. The measurements were made in tracking-analyzer mode and the data reported in (α, β)-format. Data points were acquired every 5 nm over the 225 nm to 820 nm wavelength range.

3.1.3 Cell

Immersion measurements were performed using a cell designed for 75° angle of incidence. The cell was machined from aluminum with 3 mm thick fused-silica windows mounted so that the incident and specularly-reflected beams entered and exited nominally at normal incidence. The windows were cemented in place with silicone rubber.

Measurements were taken for a variety of uniform thin-film and grating structures and in the immersion cell without fluid to verify that the windows have no significant

effect on the collected data. The angle of incidence for all measurements taken in the cell was determined to be 75.06° by taking measurements on a bare silicon wafer over the 500 nm to 820 nm wavelength range and fitting to the native oxide thickness and the angle of incidence. All immersion measurements in this cell were performed with the fluid stagnant, and no active temperature or ambient gas controls were used.

3.1.4 Optical properties of water

We measured the refractive index of the water by measuring a thick (~ 2 μm) SiO_2 film on a silicon wafer both dry and wet. We simultaneously fit the thickness of the oxide and the refractive index of the water. The refractive index was modeled using the 4-parameter dispersion formula of Tilton and Taylor [40]:

$$n_t^2(\lambda) = a_t^2 - k_t \lambda^2 + \frac{m_t}{\lambda^2 - l_t^2} \tag{3.1}$$

where the refractive index n and the four parameters $a, k, l,$ and m have all been labeled with the subscript t to indicate that these quantities vary with temperature. We also investigated allowing all 4 of the Tilton–Taylor parameters to freely vary during regression.

To account for possible effects of atmospheric gas absorption, we used a Bruggemann effective-medium approximation (BEMA) [41, 42] mixture of Tilton–Taylor water at 23°C and voids. The BEMA uses the model of a spherical inclusions of dielectric function ϵ_a and radius r_a embedded in a medium of dielectric function ϵ_b. In the Bruggeman effective medium approximation, neither phase a nor b are given preference, but are considered as being embedded in the effective medium itself. This is equivalent to choosing $\epsilon_h = \epsilon$ in the general effective medium expression [42],

$$\frac{\epsilon - \epsilon_h}{\epsilon + 2\epsilon_h} = f_a \frac{\epsilon_a - \epsilon_h}{\epsilon_a + 2\epsilon_h} + f_b \frac{\epsilon_b - \epsilon_h}{\epsilon_b + 2\epsilon_h}, \tag{3.2}$$

where ϵ and ϵ_h are the dielectric functions of the effective medium and the host medium, respectively, and f_a and f_b are the volume fractions occupied by the phases a and b, respectively. The result is the Bruggeman effective-medium expression (also known as the Bruggeman effective-medium approximation)

$$0 = f_a \frac{\epsilon_a - \epsilon}{\epsilon_a + 2\epsilon} + f_b \frac{\epsilon_b - \epsilon}{\epsilon_b + 2\epsilon}. \quad (3.3)$$

The result of one of the refractive-index fits for an SiO_2 film on a silicon wafer is shown in figure 3.1. The unbiased estimator of error σ for all these fits was less than 0.03. All three parameterizations yielded nearly identical results for our water. In particular, the BEMA fit with 0.46% voids perfectly overlays the Tilton–Taylor 37.4°C fit. Since it was not physically possible for our laboratory and the immersion cell to be this hot, we rule out temperature variation as the major cause of our water index variations. For the immersion fits for gratings, we used the BEMA model for all results presented in this chapter.

We also investigated varying all four Tilton–Taylor parameters in the grating cases, but this led to model over-parameterization and possibly nonphysical results for the water index. The void fractions extracted in our fits were below those suggested by O_2 and N_2 solubilities in H_2O [43]. Changes in the water refractive index due to contamination cannot be ruled out, but this seems unlikely based on the results of studies of aqueous ion solutions [44]. Further, we see apparent reductions in the water refractive index, whereas ionic contamination would tend to raise it. For example, the refractive index of seawater can be described by the empirical dispersion formula of Quan and Fry [45],

$$n(S, T, \lambda) = n_0 + (n_1 + n_2 T + n_3 T^2)S + n_4 T^2 + \frac{n_5 + n_6 S + n_7 T}{\lambda} + \frac{n_8}{\lambda^2} + \frac{n_9}{\lambda^3}, \quad (3.4)$$

where S is the salinity in parts per thousand (per mil, or ‰), T is the temperature in

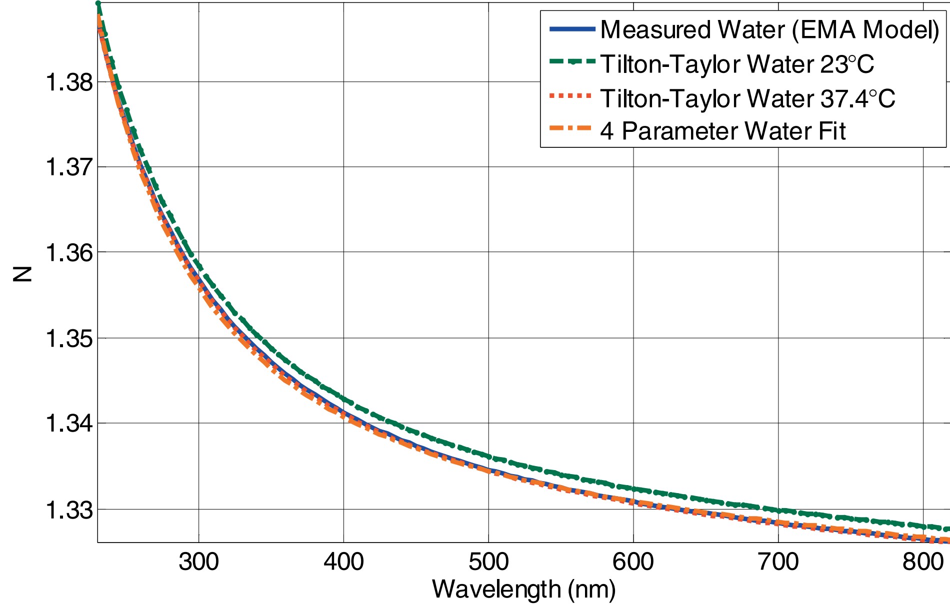

Figure 3.1 Extracted effective-medium approximation (EMA) refractive index for water (solid blue curve) and Tilton–Taylor reference data at 23°C (dashed green curve). Observe that the curves for the EMA model, the Tilton–Taylor model for $T = 37°$C, and freely-varying Tilton–Taylor model overlap, but the Tilton–Taylor model for $T = 23°$C does not.

Celsius, and λ is the wavelength in nanometers. The coefficients have the following values:

$$
\begin{aligned}
n_0 &= 1.314\,05 \\
n_1 &= 1.779 \times 10^{-4} \\
n_2 &= -1.05 \times 10^{-6} \\
n_3 &= 1.6 \times 10^{-8} \\
n_4 &= -2.02 \times 10^{-6} \\
n_5 &= 15.868 \\
n_6 &= 0.011\,55 \\
n_7 &= -0.004\,23 \\
n_8 &= -4382 \\
n_9 &= 1.1455 \times 10^{6}
\end{aligned}
$$

The dispersion curves for the refractive index of Quan-Fry seawater at 10‰ and 5‰

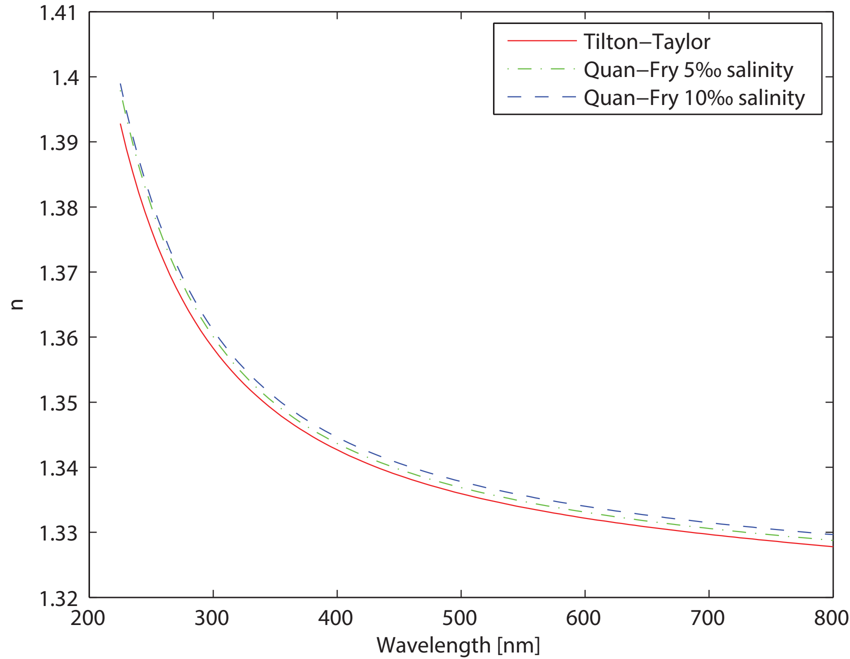

Figure 3.2 Refractive index of Quan-Fry seawater at 10‰(dashed blue curve) and 5‰(dash-dot green curve) salinity compared to Tilton-Taylor water (solid red curve) at 25 °C.

salinity and 25 °C are plotted alongside the dispersion curve for the refractive index of Tilton-Taylor water at 25 °C in figure 3.2. As expected, these curves show that increasing salinity raises the index of refraction of water, which is the opposite of the effect we observe in our refractive index fits.

3.2 Simulation of 100-nm period gratings

To motivate the use of immersion to improve the feature resolution, we use the RCWA code to simulate the ellipsometric spectra of 100-nm period silicon gratings. Figures 3.3 and 3.4 show these ellipsometric spectra for linewidths of 16 nm, 20 nm and 24 nm in air and deionized water, respectively. In air, there are no propagating backscattered modes, and in deionized water, only the first-order backscattered mode is accessible ($\lambda_0 < 267.4\,\mathrm{nm}$). Despite this, both the atmospheric and immersion spectra show

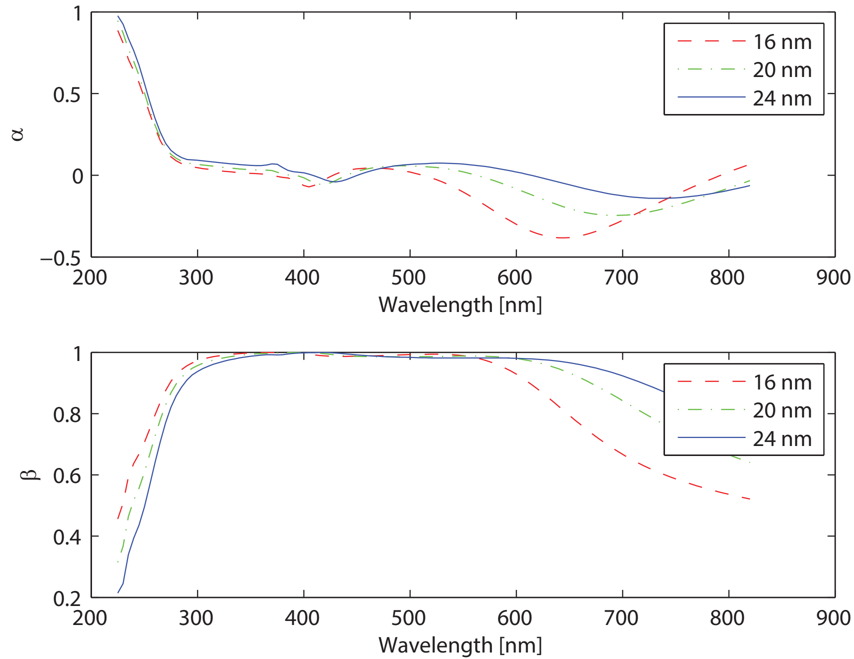

Figure 3.3 Simulated ellipsometric spectra for 100-nm period silicon gratings with linewidths of 16 nm, 20 nm and 24 nm in air.

sensitivities to linewidths well below the Rayleigh limit. In this atmospheric case, this sensitivity is essentially an effective-medium approximation of the grating ridges and the grating grooves. To illustrate this, we simulated the ellipsometric spectra for a 100-nm period silicon grating with a 24-nm average linewidth for sidewall angles of 90°, 87.5° and 85° in both air (figure 3.5) and deionized water (figure 3.6). We see that the atmospheric spectra have very little sensitivity to the sidewall angle over the entire spectrum, whereas the immersion spectra have some additional sensitivity near the cutoff of the first-order backscattered mode ($\lambda_0 \approx 267.4\,\text{nm}$). Photoresist gratings of comparable geometry would be even less sensitive to sidewall angle because photoresists have smaller dielectric constants than silicon.

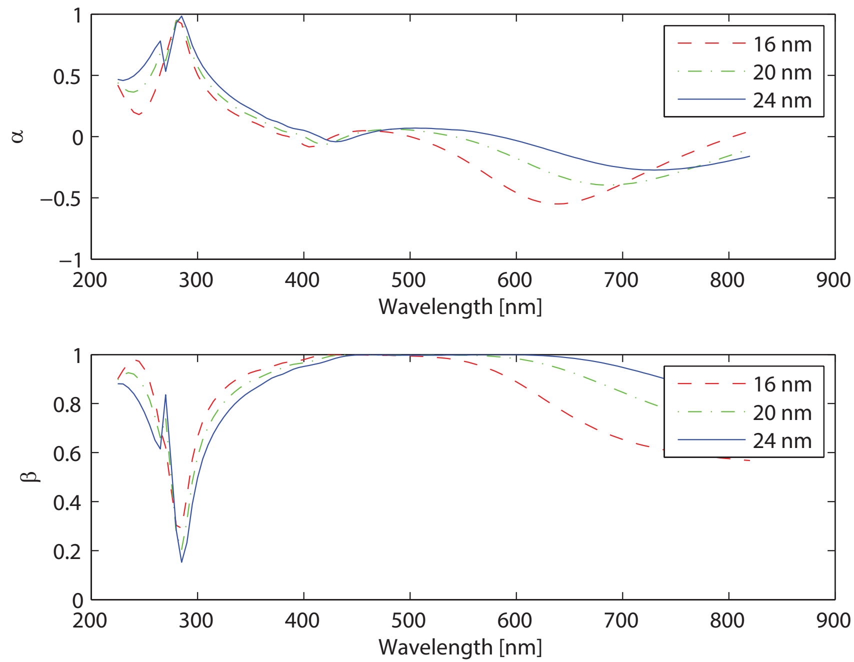

Figure 3.4 Simulated ellipsometric spectra for 100-nm period silicon gratings with linewidths of 16 nm, 20 nm and 24 nm in deionized water.

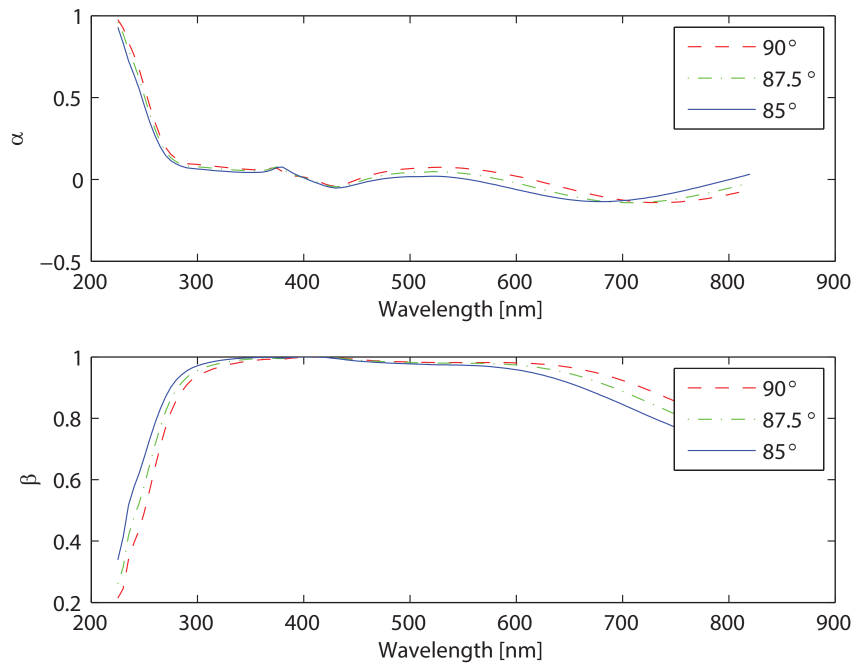

Figure 3.5 Simulated ellipsometric spectra for 100-nm period, 24-nm average linewidth silicon gratings with sidewall angles of 90°, 87.5° and 85° in air.

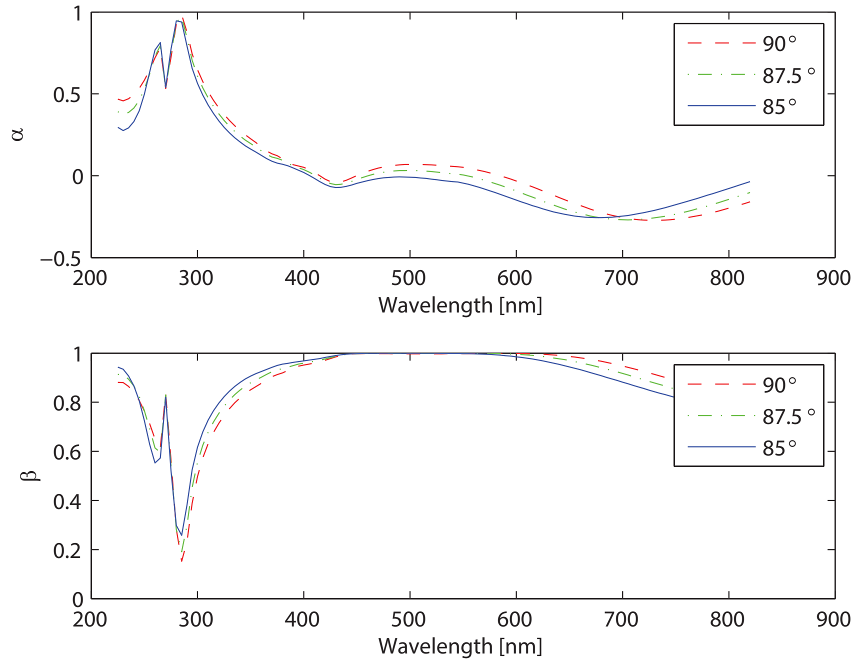

Figure 3.6 Simulated ellipsometric spectra for 100-nm period, 24-nm average linewidth silicon gratings with sidewall angles of 90°, 87.5° and 85° in deionized water.

3.3 Measurements on the 700-nm period gratings

Our initial experiments consisted of measurements on the 700-nm period gratings. The first set of measurements were made in air. The line topography was extracted using a computer program implemented in MATLAB which used Levenberg-Marquardt regression to drive a RCWA-based forward scattering simulation of a parameterized grating model. This program was originally implemented for previous work on scatterometry in our laboratory [46], and subsequently extended for simulation studies of immersion scatterometry [38]. The grating model we used was a stack of trapezoids of equal height. Initially, a single trapezoid was fit to the data. The parameters of the best fit was used to seed a 2-trapezoid fit, whose best-fit parameters were used to seed a 4-trapezoid fit, whose best-fit parameters were used to seed an 8-trapezoid fit. The single-trapezoid and 8-trapezoid fits are shown in figures 3.7 and 3.8, respectively, and the parameter fits and 95.4% confidence limits for the 8-trapezoid model are shown in

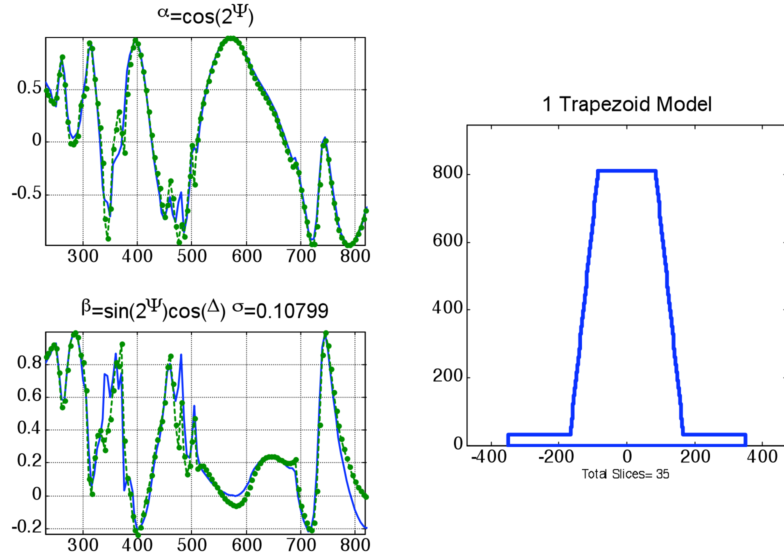

Figure 3.7 Measured (blue solid curves) and best-fit (green dashed curves) spectroscopic ellipsometric (SE) data for a single-trapezoid model of the 700-nm photoresist (PR) grating measured in air.

figure 3.9. Figure 3.10 shows this fitted profile overlaid on a cross-sectional scanning electron micrograph (SEM) of this grating, and there is excellent agreement between the fitted profile and the SEM image. For these fits, 11 spatial orders were used in the RCWA simulation (based on convergence tests) and a slicing algorithm that insured no more than a 2-nm width change between each slice (resulting in 159 slices for the 8-trapezoid fit).

The sharp structure in this data arises from scattering of energy into non-specular reflected and transmitted modes. For the 700-nm gratings measured in air, simulations from the fitted structures show significant scattering into the $m = 1$ to 6 backscattered modes (both reflected and transmitted). Forward scattering is insignificant for these structures over the wavelength measured. Strong transmitted-mode scattering tends to occur just before the allowed onset of the same-order reflected mode (as illustrated in figure 3.11). This trend occurred for all photoresist grating structures studied. These regions of strong diffraction are very sensitive to changes in the grating lineshape.

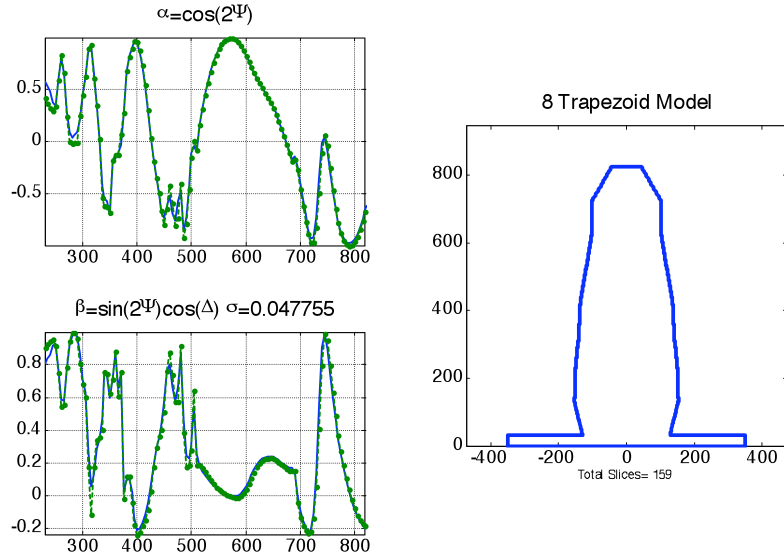

Figure 3.8 Measured and best-fit SE data for an 8-trapezoid model of the 700-nm PR grating measured in air.

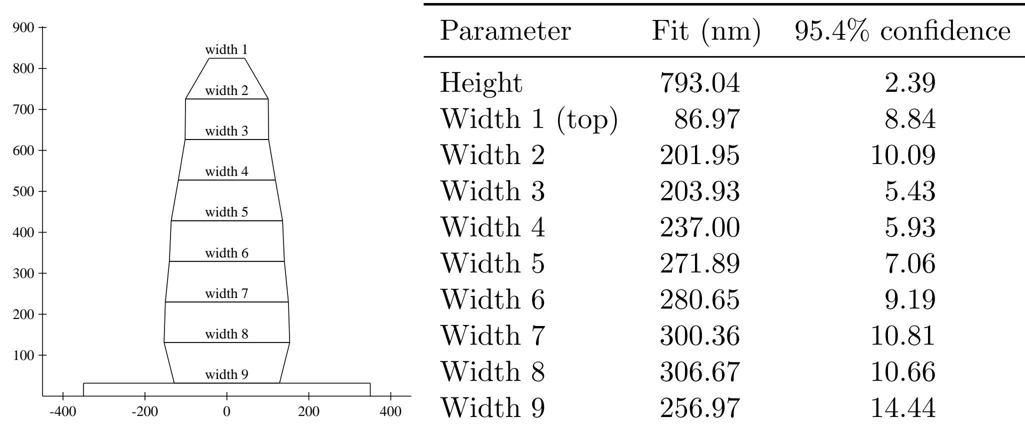

Parameter	Fit (nm)	95.4% confidence
Height	793.04	2.39
Width 1 (top)	86.97	8.84
Width 2	201.95	10.09
Width 3	203.93	5.43
Width 4	237.00	5.93
Width 5	271.89	7.06
Width 6	280.65	9.19
Width 7	300.36	10.81
Width 8	306.67	10.66
Width 9	256.97	14.44

Figure 3.9 Fit results and 95.4% confidence limits for an 8-trapezoid grating model to dry ellipsometric measurements of the 700-nm grating.

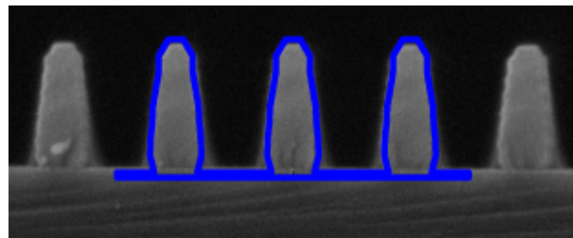

Figure 3.10 Comparison of best 8-trapezoid fit (blue outline) of the 700-nm grating measured in air with cross-sectional scanning electron micrograph.

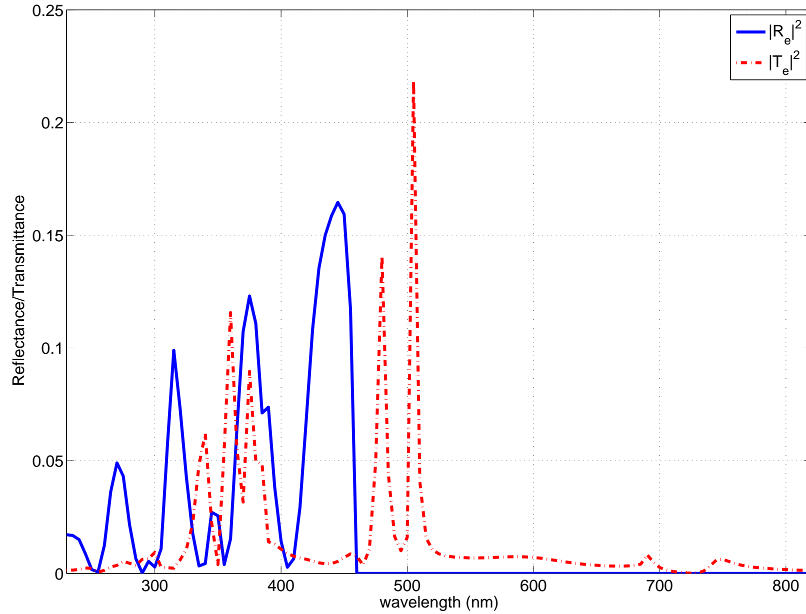

Figure 3.11 Simulated $m = 3$ backscattered reflected (solid blue) and transmitted (dashed red) energy for best-fit 8-trapezoid model of the 700-nm grating measured in air.

We applied the same procedure to measure the grating in water. The final 8-trapezoid immersion fit is shown in figure 3.12 and superimposed on the final 8-trapezoid dry fit in figure 3.13. Since the dry data topography fit agrees well with SEM observations, we must conclude that there is a systematic error in either the immersion measurement or the ambient refractive index extraction. Our simulations indicate that an angle of incidence error will not explain this variation. Also, measurements of different thicknesses of SiO_2 on Si show very good quality fits in both dry and immersion measurements with the same oxide thickness. Variations in the photoresist density were investigated (assuming an effective media mixing of voids with the reference PR index data), but this too failed to explain our observed immersion measurements. Also, including trapped air (bubbles) in the grating lines also failed to prove valid.

To best fit our current experimental data, we simultaneously fit a single topography

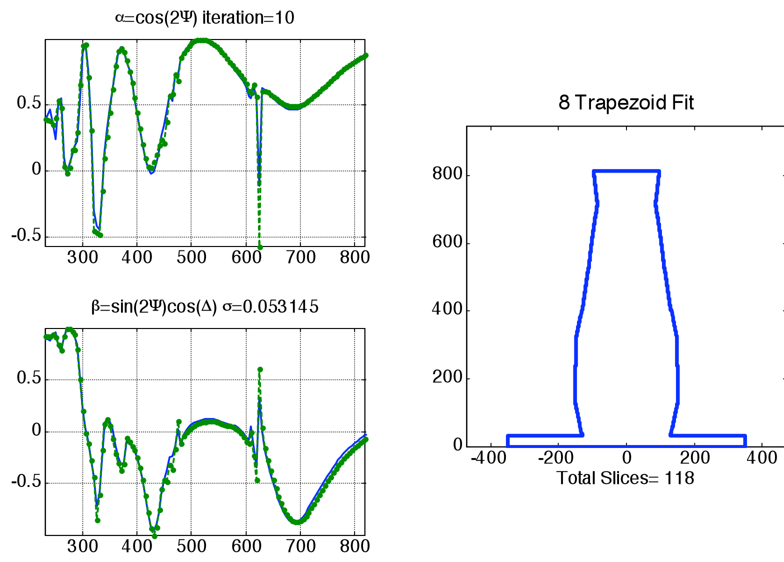

Figure 3.12 Measured and best-fit SE data for an 8-trapezoid model of the 700-nm PR grating measured in water.

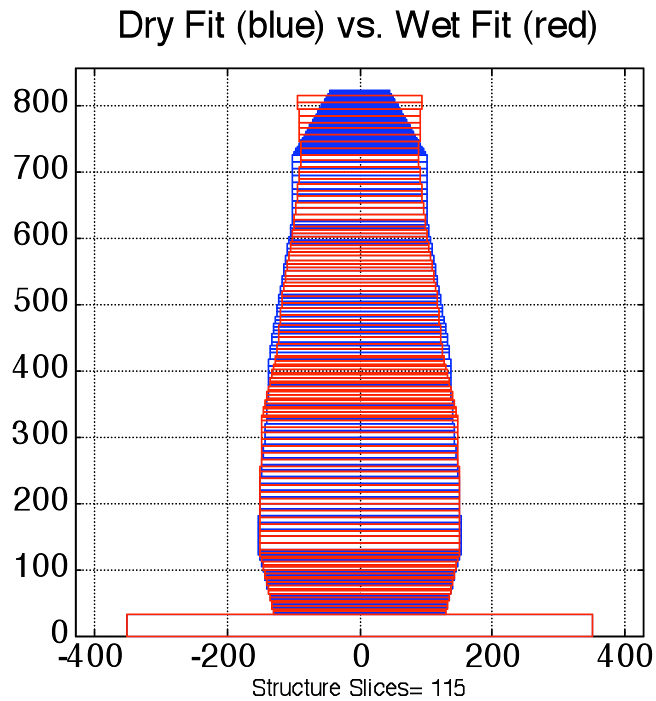

Figure 3.13 Comparison of the best fit from SE data for an 8-trapezoid model of the 700-nm PR grating measured in water (red) and air (blue).

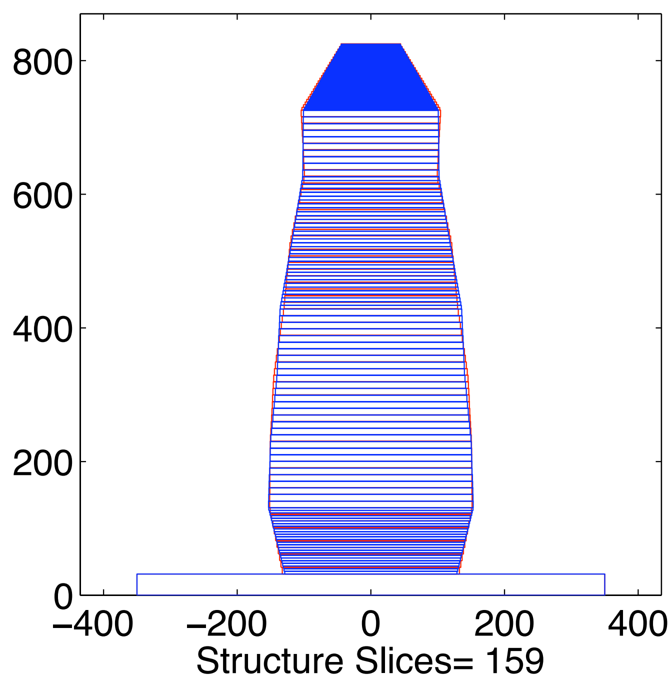

Figure 3.14 Comparison of the dry-only fit (blue) and dual dry/BEMA fit (red) for the 700 nm grating.

to both the dry and immersion data and also varied the water index using the BEMA model. The topography extracted from this fit very closely overlay that of the dry-only fit as shown in figure 3.14. The extracted void fraction of the water was $0.537 \pm 0.087\%$. The values of the extracted topography parameters are very close to those shown in figure 3.9. The confidence limits are slightly higher. The additional information in the immersion measurement did not offset the additional uncertainty introduced by adding an additional model parameter.

3.4 Measurements on the 160-nm period gratings

For the 160 nm photoresist gratings, only the first-order backscattered mode is accessible ($\lambda < 315$ nm dry, 430 nm in H_2O). This lack of allowed scattered modes reduces the sensitivity to the lineshape. The measured data could be fit well using a single

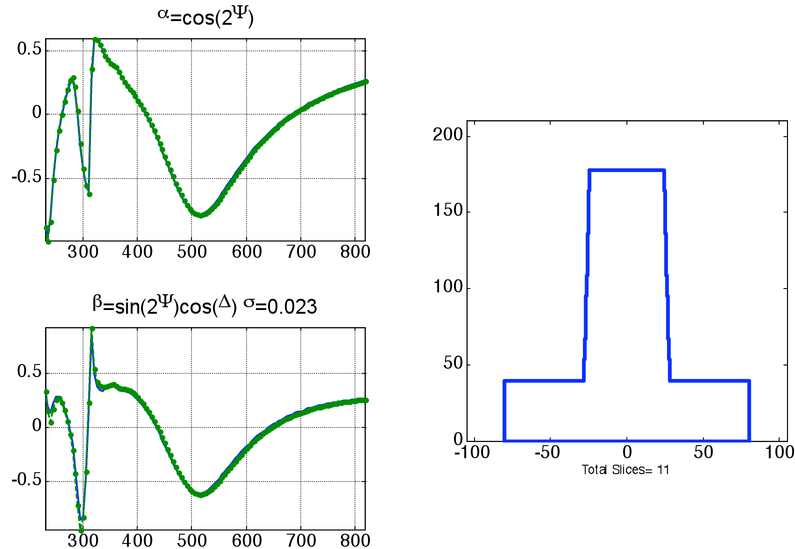

Figure 3.15 Measured and best-fit SE data for a single-trapezoid model of the 160-nm PR grating measured in air.

trapezoid model as shown in figure 3.15 and with the parameter fits and confidence limits shown in figure 3.17. The dual-ambient fit is very similar to a dry-only fit for the single trapezoid shape model, as is shown in figure 3.16. Previous computational studies showed that additional shape information should be obtainable from the extra information in immersion data [38].

The problems posed by the apparent variation of water refractive indices prevented us from experimentally demonstrating improved confidence limits in the extracted topography parameters. However, in our attempts to gain more shape information from the 160-nm gratings, we did find a strong indication that the extra information in the immersion data may be helpful. We fit the data using increasing numbers of equal-height trapezoids. As the number of trapezoids in the model increased, we found that the dry fits would deviate into physically unreasonable structures while the dual mode (dry/wet-BEMA) fits yielded physically reasonable resist shapes. An illustration of this is found in figures 3.18 and 3.19 for a 16-trapezoid fit. Clearly, this is an over-parameterization and the results may be nonphysical in both cases; however, it is

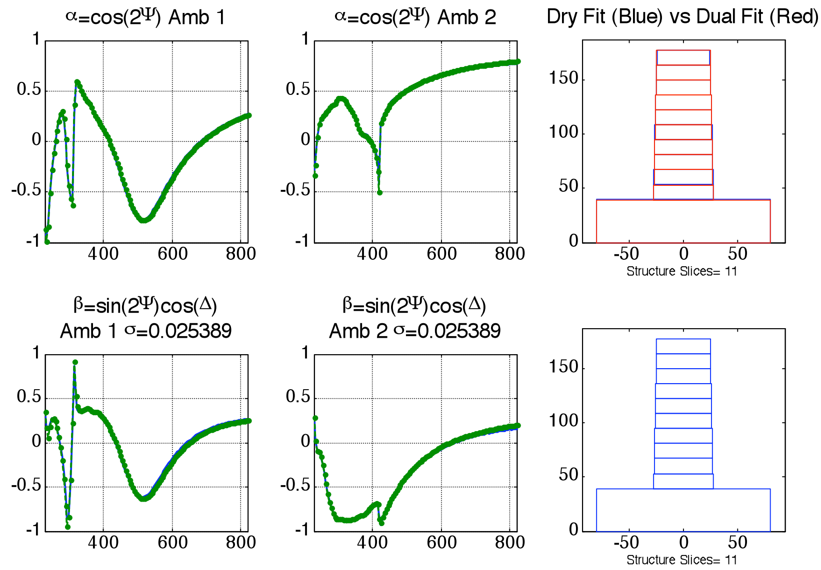

Figure 3.16 Measured and best dual-ambient fit SE data for a single-trapezoid model of the 160-nm PR grating measured in water.

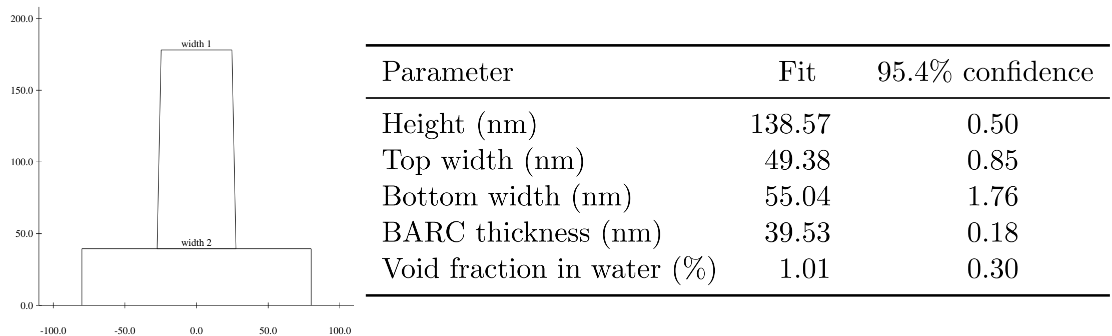

Parameter	Fit	95.4% confidence
Height (nm)	138.57	0.50
Top width (nm)	49.38	0.85
Bottom width (nm)	55.04	1.76
BARC thickness (nm)	39.53	0.18
Void fraction in water (%)	1.01	0.30

Figure 3.17 Fit results and confidence limits for a single-trapezoid grating model to dual-mode (dry and wet) ellipsometric measurements of the 160-nm grating. $\sigma = 2.5 \times 10^{-2}$ for this fit.

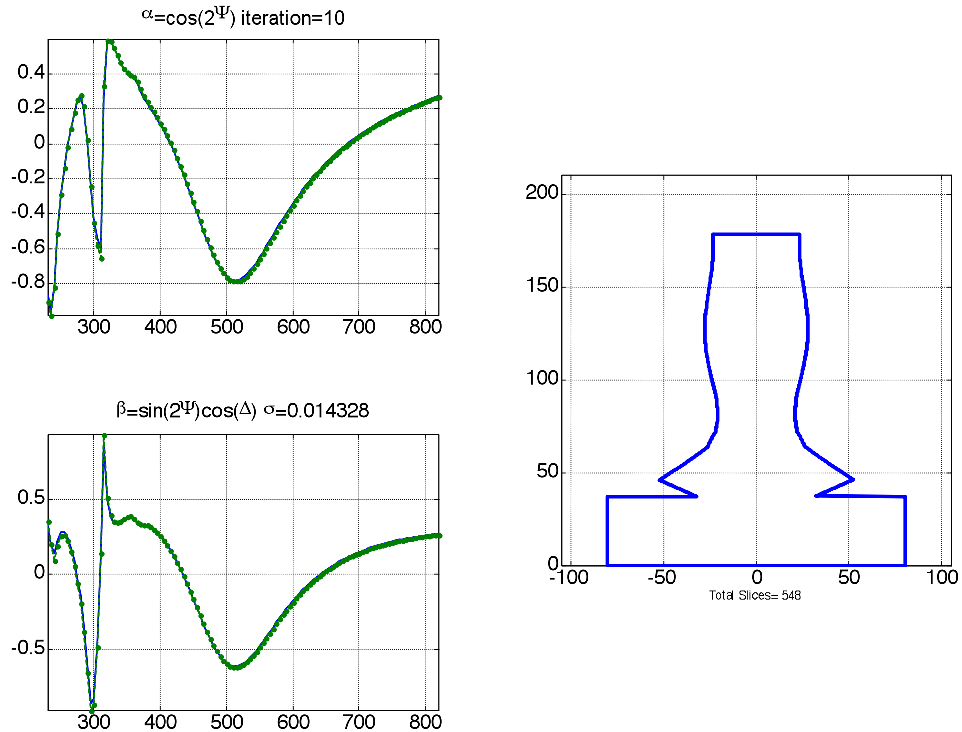

Figure 3.18 Measured and best-fit SE data for a 16-trapezoid model of the 160-nm PR grating measured in air.

interesting to note that the dry-only fit is very improbable for a photoresist structure, whereas the dual mode fit yields the commonly encountered case of a basically vertical line with a "footer." Due to the very small size of these features, we have not yet been able to obtain cross-sectional electron micrographs to further investigate this result.

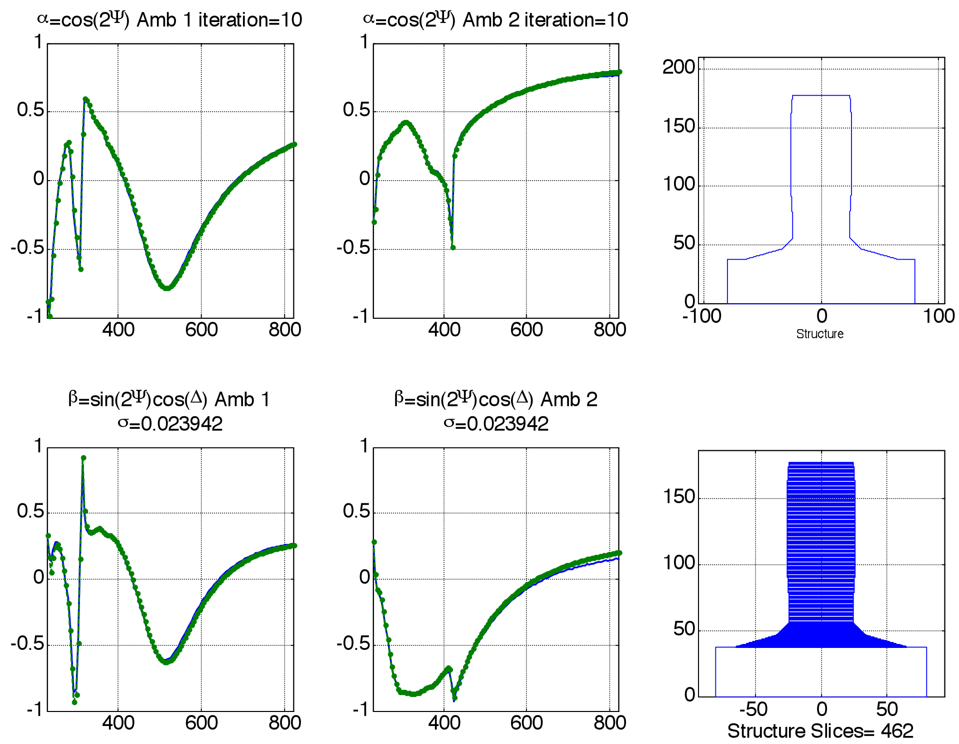

Figure 3.19 Measured and best dual-ambient fit SE data for a 16-trapezoid model of the 160-nm PR grating.

Chapter 4

Investigation of systematic errors in immersion ellipsometry

The preliminary immersion scatterometry results in chapter 3 suggest that the resolution of topography extraction is limited by one or more sources of systematic error in immersion ellipsometry. There is a surprising absence in the ellipsometry literature of investigation of error sources in immersion ellipsometry. Based on our preliminary experimental results, we have identified several potential sources of systematic error: error in the angle of incidence in the immersion case, error in our estimate of the immersion refractive index due to ambient conditions, and errors due to stress-induced birefringence in the immersion case.

4.1 Errors in angle of incidence

One of the potential sources of systematic error in immersion ellipsometry are deviations in the angle of incidence in the immersion case relative to the atmospheric case. To illustrate the origin of these deviations, we consider the deviation of an oblique ray incident upon an ideal plane-parallel window in air and in liquid immersion. The geometry of this scenario is illustrated in figure 4.1. In air, a ray incident at angle θ_1 emerges at angle θ_1. In the case where the incident medium has refractive index n_1

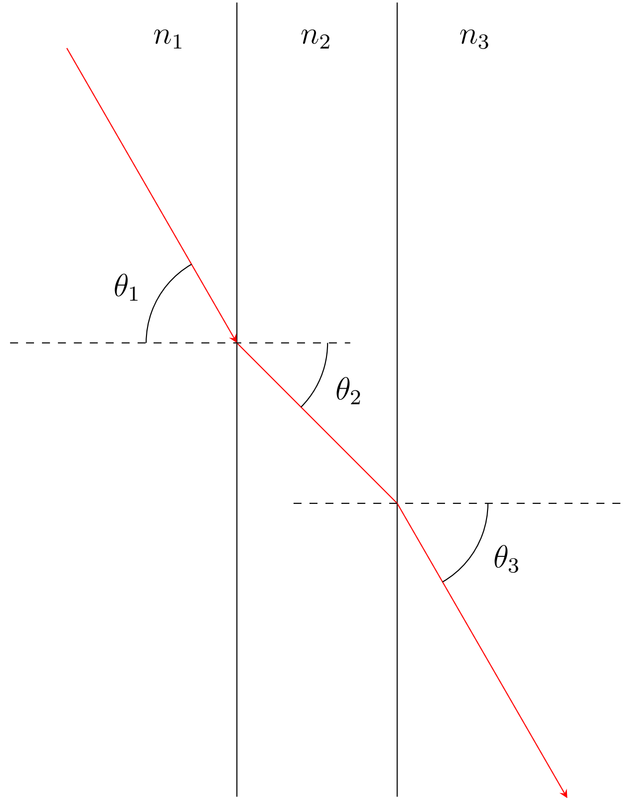

Figure 4.1 Deviation of an oblique ray incident upon an ideal plane-parallel window.

and the exit medium has refractive index n_2, the exit angle θ_2 is given by

$$\theta_2 = \arcsin\left(\frac{n_1 \sin\theta_1}{n_2}\right).$$

When the ambient refractive index is the same on both sides of the window (i.e. $n_1 = n_2$), then the ray exits the window at the same angle as it impinges (i.e. $\theta_1 = \theta_2$). However, when the ambient refractive index is different on either side of the window ($n_1 \neq n_2$) and the ray does not impinge upon the window at exactly normal incidence (i.e. $\theta_1 \neq 0°$), then the ray exits the window at a different angle than it entered. This also results in the polarizer beam impinging upon the sample at a different angle in the immersion case than in the atmospheric case.

4.1.1 Simulation

To motivate our experimental work, we simulated the change in the ellipsometric spectrum for the immersion measurements of a variety of unpatterned thin-film samples when different pairs of measurement parameters (e.g. angle of incidence, ambient refractive index parameters, etc.) are varied. The error surface for immersion ellipsometry of a nominally bare silicon wafer (2 nm SiO_2 on Si) in deionized water for errors in the angle of incidence and ambient temperature is shown in figure 4.2. We use Tilton and Taylor's formula for the refractive index of water that interpolates for both temperature and wavelength [40]:

$$
\begin{aligned}
n(t,\lambda) = &\sqrt{a_{20}^2 - k_{20}\lambda^2 + \frac{m_{20}}{\lambda^2 - l_{20}^2}} \\
&- \frac{\left\{\bar{B} - \frac{b(\Delta\lambda)^3}{\lambda - l}\right\}(\Delta t)^3}{(t+\bar{D})\times 10^7} \\
&- \frac{\left\{\bar{A} - a'\Delta\lambda\left(1 + \frac{a''}{\lambda - l}\right)\right\}(\Delta t)^2}{(t+\bar{D})\times 10^7} \\
&+ \frac{\left\{\bar{C} - c\Delta\lambda\left(1 + \frac{c'}{\lambda - l}\right)\right\}\Delta t}{(t+\bar{D})\times 10^7}
\end{aligned}
$$

where

$$
\begin{aligned}
a_{20}^2 &= 1.761\,631\,6 \\
k_{20} &= 0.011\,988\,2 \\
l_{20} &= 0.122\,114\,5 \\
m &= 0.006\,442\,77 \\
\bar{A} &= 2352.12 \\
\bar{B} &= 6.3649 \\
\bar{C} &= 76\,087.9 \\
\bar{D} &= 65.7081
\end{aligned}
$$

$$
\begin{aligned}
a' &= 143.63 \\
a'' &= 0.4436 \\
b &= 10.562 \\
c &= 12\,504 \\
c' &= 0.084\,30
\end{aligned}
$$

From the contours of the error surface, we see that the measurement of nominally bare silicon is very sensitive to angle of incidence and relatively insensitive to ambient temperature (and its effects on the ambient refractive index). A relatively small (0.1°) change in the angle of incidence results in a mean-squared error in the ellipsometric signal of the same magnitude as a relatively large ($> 5\,°C$) change in the ambient temperature. Thus we can use immersion ellipsometry of a nominally bare silicon wafer to bound the uncertainty in actual angle of incidence in the immersion case.

4.1.2 Materials and methods

Samples

To estimate the actual angle of incidence in the immersion case, we perform liquid immersion measurements on a nominally bare silicon wafer. Simulation of the mean square error of the ellipsometric signal as a function of the error in angle of incidence and ambient refractive index shows that, in the case of bare silicon, the mean-squared error is sensitive to angle of incidence and not to refractive index.

The samples used were p-doped silicon wafers. The native oxide thickness was determined to be approximately 2 nm from ellipsometric measurements in air using SOPRA Winelli software.

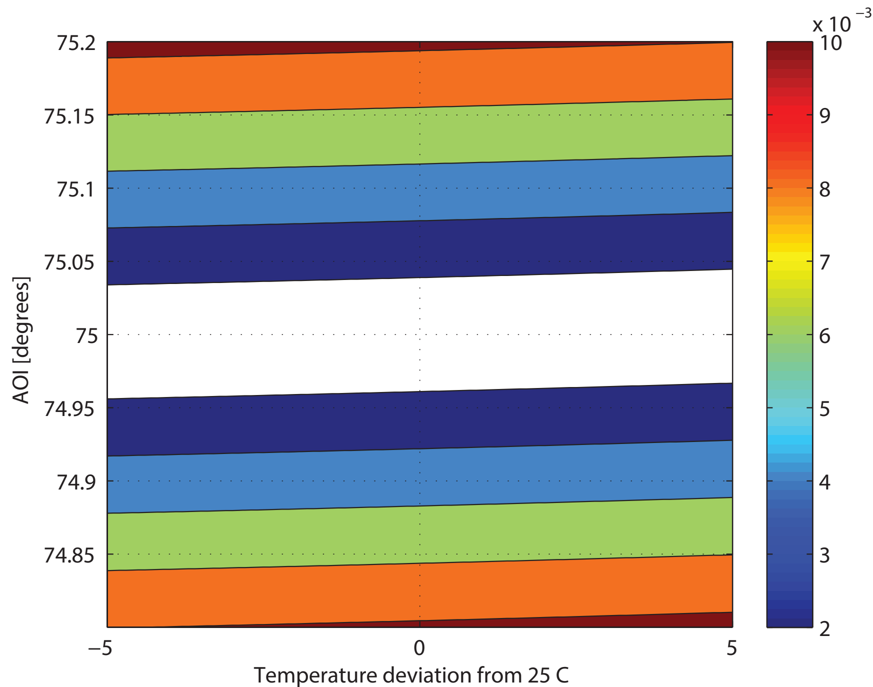

Figure 4.2 Error surface for immersion ellipsometry of a nominally bare silicon wafer (2 nm SiO_2 on Si) in deionized water for errors in the angle of incidence (AOI) and ambient temperature. The contours of the error surface show that immersion measurements of this sample are relatively sensitive to angle of incidence and relatively insensitive to ambient temperature, since a relatively small change in the angle of incidence results in a mean-squared error comparable to a relatively large change in the ambient temperature.

Alignment procedure

To ascertain the repeatability of the angular estimation procedure, we replaced the optical fiber to the monochromator with a fiber-coupled HeNe laser and used the following alignment procedure before each measurement:

1. Remove the immersion cell from the stage.
2. Set the goniometer to 90°.
3. Set the analyzer to 45°.
4. Set the goniometer to the desired angle of incidence.
5. Place the immersion cell on the stage. Adjust the azimuthal orientation of the cell to align both retroreflections as much as possible.
6. Repeat the following steps until the alignment is satisfactory:
   (a) Adjust the stage height to bring the HeNe beam into alignment.
   (b) Adjust the tip-tilt of the stage to bring the probe beam into alignment.

Data analysis

Initial measurements were taken at the design angle of incidence to obtain an initial estimate. The target angle was then perturbed until there was satisfactory agreement between the goniometer settings and the estimates. Ellipsometric data were collected from 300 nm to 800 nm at 5 nm intervals. The estimates were generated using SOPRA WinElli for the following structural model:

- An ambient medium of Tilton-Taylor water at 23 °C.
- An SiO_2 film of 2 nm nominal thickness on a crystalline silicon substrate.

The regression parameters were the angle of incidence and the thickness of the SiO_2 film. The initial estimates pointed to a target angle of incidence of 74.85°.

4.1.3 Results and discussion

Representative ellipsometric spectra for a "bare" silicon wafer in air and in deionized water are shown in Figures 4.3 and 4.4, respectively. In additional, measurements were taken in the cell before and after it was anodized. Initial Levenberg-Marquardt regression estimates of the angle of incidence from Sopra WinElli pointed to an actual angle of incidence in deionized water of 74.8° for the unanodized cell. WinElli's estimates for the actual angle of incidence and the thickness of the native oxide when the goniometer was set to 74.85° are tabulated in Table 4.1. The time evolution of these estimates are plotted in figures 4.5 and 4.6. It is clear that the estimates in both quantities is drifting over time, hence we decided to anodize the cell in case chemical contamination due to the corrosion of the aluminum cell was responsible for this drift.

After the cell was anodized and reassembled, we repeated these calibration measurements. Based on the initial Levenberg-Marquardt regression estimates of the angle of incidence from Sopra WinElli pointed to an actual angle of incidence in deionized water of 74.85° for the anodized cell. WinElli's estimates for the actual angle of incidence and the thickness of the native oxide when the goniometer was set to

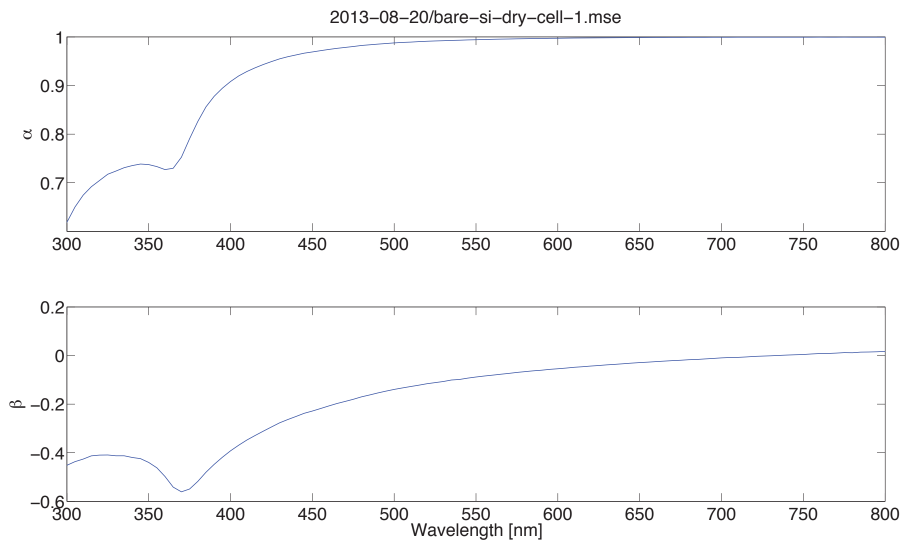

Figure 4.3 A representative ellipsometric spectrum from a "bare" silicon wafer in air in (α, β) format.

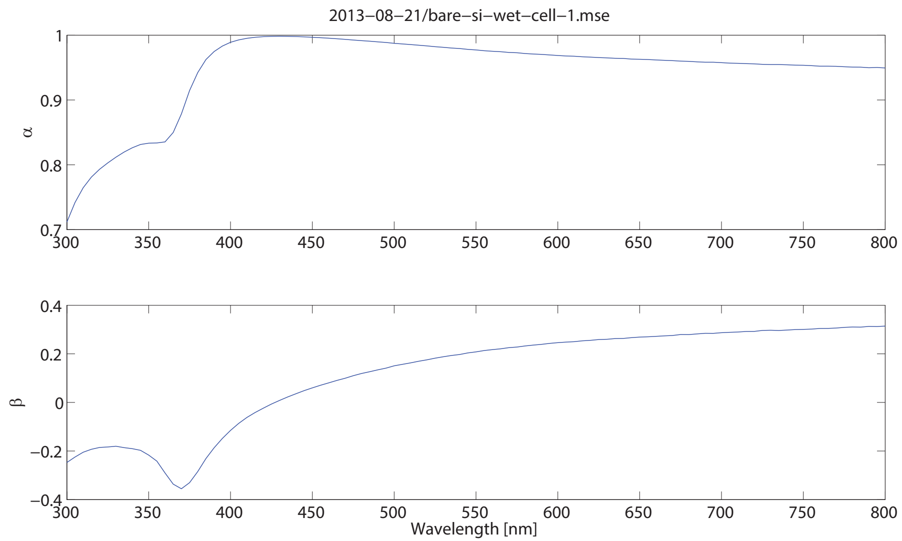

Figure 4.4 A representative ellipsometric spectrum from a "bare" silicon wafer in deionized water in (α, β) format.

Table 4.1 Angular repeatability of immersion ellipsometric measurements of a nominally bare silicon wafer in an unanodized aluminum cell.

Angle θ	σ_θ	SiO_2 thickness t [nm]	σ_t
74.797 180	0.000 100	1.415 214	0.179 018
74.748 793	0.000 106	2.841 189	0.186 097
74.763 854	0.000 114	2.321 740	0.200 218
74.751 652	0.000 112	3.116 431	0.214 318
74.759 372	0.000 090	2.623 408	0.157 480
74.648 450	0.000 111	3.859 357	0.191 702
74.698 102	0.000 142	3.583 165	0.248 172
74.664 070	0.000 078	4.443 099	0.134 375
74.677 718	0.000 112	4.554 183	0.197 924
74.597 925	0.000 071	4.410 603	0.123 032

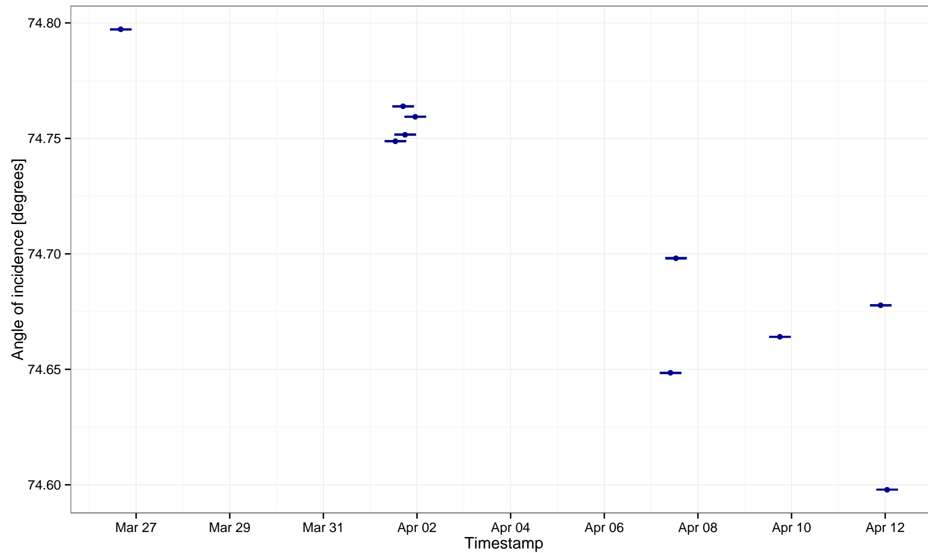

Figure 4.5 Estimated angle of incidence from ellipsometric measurements of a "bare" silicon wafer in deionized water, taken in an unanodized aluminum cell over the course of several weeks. The horizontal lines associated with each data point indicate the upper confidence limit and lower confidence limit of the 95.4% confidence interval for each individual measurement.

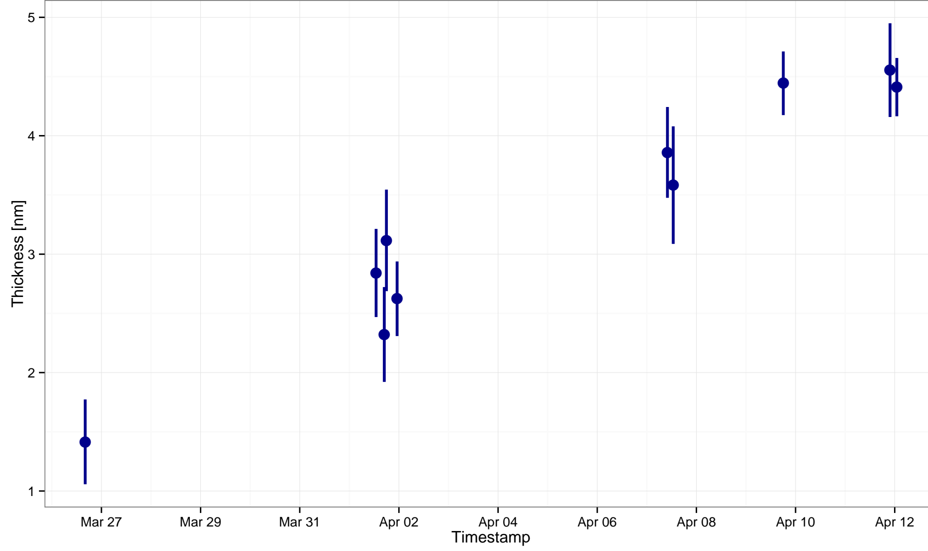

Figure 4.6 Estimated SiO_2 thickness from ellipsometric measurements of a "bare" silicon wafer in deionized water, taken in an unanodized aluminum cell over the course of several weeks. The vertical lines associated with each data point indicate the 95.4% confidence interval for each individual measurement.

Table 4.2 Angular repeatability of immersion ellipsometric measurements of a nominally bare silicon wafer in an anodized aluminum cell.

Angle θ	σ_θ	SiO_2 thickness t [nm]	σ_t
74.858 351	0.000 081	2.124 043	0.143 860
74.860 406	0.000 078	2.052 209	0.137 471
74.864 992	0.000 079	2.119 181	0.139 126
74.805 860	0.000 066	2.949 611	0.115 441
74.861 111	0.000 092	2.471 062	0.163 022
74.865 824	0.000 108	2.474 316	0.188 884
74.839 214	0.000 102	1.849 462	0.184 642
74.872 679	0.000 091	2.774 831	0.159 937
74.886 235	0.000 100	2.603 019	0.176 643

$$\bar{\theta} \pm \hat{\sigma}_\theta = 74.857\,185\,780° \pm 0.007\,641\,179°$$
$$\bar{t}_{\mathrm{SiO_2}} \pm \hat{\sigma}_t = 2.379\,748\,222\,\mathrm{nm} \pm 0.121\,890\,830\,\mathrm{nm}$$

74.85° are tabulated in Table 4.2. There is excellent agreement between the estimated angle of incidence and the goniometer set point, and a high degree of repeatability of these estimates.

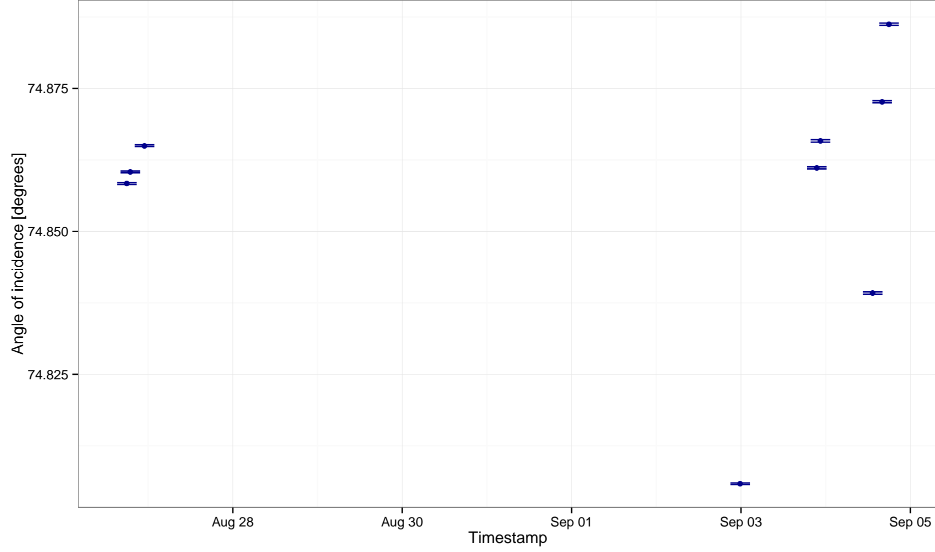

Figure 4.7 Estimated angle of incidence from ellipsometric measurements of a "bare" silicon wafer in deionized water, taken in an anodized aluminum cell over the course of a week. The horizontal lines associated with each data point indicate the upper confidence limit and lower confidence limit of the 95.4% confidence interval for each individual measurement.

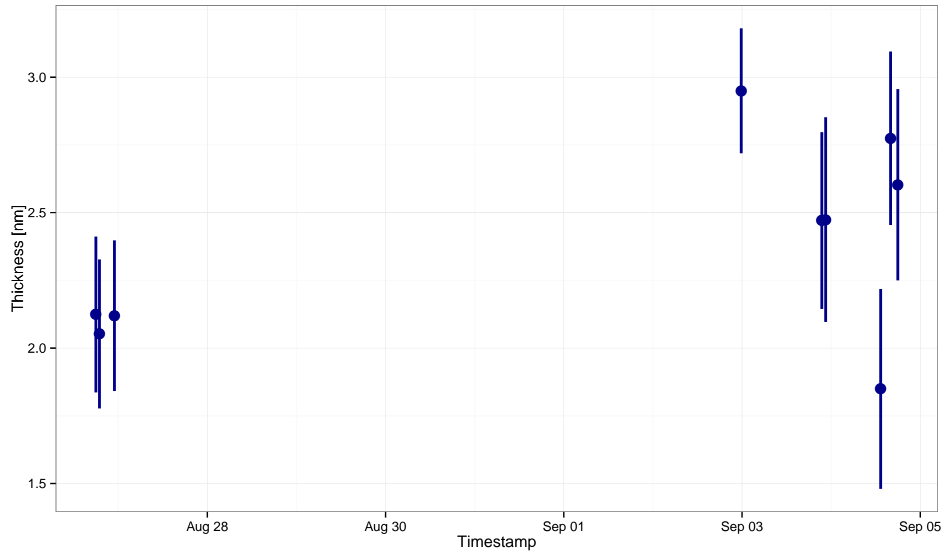

Figure 4.8 Estimated SiO_2 thickness from ellipsometric measurements of a "bare" silicon wafer in deionized water, taken in an anodized aluminum cell over the course of a week. The vertical lines associated with each data point indicate the 95.4% confidence interval for each individual measurement.

4.2 Errors in ambient refractive index

4.2.1 Simulation

As in the case of angle of incidence, we motivate our experimental work by simulating the change in the ellipsometric spectrum for the immersion measurements of a variety of unpatterned thin-film samples when different pairs of measurement parameters (e.g. angle of incidence, ambient refractive index parameters, etc.) are varied. The error surface for immersion ellipsometry of a thick (2 µm) SiO_2 film on Si in deionized water for errors in the angle of incidence and ambient temperature is shown in figure 4.9. From the contours of the error surface, we see that errors in angle of incidence and ambient temperature are highly correlated, so one cannot determine just from immersion ellipsometry of a thick SiO_2 film whether the observed systematic measurement error is due to errors in the angle of incidence or the ambient temperature. However, if we can bound the error in the angle of incidence (e.g. using measurements on nominally bare silicon), then we can also bound the error in the ambient refractive index.

4.2.2 Materials and methods

Samples

To estimate the actual angle of incidence in the immersion case, we performed liquid immersion measurements on a thick ($\approx$ 2 µm) SiO_2 film on a Si wafer. We used a SOPRA reference wafer with a nominal SiO_2 film thickness of 2.0037 µm. Repeated measurements of this wafer in air resulted in an estimated SiO_2 thickness of 2.0025 µm.

Measurements

We did two measurements to assess different potential causes of ambient refractive index effects. One was to monitor and log the temperature of the immersion cell

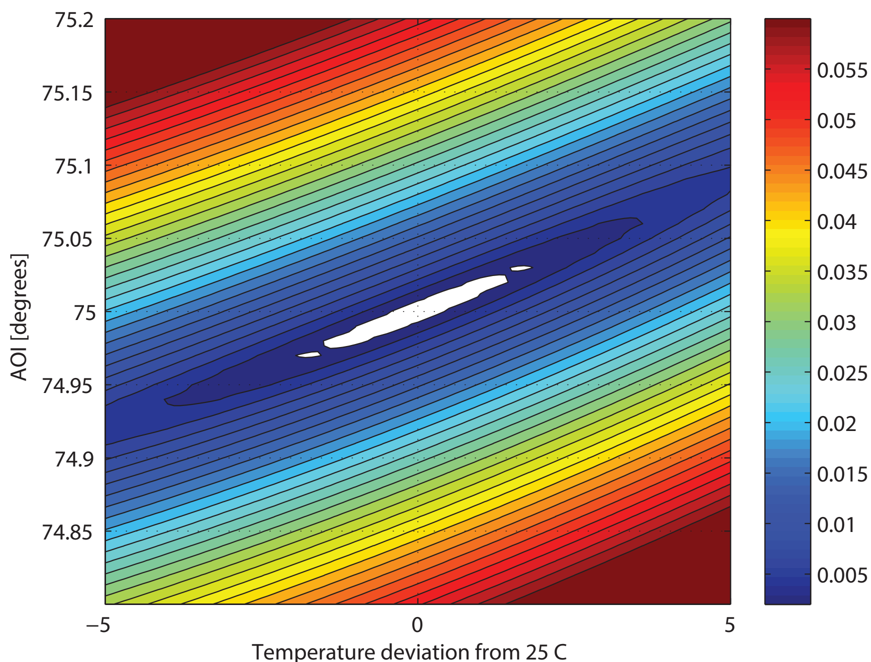

Figure 4.9 Error surface for immersion ellipsometry of a thick (2 µm) SiO_2 film on Si in deionized water for errors in the angle of incidence and ambient temperature.

during the ellipsometric measurement. The second was to compare regression results for a refractive index parameter for measurements performed at atmospheric pressure and for measurements after sonic degassing at rough vacuum (∼150 torr). The cell temperature was monitored using a Maxim DS18B20 one-wire digital thermometer. The sensor values were read by an Arduino Uno microcontroller board and transmitted by USB (Universal Serial Bus) to a laptop computer. The computer was running a Processing script that received the data on this USB port and logged timestamps and the observed temperature values to a comma-separated value (CSV) file. The same Arduino microcontroller board was also used to drive a CUI CEM-1203(42) magnetic buzzer for sonic degassing. The buzzer was driven at 2 kHz, and bubbles were observed nucleating and detaching when the buzzer was active and the vacuum pump was running.

Data analysis

WinElli is not capable of incorporating arbitrary optical models such as the Tilton-Taylor formula for water, so we adapted the MATLAB RCWA code to facilitate inclusion of these models in our regression analyses. We ran Levenberg-Marquardt regression for the angle of incidence and the ambient temperature for the following structural model:

- An ambient medium of Tilton-Taylor water at 23 °C.
- An SiO_2 film of 2.0025 µm nominal thickness (determined by ellipsometric measurements of the sample in air).
- A crystalline silicon substrate.

4.2.3 Results and discussion

Representative ellipsometric spectra for the SOPRA reference wafer with 2.0037 µm SiO_2 on Si in air and water are shown in figure 4.10 and 4.11. Furthermore, we collected data for in both undegassed and degassed deionized water, and logged the temperature for the entire duration of each measurement under either condition. The temperature was in the range 23 °C ± 1 °C during all measurements. The estimated parameters for the undegassed and degassed measurements are tabulated in table 4.3. It is apparent that the $\sim$ 38 °C estimates for the ambient temperature T from both the undegassed and degassed measurements are many standard deviations away from the logged temperature of 23 °C. Thus it would appear that dissolved atmospheric gases are not responsible for the systematic errors observed in the immersion measurement, which is consistent with remarks by Tilton and Taylor [40] and Harvey and co-workers [47] that the effect of dissolved air on the refractive index of water should be $|\Delta n| < 1 \times 10^{-5}$.

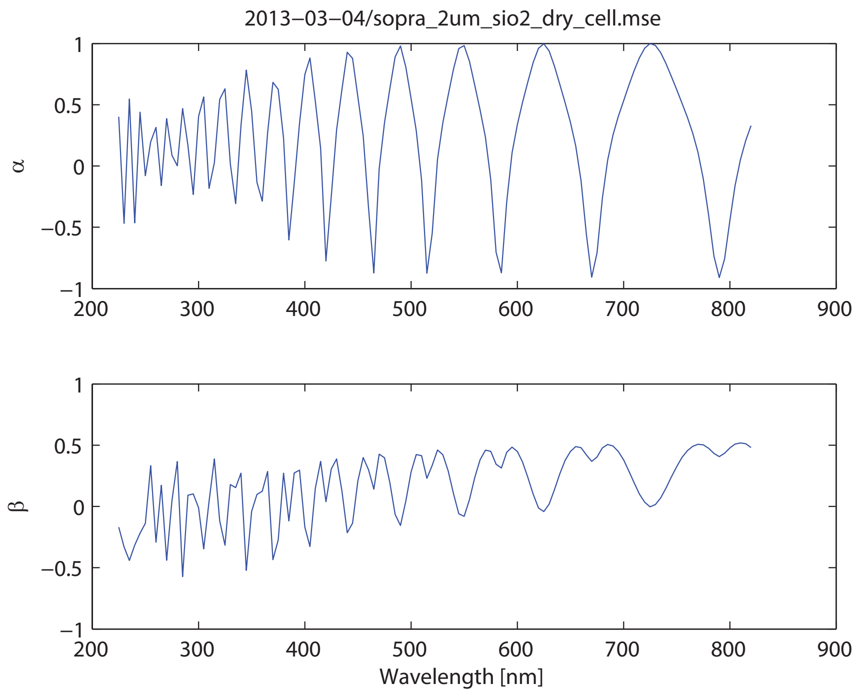

Figure 4.10 Representative ellipsometric spectrum for SOPRA reference wafer with 2.0037 µm SiO_2 on Si in air.

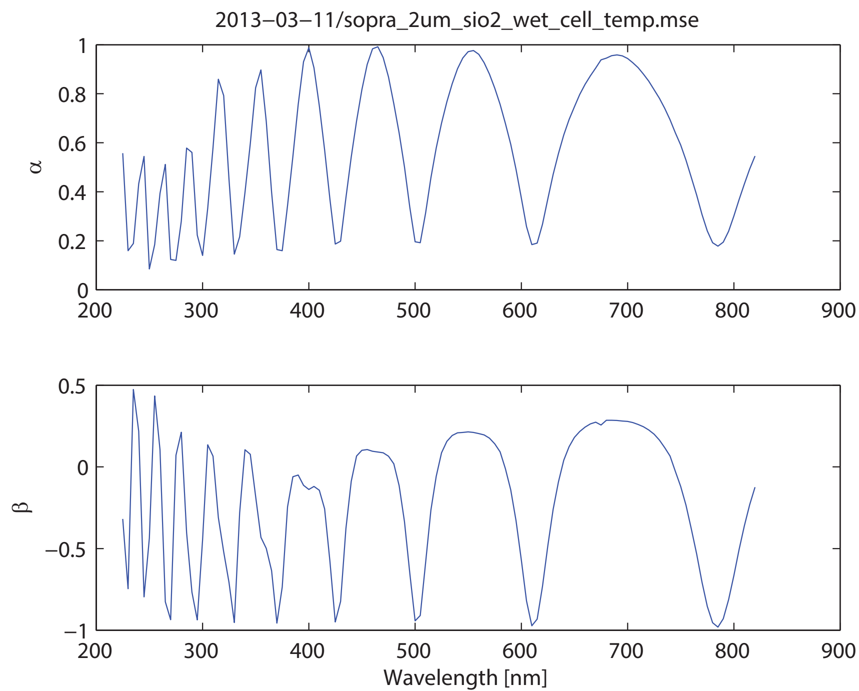

Figure 4.11 Representative ellipsometric spectrum for SOPRA reference wafer with 2.0037 µm SiO_2 on Si in deionized water.

Table 4.3 Estimated ambient temperature T for ellipsometric measurements of the 2.0037 µm SiO_2 SOPRA reference wafer in undegassed and degassed deionized water.

Condition	T (°C)	σ_T (°C)
Undegassed	38.490 908 70	1.068 799 07
	37.918 067 39	1.002 989 93
Degassed	41.581 244 47	0.974 085 59
	42.250 935 75	1.134 420 33
	40.726 434 19	2.806 585 26

4.3 Errors due to stress-induced window birefringence

The inspiration to investigate stress-induced window birefringence was pure serendipity. We noticed that when we seeded a geometric regression on immersion data for the 700 nm Sony photoresist grating with the best-fit 8-trapezoid geometry from the atmospheric case, the simulated α spectrum fit the experimental spectrum quite well, but the simulated β spectrum appeared offset from the experimental spectrum, as illustrated in Figure 4.12. Since

$$\alpha = -\cos(2\Psi) \qquad \beta = \sin(2\Psi)\cos\Delta,$$

systematic errors in β and not α imply errors in the phase Δ and not in the amplitude Ψ. Since the systematic error is only present in the immersion case and not in the atmospheric case, the leading candidate for causing this error is stress-induced window birefringence due to the hydrostatic pressure of the immersion fluid.

There is considerable work on modeling, measuring, and compensating for intrinsic or stress-induced birefringence in ellipsometry cell windows, especially for measuring samples in evacuated or pressurized environments. The usual model for the window birefringence is the small-retardance waveplate (SRWP) [48, 49, 50, 51, 52]. Johs and co-workers [53] decompose the retardance of the windows into an *in-plane* component

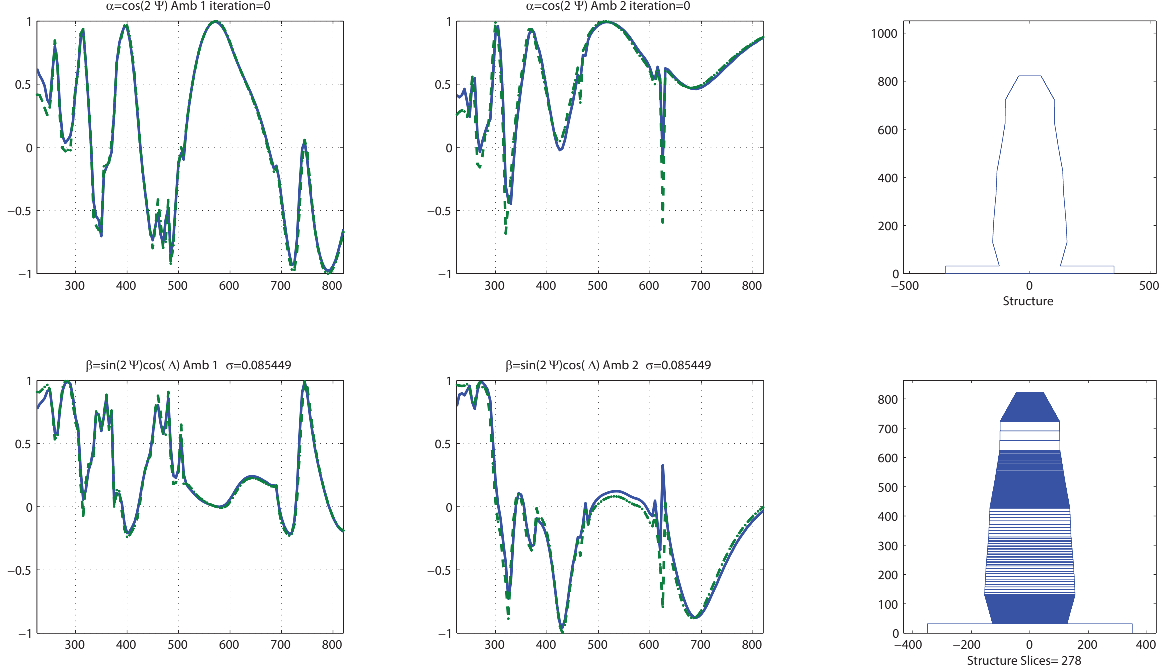

Figure 4.12 Comparison of the dry and wet simulated ellipsometric spectra for the dry best-fit profile for the 700 nm Sony photoresist grating. The wet β spectrum (bottom center) shows an offset between the experimental data (solid blue) and the simulated spectrum (green dashed) for the dry best-fit profile in the immersion case.

(which is a waveplate with the fast axis aligned in the plane of incidence) and an *out-of-plane* component (which is a waveplate with fast axis at 45° relative to the plane of incidence). The out-of-plane component can be determined by regression calibration of the ellipsometer [54], leaving just the in-plane component to be determined by regression analysis on a known reference sample. To first order, the dispersion formula for the in-plane retardance is

$$\Delta_w = \frac{p}{\lambda}$$

for some constant p [55].

4.3.1 Simulation

As in the case of angle of incidence and ambient refractive index, we motivate our experimental work by simulating the change in the ellipsometric spectrum for the

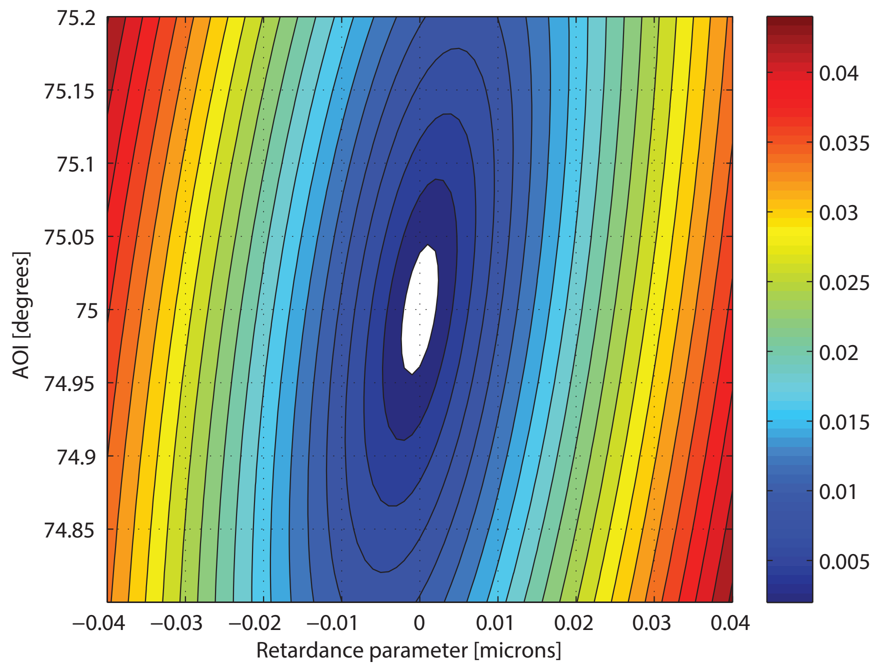

Figure 4.13 Error surface for immersion ellipsometry of a nominally bare silicon wafer (2 nm SiO_2 on Si) in deionized water for errors in the angle of incidence and first-order in-plane retardance parameter.

immersion measurements of a variety of unpatterned thin-film samples when different pairs of measurement parameters (e.g. angle of incidence, ambient refractive index parameters, etc.) are varied. The error surface for immersion ellipsometry of a nominally bare silicon wafer (2 nm SiO_2 on Si) in deionized water for errors in the angle of incidence and different values for the first-order in-plane retardance parameter is shown in figure 4.13. For comparison, the error surface for immersion ellipsometry of a thick (2 µm) SiO_2 film on Si in deionized water for errors in the angle of incidence and different values of the first-order in-plane retardance parameter is shown in figure 4.14.

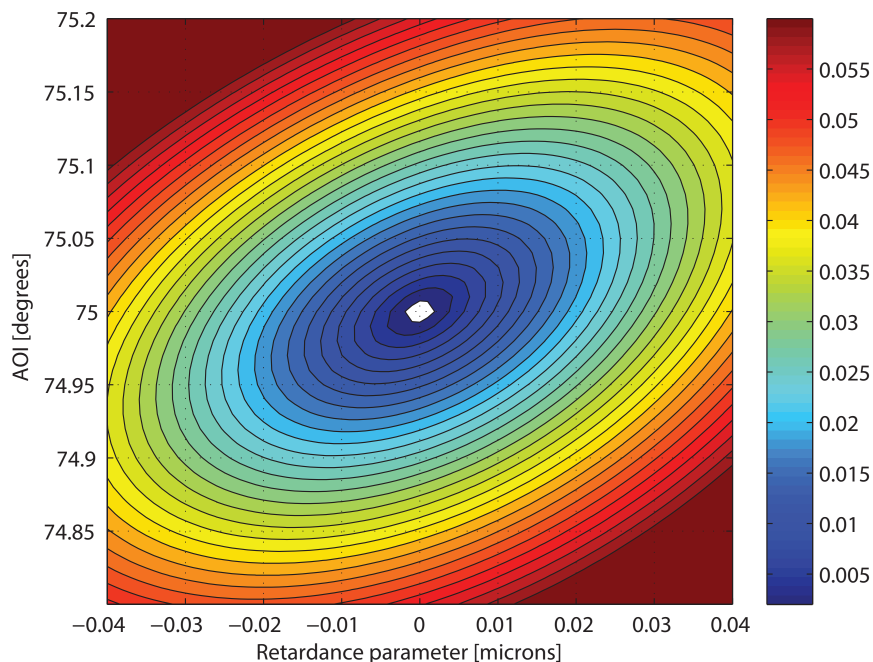

Figure 4.14 Error surface for immersion ellipsometry of a a thick (2 µm) SiO_2 film on Si in deionized water for errors in the angle of incidence and first-order in-plane retardance parameter.

4.3.2 Materials and methods

Samples

To estimate the in-plane retardance parameter p, we performed liquid immersion measurements on a SOPRA reference wafer with a nominal SiO_2 film thickness of 2.0037 µm.

Data analysis

Ellipsometric data were collected from 225 nm to 800 nm at 5 nm intervals. We adapted the MATLAB RCWA code to perform Levenberg-Marquardt regression for the oxide thickness t and the first-order in-plane plane retardance parameter p. This analysis was performed for the following structural model:

- An ambient medium of Tilton-Taylor water at 23 °C.

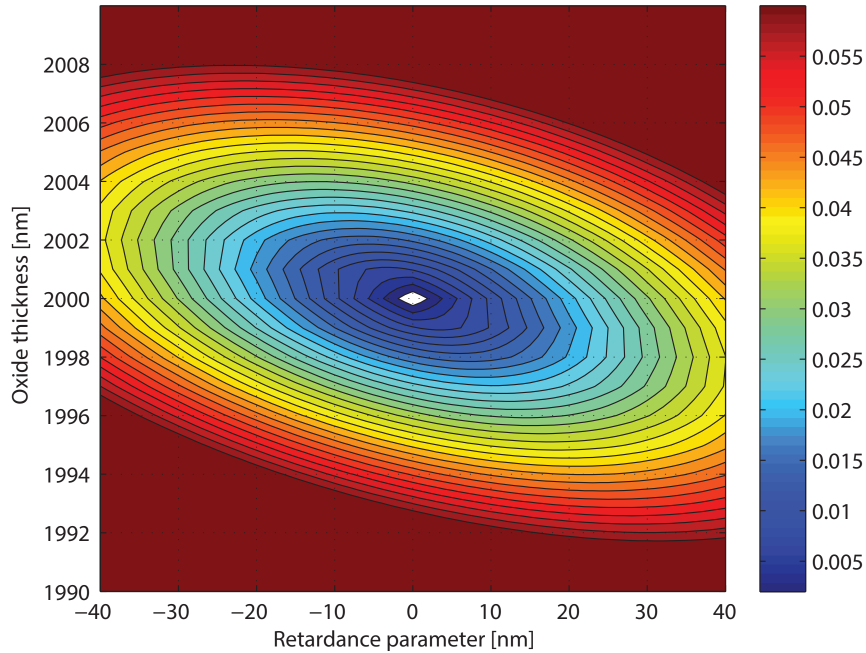

Figure 4.15 Error surface for immersion ellipsometry of a a thick (2 µm) SiO_2 film on Si in deionized water for errors in the oxide thickness and first-order in-plane retardance parameter.

- An SiO_2 film of 2.0025 µm nominal thickness (determined by ellipsometric measurements of the sample in air).
- A crystalline silicon substrate.

To verify that the thickness and estimated retardance parameter are not strongly cross-correlated, we ran thin-film simulations to determine the error surface for immersion ellipsometry of a thick (2 µm) SiO_2 film on Si in deionized water for errors in the oxide thickness and different values for the first-order in-plane retardance parameter, which is shown in figure 4.15.

4.3.3 Results and discussion

We took 5 measurements of the SOPRA reference wafer at a nominal angle of incidence $\theta = 74.85°$. The estimated parameters are tabulated in table 4.4. The estimated thickness of the oxide is 2012.42 ± 0.49nm and the estimated retardance parameter is

Table 4.4 Estimated oxide thickness t and in-plane retardance parameter p for ellipsometric measurements of the 2.0037 µm SiO_2 SOPRA reference wafer in deionized water.

SiO_2 thickness t [nm]	σ_t	Retardance parameter p [nm]	σ_p
2012.82	0.52	33.23	4.24
2012.39	0.48	32.55	3.95
2012.44	0.54	34.82	4.40
2012.50	0.50	35.00	4.10
2012.42	0.49	34.96	3.96

$$\bar{t}_{SiO_2} \pm \hat{\sigma}_t = 2012.42\,\text{nm} \pm 0.49\,\text{nm}$$
$$\bar{p} \pm \hat{\sigma_p} = 34.1\,\text{nm} \pm 0.5\,\text{nm}$$

34.1 nm ± 0.5 nm, and the cross-correlation between these two parameters is 0.617 38. The in-plane retardance spectrum corresponding to this estimate is plotted in figure 4.16. The in-plane retardance decays from approximately 9° at 225 nm wavelength to approximately 2° at 820 nm wavelength, which is of the same order as the retardance spectrum measured by Johs and co-workers for a standard 2-¾" conflat vacuum window [53].

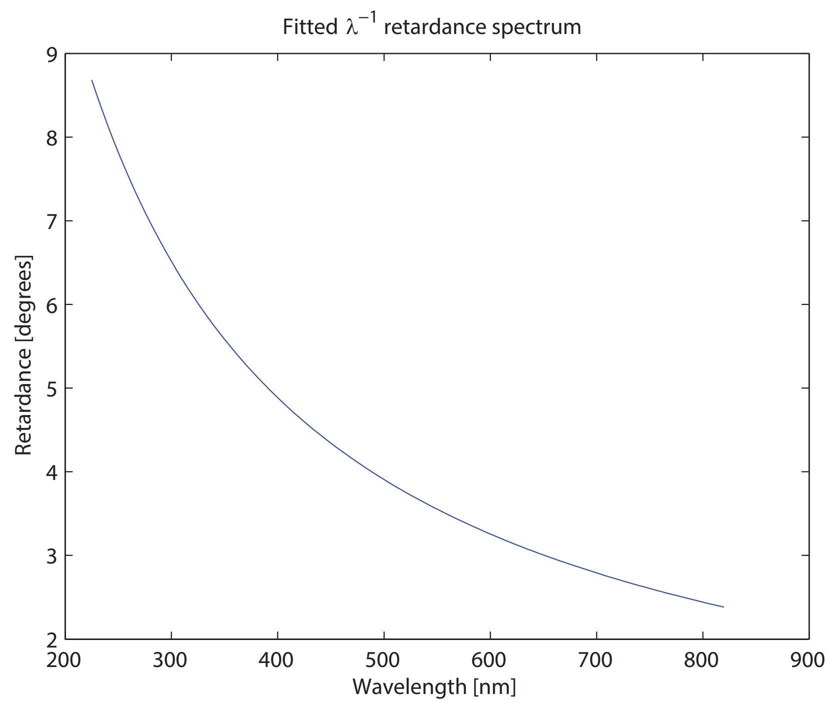

Figure 4.16 In-plane retardance spectrum estimated from ellipsometric measurements of the 2.0037 µm SiO_2 SOPRA reference wafer in deionized water.

Chapter 5

Improved procedure of grating topography extraction by immersion scatterometry

Having identified and characterized several relevant sources of systematic error in immersion ellipsometry, we are now in a position to improve the procedure for grating topography extraction by immersion scatterometry.

5.1 Materials and methods

We attempt to mitigate systematic error in immersion scatterometry due to errors in the immersion angle of incidence and stress-induced birefringence in the immersion cell windows by applying the following measurement procedure:

1. Measure a "bare" silicon wafer in air to characterize its structure (native oxide thickness).
2. Measure the "bare" silicon wafer in immersion to characterize the actual angle of incidence and adjust the nominal angle of incidence to match the estimated angle of incidence.
3. Measure a thick SiO_2 film in air to characterize its structure (oxide thickness).
4. Measure the thick SiO_2 film in immersion to characterize the stress-induced birefringence.
5. Measure a grating in air and produce a best-fit geometry for reference.
6. Measure the grating in immersion and determine the best-fit geometry with and without birefringence correction.

5.2 Results and discussion

5.2.1 Atmospheric measurements of bare silicon

We took 5 measurements of a bare silicon wafer in air at a nominal angle of incidence of 75° to estimate the native oxide thickness. The estimates of the angle of incidence θ and the native oxide thickness t are tabulated in table 5.1. After averaging the individual measurements and computing the standard error, the estimated angle of incidence is 75.0542° ± 0.0047° and the estimated native oxide thickness is 1.916 nm ± 0.036 nm.

Table 5.1 Atmospheric measurements of bare silicon used to estimate the native oxide thickness.

Angle θ	σ_θ	SiO_2 thickness t [nm]	σ_t
75.051 006	0.000 062	1.89	0.04
75.052 164	0.000 059	1.91	0.04
75.056 818	0.000 059	1.97	0.04
75.069 870	0.000 065	2.00	0.04
75.040 987	0.000 061	1.80	0.04

$$\bar{\theta} \pm \hat{\sigma}_\theta = 75.054\,169\,00° \pm 0.004\,697\,49°$$
$$\bar{t}_{SiO_2} \pm \hat{\sigma}_t = 1.915\,739\,800\,\text{nm} \pm 0.035\,543\,639\,\text{nm}$$

5.2.2 Immersion measurements of bare silicon

We took 9 measurements of the same bare silicon wafer in immersion at a nominal angle of incidence of 74.85° to establish the immersion angle of incidence. The estimates of the angle of incidence θ and the native oxide thickness t are tabulated in table 5.2. After averaging the individual measurements and computing the standard error, the estimated angle of incidence is 74.857° ± 0.008° and the estimated native oxide thickness is 2.379 nm ± 0.122 nm.

Table 5.2 Immersion measurements of bare silicon to estimate the immersion angle of incidence.

Angle θ	σ_θ	SiO_2 thickness t [nm]	σ_t
74.858 351	0.000 081	2.12	0.14
74.860 406	0.000 078	2.05	0.14
74.864 992	0.000 079	2.12	0.14
74.805 860	0.000 066	2.95	0.12
74.861 111	0.000 092	2.47	0.16
74.865 824	0.000 108	2.47	0.19
74.839 214	0.000 102	1.85	0.18
74.872 679	0.000 091	2.77	0.16
74.886 235	0.000 100	2.60	0.18

$$\bar{\theta} \pm \hat{\sigma}_\theta = 74.857 \pm 0.008°$$
$$\bar{t}_{SiO_2} \pm \hat{\sigma}_t = 2.38 \pm 0.12\text{nm}$$

5.2.3 Atmospheric measurements of thick SiO_2 film

We took 3 measurements of a SOPRA reference wafer (nominally 2.0037 µm SiO_2 on Si) in air at a nominal angle of incidence of 74.85° to estimate the oxide thickness. The estimates of the oxide thickness t are tabulated in table 5.3. After averaging the individual measurements and computing the standard error, the estimated thickness of the oxide is 2003.48 nm $\pm$ 0.07 nm.

Table 5.3 Atmospheric measurements of SOPRA 2.0037 µm SiO_2 reference wafer used to estimate the oxide thickness.

SiO_2 thickness t [nm]	σ_t
2003.53	0.32
2003.35	0.35
2003.57	0.34

$$\bar{t}_{SiO_2} \pm \hat{\sigma}_t = 2003.48\,\text{nm} \pm 0.07\,\text{nm}$$

5.2.4 Immersion measurements of thick SiO_2 film

We took 5 measurements of the SOPRA reference wafer (nominally 2.0037 µm SiO_2 on Si) in immersion at a nominal angle of incidence of 74.85° to estimate the first-order in-plane retardance parameter. The estimates of the angle of incidence θ and the native oxide thickness t are tabulated in table 5.4. After averaging the individual measurements and computing the standard error, the estimated thickness of the oxide is 2012.42 nm ± 0.49 nm and the estimated retardance parameter is 34.1 nm ± 0.5 nm.

Table 5.4 Immersion measurements of SOPRA 2.0037 µm SiO_2 reference wafer used to estimate the oxide thickness and the first-order in-plane retardance parameter.

SiO_2 thickness t [nm]	σ_t	Retardance parameter p [nm]	σ_p
2012.82	0.52	33.23	4.24
2012.39	0.48	32.55	3.95
2012.44	0.54	34.82	4.40
2012.50	0.50	35.00	4.10
2012.42	0.49	34.96	3.96

$$\bar{t}_{SiO_2} \pm \hat{\sigma}_t = 2012.42\,\text{nm} \pm 0.49\,\text{nm}$$
$$\bar{p} \pm \hat{\sigma_p} = 34.1\,\text{nm} \pm 0.5\,\text{nm}$$

5.2.5 Atmospheric measurements of 700-nm pitch Sony photoresist grating

We took several measurements of the 700-nm pitch Sony photoresist grating in air and used one to determine the 8-trapezoid best-fit geometry. Because we had issues with poor fit quality, we also took measurements of uniform thin films of the photoresist to measure their optical properties and correct for aging effects. A representative ellipsometric spectrum for a uniform film of the Sony photoresist is shown in figure 5.1. SOPRA WinElli was then used to simultaneously fit the film thickness and parameters for a mixed dispersion model consisting of two Lorentz oscillator terms and

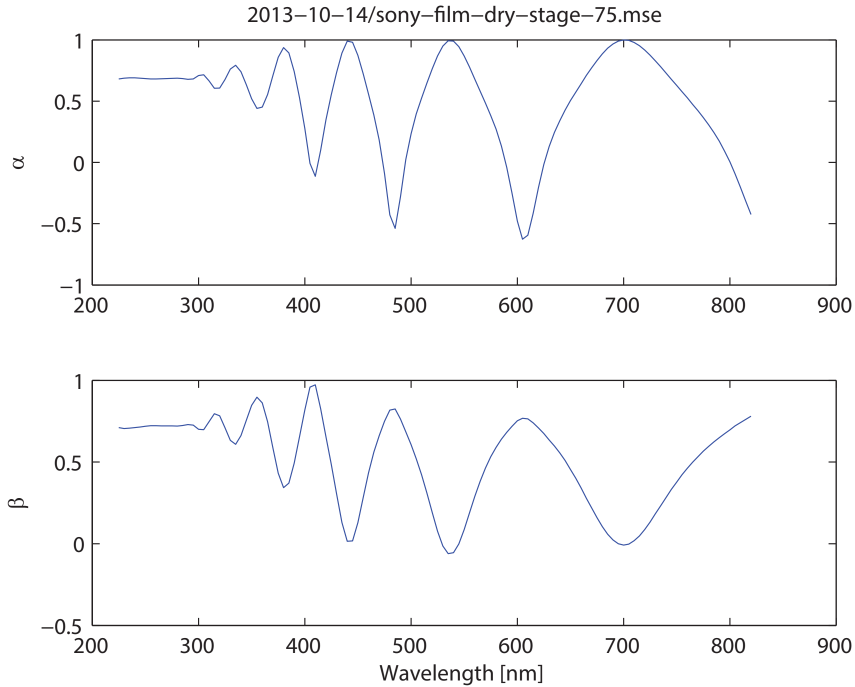

Figure 5.1 Measured SE data for a uniform film of Sony photoresist taken at $\theta = 75°$.

two Cauchy terms. The 8-trapezoid best-fit geometry using this dispersion model is shown in figure 5.2, and the parameter fits and 95.4% confidence limits are tabulated in table 5.5. The quality of fit is significantly improved relative to the published dry fit [5] ($\sigma \approx 0.036$ compared to $\sigma \approx 0.048$).

Table 5.5 Fit results and 95.4% confidence limits for an 8-trapezoid grating model to dry ellipsometric measurements of the 700-nm grating with new photoresist data.

Parameter	Fit (nm)	95.4% confidence
Height	789.92	2.33
Width 1 (top)	107.01	9.79
Width 2	206.44	11.76
Width 3	213.74	5.72
Width 4	240.80	5.99
Width 5	268.67	6.71
Width 6	284.71	8.68
Width 7	307.45	9.61
Width 8	316.79	8.82
Width 9	249.24	13.90

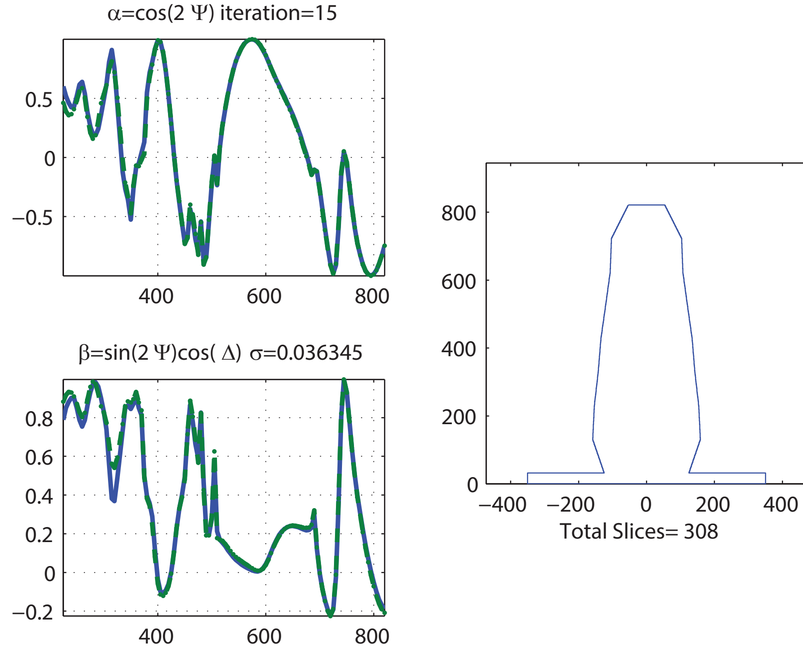

Figure 5.2 Measured and best-fit SE data for an 8-trapezoid model of the Sony 700-nm photoresist grating measured in air.

5.2.6 Immersion measurements of 700-nm pitch Sony photoresist grating

We took several measurements of the 700-nm pitch Sony photoresist grating in deionized water for two purposes:

1. To compare simulations of the dry best-fit geometry under immersion to experimental data.
2. To determine the 8-trapezoid best-fit geometry in the immersion with and without applying the birefringence correction determined using measurements on the SOPRA reference wafer.

The wet 8-trapezoid best-fit geometry determined without applying the birefringence correction is shown in figure 5.3, and the parameter fits and 95.4% confidence limits are tabulated in table 5.6. The wet 8-trapezoid best-fit geometry determined with first-order in-plane birefringence correction is shown in figure 5.4, and the parameter fits and 95.4% confidence limits are tabulated in table 5.7. The quality of fit improved

Table 5.6 Fit results and 95.4% confidence limits for an 8-trapezoid grating model to wet ellipsometric measurements of the 700-nm grating without birefringence correction.

Parameter	Fit (nm)	95.4% confidence
Height	810.91	2.31
Width 1 (top)	142.53	6.41
Width 2	141.85	8.09
Width 3	268.02	5.04
Width 4	162.07	7.09
Width 5	306.66	6.75
Width 6	243.57	7.74
Width 7	312.33	8.01
Width 8	284.27	8.32
Width 9	277.96	13.69

slightly with the birefringence correction from $\sigma \approx 0.051$ to $\sigma \approx 0.049$. The uncorrected wet fit exhibits several strong reentrant features which are less prominent in the corrected fit. RCWA forward simulation for this geometry in air deviates significantly with the atmospheric data (figure 5.5), suggesting that these features are artifacts, possibly due to overcorrecting the angle of incidence based on the results of the bare silicon measurement.

Reexamination of figure 4.13 suggests that it may be possible to extract both the angle of incidence and the first-order in-plane birefringence parameters from measurements of a thick SiO_2 film, which might also suppress these reentrant features. One possible measurement procedure is as follows:

1. Measure a thick SiO_2 film in air to characterize its structure (oxide thickness).
2. Measure the thick SiO_2 film in immersion.
    (a) Use the α (or Ψ) spectrum to determine the angle of incidence.
    (b) Use the β (or Δ) spectrum to characterize the stress-induced birefringence.
3. Adjust the nominal angle of incidence to match the estimated angle of incidence, and repeat the immersion measurement of the thick SiO_2 film until the estimates of the angle of incidence and stress-induced birefringence stabilize.

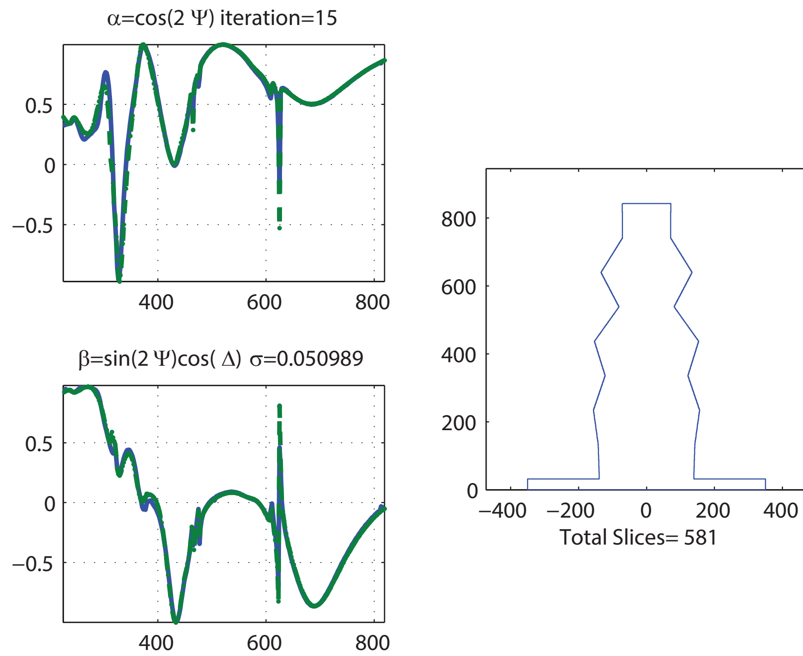

Figure 5.3 Measured and best-fit SE data for an 8-trapezoid model of the Sony 700-nm photoresist grating measured in deionized water with no birefringence correction.

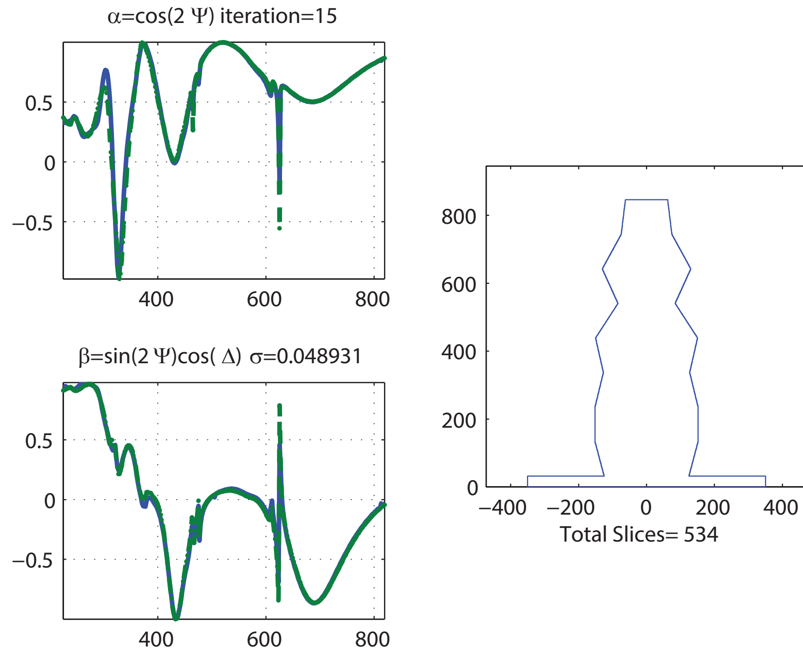

Figure 5.4 Measured and best-fit SE data for an 8-trapezoid model of the Sony 700-nm photoresist grating measured in deionized water with birefringence correction from thick SiO_2 data.

Table 5.7 Fit results and 95.4% confidence limits for an 8-trapezoid grating model to wet ellipsometric measurements of the 700-nm grating with birefringence correction.

Parameter	Fit (nm)	95.4% confidence
Height	814.07	2.33
Width 1 (top)	124.29	6.43
Width 2	149.13	7.82
Width 3	260.53	4.85
Width 4	168.29	6.86
Width 5	300.14	6.76
Width 6	254.04	7.77
Width 7	303.45	7.79
Width 8	303.39	7.92
Width 9	249.42	12.70

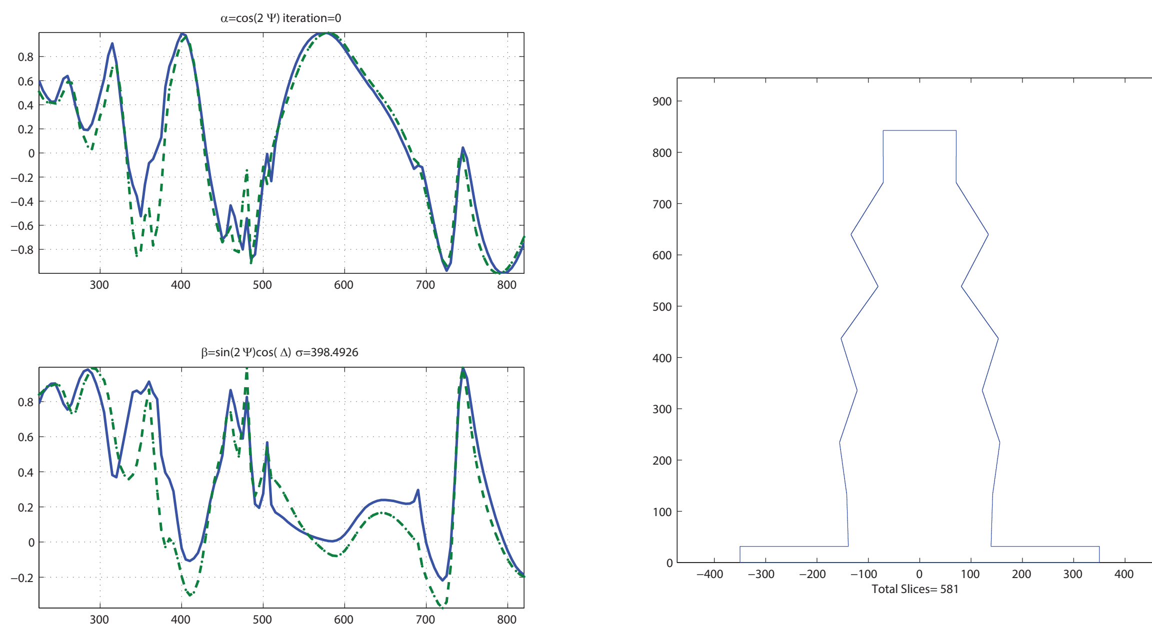

Figure 5.5 Comparison of the simulated dry ellipsometric spectra (green dashed) for the 8-trapezoid wet best-fit profile (without birefringence correction) for the 700 nm Sony photoresist grating with experimental data (solid blue).

Chapter 6
Conclusion and future work

6.1 Summary

In this thesis, we have presented the first experimental results for grating topography extraction by immersion scatterometry [5]. The resolution of those measurements was limited by systematic error of unknown origin, so we investigated several potential sources of error in immersion ellipsometry: error in the angle of incidence in the case of immersion, error in the refractive index of the immersion medium, and error introduced by stress-induced birefringence in the immersion cell windows. We motivated the selection of reference samples to characterize these sources of systematic error using computer simulations of thin-film optics, then performed the experiments. The results suggest that stress-induced birefringence in the immersion cell windows and error in the angle of incidence in the immersion case are the dominant sources of error. With this knowledge, we proposed a measurement procedure to correct for these systematic errors and report the results of applying this procedure. The new procedure did improve the quality of the regression fits and suggests that immersion scatterometry may still have the potential for improved resolution, but that potential has not yet been realized. However, the knowledge gained regarding the error sources that are present certainly puts us in a better position to attempt to realize that potential in the future.

6.2 Future work

The motivating question of this work remains unanswered: "Can the resolution of grating topography extraction by scatterometry be improved by immersion in a high-index medium?" The results reported in this thesis suggest that this goal may still be achievable if the sources of systematic error can be controlled. The dominant error source seems to be stress-induced birefringence in the immersion cell windows. The first avenue of future work is both to reduce this effect and to improve the method of correction. The magnitude of the effect can be reduced by using thicker windows or windows of different design, as was done by Studna and co-workers for vacuum applications of ellipsometry [56]. The method of correction can be improved by characterizing the out-of-plane retardance in addition to the in-plane retardance [55].

Another limitation seems to be the cross-correlation of difference sources of systematic error—a correlation that thus far cannot be broken with spectroscopic measurements of a single sample at a single angle of incidence. In the shorter term, there is additional work that can be done to explore, in simulation and in experiment, the pairwise interactions between various error sources in the immersion measurement for various choices of reference sample. In the longer term, it is worth investigating whether angle-resolved spectroscopic measurements at multiple angles of incidence can break this correlation and allow us to simultaneously fit to the geometry and the sources of systematic error. This is not possible with our current immersion cell design, but it may be possible with different cell designs, such as a the immersed light-guide design proposed by Benjamins and co-workers [57].

Bibliography

[1] B. D. Bunday and M. Bishop, "Benchmarking of advanced CD-SEMs at the 130-nm CMOS technology node," in *Metrology, Inspection, and Process Control for Microlithography XVI*, D. J. C. Herr, ed., *Proc. SPIE* **4689**, pp. 102–115, 2002.

[2] A. Habermas, D. Hong, M. F. Ross, and W. R. Livesay, "193-nm CD shrinkage under SEM: modeling the mechanism," in *Metrology, Inspection, and Process Control for Microlithography XVI*, D. J. C. Herr, ed., *Proc. SPIE* **4689**, pp. 92–101, 2002.

[3] C. Raymond, "Overview of scatterometry applications in high volume silicon manufacturing," in *Characterization and Metrology for ULSI Technology 2005.*, *AIP Conf. Proc.* **788**(1), pp. 394–402, 2005.

[4] H.-T. Huang and F. L. Terry, Jr., "Spectroscopic ellipsometry and reflectometry from gratings (scatterometry) for critical dimension measurement and in situ, real-time process monitoring," *Thin Solid Films* **455–456**, pp. 828–836, 2004.

[5] E. Liu and F. L. Terry, Jr., "Immersion scatterometry for improved nano-scale topography measurements," *physica status solidi (a)* **205**, pp. 784–788, Apr. 2008.

[6] H. P. Kleinknecht and H. Meier, "Linewidth measurement on IC masks and wafers by grating test patterns," *Appl. Opt.* **19**, pp. 525–533, Feb. 1980.

[7] J. R. McNeil, S. S. H. Naqvi, S. M. Gaspar, K. C. Hickman, K. P. Bishop, L. M. Milner, R. H. Krukar, and G. A. Petersen, "Scatterometry applied to microelectronics processing - part 1," *Solid State Technology* **36**, pp. 29–32, Mar. 1993.

[8] J. R. McNeil, S. S. H. Naqvi, S. M. Gaspar, K. C. Hickman, K. P. Bishop, L. M. Milner, R. H. Krukar, and G. A. Petersen, "Scatterometry applied to microelectronics processing - part 2," *Solid State Technology* **36**, pp. 53–56, Apr. 1993.

[9] M. E. Lee, C. Galarza, W. Kong, W. Sun, and F. L. Terry, Jr., "Analysis of reflectometry and ellipsometry data from patterned structures," in *International Conference on Characterization and Metrology for ULSI Technology*, D. G. Seiler,

A. C. Diebold, W. M. Bullis, T. J. Shaffner, R. McDonald, and E. J. Walters, eds., *AIP Conf. Proc.* **449**, pp. 331–335, 1998.

[10] X. Niu, N. H. Jakatdar, J. Bao, C. J. Spanos, and S. K. Yedur, "Specular spectroscopic scatterometry in DUV lithography," in *Metrology, Inspection, and Process Control for Microlithography XIII*, B. Singh, ed., *Proc. SPIE* **3677**, pp. 159–168, SPIE, Mar. 1999.

[11] X. Niu, N. Jakatdar, J. Bao, and C. Spanos, "Specular spectroscopic scatterometry," *IEEE Transactions on Semiconductor Manufacturing* **14**, pp. 97–111, May 2001.

[12] H. G. Tompkins and W. A. McGahan, *Spectroscopic Ellipsometry and Reflectometry: A User's Guide*, John Wiley & Sons, New York, NY, 1999.

[13] R. Petit, ed., *Electromagnetic Theory of Gratings*, Springer-Verlag Berlin Heidelberg, New York, NY, 1980.

[14] M. Neviere and E. K. Popov, "Electromagnetic theory of gratings: review and potential applications," in *Theory and Practice of Surface-Relief Diffraction Gratings: Synchrotron and Other Applications*, W. R. McKinney and C. A. Palmer, eds., *Proc. SPIE* **3450**, pp. 2–10, 1998.

[15] M. Nevière and E. Popov, *Light Propagation in Periodic Media: Differential Theory and Design*, Marcel Dekker, New York, NY, 2003.

[16] M. G. Moharam, E. B. Grann, D. A. Pommet, and T. K. Gaylord, "Formulation for stable and efficient implementation of the rigorous coupled-wave analysis of binary gratings," *J. Opt. Soc. Am. A* **12**, pp. 1068–1076, May 1995.

[17] M. G. Moharam, D. A. Pommet, E. B. Grann, and T. K. Gaylord, "Stable implementation of the rigorous coupled-wave analysis for surface-relief gratings: enhanced transmittance matrix approach," *J. Opt. Soc. Am. A* **12**, pp. 1077–1086, May 1995.

[18] H. Kogelnik, "Coupled wave theory for thick hologram gratings," *Bell System Technical Journal* **48**, pp. 2909–2947, Nov. 1969.

[19] P. Lalanne and G. M. Morris, "Highly improved convergence of the coupled-wave method for TM polarization," *J. Opt. Soc. Am. A* **13**, pp. 779–784, Apr. 1996.

[20] G. Granet and B. Guizal, "Efficient implementation of the coupled-wave method for metallic lamellar gratings in TM polarization," *J. Opt. Soc. Am. A* **13**, pp. 1019–1023, May 1996.

[21] L. Li, "Use of Fourier series in the analysis of discontinuous periodic structures," *J. Opt. Soc. Am. A* **13**, pp. 1870–1876, Sept. 1996.

[22] D. Y. K. Ko and J. R. Sambles, "Scattering matrix method for propagation of radiation in stratified media: attenuated total reflection studies of liquid crystals," *J. Opt. Soc. Am. A* **5**, pp. 1863–1866, Nov. 1988.

[23] C. Schwartz and L. F. DeSandre, "New calculational technique for multilayer stacks," *Appl. Opt.* **26**, pp. 3140–3144, Aug. 1987.

[24] P. Drude, "Bestimmung der optischen Constanten der Metalle," *Annalen der Physik* **275**(4), pp. 481–554, 1890.

[25] P. Drude, *The Theory of Optics*, Longmans, Green, and Co., New York, NY, 1901.

[26] A. Rothen, "The ellipsometer, an apparatus to measure thicknesses of thin surface films," *Review of Scientific Instruments* **16**(2), pp. 26–30, 1945.

[27] H. G. Tompkins, *A User's Guide to Ellipsometry*, Academic Press, San Diego, CA, 1993.

[28] R. W. Collins, I. An, and C. Chen, "Rotating polarizer and analyzer ellipsometry," in *Handbook of Ellipsometry*, H. G. Tompkins and E. A. Irene, eds., ch. 5, William Andrew, Norwich, NY, 2005.

[29] F. L. McCrackin, E. Passaglia, R. R. Stromberg, and H. L. Steinberg, "Measurement of the thickness and refractive index of very thin films and the optical properties of surfaces by ellipsometry," *J. Res. Natl. Bur. Stand. Sec. A* **67A**, p. 363, July 1963.

[30] J.-P. Moy, "Immersion ellipsometry," *Appl. Opt.* **20**, pp. 3821–3822, Nov. 1981.

[31] V. A. Yakovlev and E. A. Irene, "An interface enhanced spectroscopic ellipsometry technique: Application to Si-SiO_2," *Journal of The Electrochemical Society* **139**(5), pp. 1450–1455, 1992.

[32] V. A. Yakovlev, Q. Liu, and E. A. Irene, "Spectroscopic immersion ellipsometry study of the mechanism of Si/SiO_2 interface annealing," *Journal of Vacuum Science & Technology A: Vacuum, Surfaces, and Films* **10**(3), pp. 427–433, 1992.

[33] K. Levenberg, "A method for the solution of certain non-linear problems in least squares," *Quarterly of Applied Mathematics* **2**, pp. 164–168, 1944.

[34] D. Marquardt, "An algorithm for least-squares estimation of nonlinear parameters," *Journal of the Society for Industrial and Applied Mathematics* **11**(2), pp. 431–441, 1963.

[35] W. H. Press, S. A. Teukolsky, W. T. Vetterling, and B. P. Flannery, *Numerical Recipies: The Art of Scientific Computing*, Cambridge University Press, New York, NY, third ed., 2007.

[36] S.-H. Lu, L.-C. Tseng, C.-F. Kao, S.-P. Pan, and L.-C. Chang, "Immersion diffractometry for determining nanoscale grating pitch," *Optics Express* **14**, pp. 9564–9569, Oct. 2006.

[37] A. J. Den Boef, M. Dusa, A. G. M. Kiers, and M. Van Der Schaar, "Method and apparatus for angular-resolved spectroscopic lithography characterization." United States patent application 10/918,742, Aug. 2004.

[38] F. L. Terry, Jr. and J. J. Bendik, "Immersion scatterometry for improved feature resolution and high speed acquisition of resist profiles," in *Metrology, Inspection, and Process Control for Microlithography XIX*, R. M. Silver, ed., *Proc. SPIE* **5752**, pp. 237–247, 2005.

[39] M. Rothschild, T. M. Bloomstein, R. R. Kunz, V. Liberman, M. Switkes, S. T. Palmacci, J. H. C. Sedlacek, D. Hardy, and A. Grenville, "Liquid immersion lithography: Why, how, and when?," *J. Vac. Sci. Technol. B* **22**(6), pp. 2877–2881, 2004.

[40] L. W. Tilton and J. K. Taylor, "Refractive index and dispersion of distilled water for visible radiation, at temperatures 0 to 60°C," *J. Res. Natl. Bur. Stand.* **20**, pp. 419–477, Apr. 1938.

[41] D. A. G. Bruggeman, "Berechnung verschiedener physikalischer Konstanten von heterogenen Substanzen. I. Dielektrizitätskonstanten und Leitfähigkeiten der Mischkörper aus isotropen Substanzen," *Annalen der Physik* **416**(8), pp. 665–679, 1935.

[42] D. E. Aspnes, "Local-field effects and effective-medium theory: A microscopic perspective," *American Journal of Physics* **50**(8), pp. 704–709, 1982.

[43] C. J. J. Fox, "On the coefficients of absorption of nitrogen and oxygen in distilled water and sea-water, and of atmospheric carbonic acid in sea-water," *Trans. Faraday Soc.* **5**, pp. 68–86, 1909.

[44] T. Berlind, G. K. Pribil, D. Thompson, J. A. Woollam, and H. Arwin, "Effects of ion concentration on refractive indices of fluids measured by the minimum deviation technique," *physica status solidi (c)* **5**(5), pp. 1249–1252, 2008.

[45] X. Quan and E. S. Fry, "Empirical equation for the index of refraction of seawater," *Appl. Opt.* **34**, pp. 3477–3480, June 1995.

[46] H.-T. Huang, *High-accuracy, high-speed measurement of deep submicron and nano-structure gratings using specular reflected light techniques.* PhD thesis, University of Michigan, Ann Arbor, MI, 2002.

[47] A. Harvey, S. Kaplan, and J. Burnett, "Effect of dissolved air on the density and refractive index of water," *International Journal of Thermophysics* **26**, pp. 1495–1514, Sept. 2005.

[48] F. L. McCrackin, "Analyses and corrections of instrumental errors in ellipsometry," *J. Opt. Soc. Am.* **60**, pp. 57–63, Jan. 1970.

[49] A. Straaijer, L. Hanekamp, and G. Bootsma, "The influence of cell window imperfections on the calibration and measured data of two types of rotating-analyzer ellipsometers," *Surface Science* **96**(1–3), pp. 217–231, 1980.

[50] J. M. M. de Nijs and A. van Silfhout, "Systematic and random errors in rotating-analyzer ellipsometry," *J. Opt. Soc. Am. A* **5**, pp. 773–781, June 1988.

[51] R. Kleim, L. Kuntzler, and A. El Ghemmaz, "Systematic errors in rotating-compensator ellipsometry," *J. Opt. Soc. Am. A* **11**, pp. 2550–2559, Sept. 1994.

[52] G. E. Jellison, "Windows in ellipsometry measurements," *Appl. Opt.* **38**, pp. 4784–4789, Aug. 1999.

[53] B. D. Johs, J. Hale, N. J. Ianno, C. M. Herzinger, T. E. Tiwald, and J. A. Woollam, "Recent developments in spectroscopic ellipsometry for in-situ applications," in *Optical Metrology Roadmap for the Semiconductor, Optical, and Data Storage Industries II*, A. Duparre and B. Singh, eds., *Proc. SPIE* **4449**, pp. 41–57, 2001.

[54] B. Johs, "Regression calibration method for rotating element ellipsometers," *Thin Solid Films* **234**(1–2), pp. 395–398, 1993.

[55] B. Johs and C. Herzinger, "Methods for uncorrelated evaluation of parameters in parameterized mathematical model equations for window retardence, in ellipsometer and polarimeter systems." US Patent 6,034,777, Mar. 7, 2000.

[56] A. A. Studna, D. E. Aspnes, L. T. Florez, B. J. Wilkens, J. P. Harbison, and R. E. Ryan, "Low-retardance fused-quartz window for real-time optical applications in ultrahigh vacuum," *Journal of Vacuum Science & Technology A* **7**(6), pp. 3291–3294, 1989.

[57] J.-W. Benjamins, B. Jönsson, K. Thuresson, and T. Nylander, "New experimental setup to use ellipsometry to study liquid-liquid and liquid-solid interfaces," *Langmuir* **18**(16), pp. 6437–6444, 2002.